

2017-10

Crystallographic control and texture inheritance during mylonitization of coarse grained quartz veins

Ceccato, A

<http://hdl.handle.net/10026.1/10245>

10.1016/j.lithos.2017.08.005

Lithos

Elsevier

All content in PEARL is protected by copyright law. Author manuscripts are made available in accordance with publisher policies. Please cite only the published version using the details provided on the item record or document. In the absence of an open licence (e.g. Creative Commons), permissions for further reuse of content should be sought from the publisher or author.

1 **Crystallographic control and texture inheritance during mylonitization of coarse grained** 2 **quartz veins**

3 Alberto Ceccato^{1*}, Giorgio Pennacchioni¹, Luca Menegon², Michel Bestmann³

4 ¹ Department of Geosciences, University of Padova, Via Gradenigo 6, I-35131 Padova, Italy

5 ² School of Geography, Earth and Environmental Sciences, Plymouth University, United Kingdom

6 ³ GeoZentrum Nordbayern, Friedrich-Alexander-Universität Erlangen-Nürnberg (FAU), Germany

7 * Corresponding author.

8 Tel.: +39 0498279106; fax: +39 049 8279134

9 E-mail: alberto.ceccato.2@phd.unipd.it

10 **Abstract**

11 Quartz veins within Rieserferner pluton underwent deformation during post-magmatic cooling at
12 temperature close to 450 °C. Different crystallographic orientations of cm-sized quartz vein crystals
13 conditioned the evolution of microstructures and crystallographic preferred orientations (CPO)
14 during vein-parallel simple shear up to high shear strains ($\gamma \approx 10$). For $\gamma < 2$, crystals stretched to
15 ribbons of variable aspect ratios. The highest aspect ratios resulted from {m}<a> glide in ribbons
16 with c-axis sub-parallel to the shear zone vorticity Y-axis. Ribbons with c-axis orthogonal to Y (XZ-
17 type ribbons) were stronger and hardened more quickly: they show lower aspect ratios and fine
18 (grain size ~ 10 -20 μm) recrystallization along sets of microshear zones (μSZs) exploiting
19 crystallographic planes. Distortion of XZ-type ribbons and recrystallization exploit preferentially
20 those slip systems with misorientation axis close to Y. New grains of μSZs initiated by subgrain
21 rotation recrystallization (SGR) and thereupon achieved high angle misorientations by a concurrent
22 process of heterogeneous rigid grain rotation around Y associated with the confined shear within the
23 μSZ . Dauphiné twinning occurred pervasively, but did not played a dominant role on μSZ
24 nucleation. Ribbon recrystallization became widespread at $\gamma > 2$ and pervasive at $\gamma \approx 10$.
25 Ultramylonitic quartz veins are fine grained ($\sim 10 \mu\text{m}$, similar to new grains of μSZ) and show a

26 CPO banding resulting in a bulk c-axis CPO with a Y-maximum, as part of a single girdle about
27 orthogonal to the foliation, and orientations at the pole figure periphery at moderate to high angle to
28 the foliation. This bulk CPO derives from steady-state SGR associated with preferential activity, in
29 the different CPO bands, of slip systems generating subgrain boundaries with misorientation axes
30 close to Y. The CPO of individual recrystallized bands is largely inherited from original
31 crystallographic orientation of the ribbons (and therefore vein crystals) from which they derived.
32 High strain and pervasive recrystallization were not enough to reset the initial crystallographic
33 heterogeneity and this CPO memory is explained by a dominance of SGR. This contrast with
34 experimental observation of a rapid erasure of a pristine CPO by cannibalism from grains with the
35 most favourably oriented slip system under dominant grain boundary migration recrystallization.

36 **1. Introduction**

37 Quartz is one of the most representative minerals of continental crust rocks and has been commonly
38 assumed to control the first-order rheology of large portions of the ductile crust (e.g. Ranalli, 2000).
39 This explains the huge effort made in understanding quartz rheology during geological deformation.
40 Physical deformation experiments have determined constitutive flow laws for quartz under different
41 laboratory conditions (e.g., Luan and Paterson, 1992; Hirth and Tullis, 1992; Gleason and Tullis,
42 1995; Hirth et al., 2001). Application of these lab-determined flow laws to natural deformation
43 implies extrapolation to over several orders of magnitude in strain rate (from $< 10^{-5} \text{ s}^{-1}$ to values as
44 high as 10^{-12} - 10^{-16} s^{-1}) and the reliability of such extrapolation is legitimized by the similarity of
45 microstructures, crystallographic preferred orientations (CPO) and inferred recrystallization
46 mechanisms between the experimentally and naturally deformed quartz (e.g. Hirth et al., 2001;
47 Mancktelow and Pennacchioni, 2010). With this aim numerous experimental studies have
48 investigated the development and evolution of microstructures and CPO with strain (Tullis et al.,
49 1973; Tullis, 1977; Dell'Angelo and Tullis, 1989; Gleason et al., 1993; Heilbronner and Tullis,
50 2006; Muto et al., 2011). Due to limitations of experimental apparatus, deformation experiments on
51 quartz have been conducted on either single quartz crystals (Hobbs, 1968; Vernooij et al., 2006a, b;

52 Muto et al., 2011) or on relatively fine-grained natural and synthetic quartz aggregates (e.g.:
53 novaculite, Black Hill quartzite). The experiments on quartz single crystals are of particular
54 relevance for the interpretation of many natural mylonitic quartz where recrystallized aggregates
55 were derived from coarse original grains (several mm to tens of mm in grain size); either quartz
56 grains of granitoid rocks and metamorphic rocks (Kilian et al., 2011; Bestmann and Pennacchioni,
57 2015) or quartz crystals from veins (Stipp et al., 2002; Pennacchioni et al., 2010; Price et al., 2016).
58 The experiments of Muto et al. (2011) have evidenced a control of the initial quartz crystallographic
59 orientation with respect to the imposed stress field on the crystal strength, recrystallization rate and
60 developing CPO of recrystallized aggregates. However, Muto et al. (2011) observed that all crystals
61 developed, during dynamic recrystallization, distinct domains with a CPO consistent with the
62 favoured $\{m\}\langle a \rangle$ slip that rapidly cannibalized the aggregates with other unfavourable orientations
63 with increasing shear. The memory of the original crystallographic orientations was totally erased
64 after a relatively small amount of shear. This experimental result is not consistent with the observed
65 evolution of some mylonitic quartz veins that shows a more long-lasting heredity of the original
66 crystallographic orientations of parent grains in the CPO of recrystallized aggregates (Pennacchioni
67 et al., 2010).

68 We present here the analysis of the microstructural and CPO evolution at increasing strain of quartz
69 veins from a simple geological setting of a cooling pluton, similar to the context described in
70 Pennacchioni et al. (2010). This analysis reveals a complex evolution over large strain determined
71 by the initially different orientations of the vein crystals. This initial heterogeneity in crystal
72 orientations is not dismantled by mylonitization up to stages of complete dynamic recrystallization.

73 **2. Geological background and field description**

74 The 32 Ma old Rieserferner pluton (Eastern Alps) (Romer and Siegesmund, 2003) belongs to a
75 series of intrusions emplaced along the Periadriatic Lineament in the Eocene-Oligocene (referred to
76 as Periadriatic magmatism: Rosenberg, 2004). This pluton, emplaced at a depth of 12-15 km (0.25-
77 0.35 GPa: Cesare, 1994) into the Austroalpine tectonic unit, consists of 3 main granitoid intrusions

78 of coarse-grained garnet-bearing tonalites, granodiorites and fine-grained leucogranites (Bellieni,
79 1978; Steenken et al., 2000; Wagner et al., 2006). The estimated cooling time of the pluton to
80 equilibrate to the ambient temperature varies between 1.5 and 2 Ma, depending on the cooling
81 model and the reference host rock temperature (350 °C: Steenken et al., 2000; 425 °C: Wagner et
82 al., 2006). During post-magmatic cooling the intrusive rocks were deformed along ductile shear
83 zones and cataclastic faults that overprinted the variably developed sub-magmatic to solid-state
84 foliations associated with both the emplacement-related doming process (Wagner et al., 2006) and
85 the activity of the Deferegggen-Antholz-Vals tectonic line (Mancktelow et al., 2001). The ductile
86 shear zones, typically few centimetres in thickness, exploited precursor joints and joint-filling veins,
87 as it is commonly observed in other granitoid plutons (e.g. Adamello: Pennacchioni, 2005; Sierra
88 Nevada: Pennacchioni and Zucchi, 2013) and in meta-granitoid units (Mancktelow and
89 Pennacchioni, 2005; Pennacchioni and Mancktelow, 2007; Menegon and Pennacchioni, 2010).

90 Quartz veins of variable thickness (up to few decimetres thick) occurs along a shallowly ESE-
91 dipping joint set (mean dip-direction/dip: N115°/20°), that almost invariably localized top-to-E
92 normal ductile shearing at conditions close to 450°C and 0.3 GPa (results from thermodynamic
93 modelling not reported in this paper). Deformed veins, ranging from protomylonites to
94 ultramylonites, have been sampled for the study presented here (Figs. 1a-c). The protomylonites are
95 coarse grained (reflecting the multi-millimetric grain size of the pristine quartz vein crystals) and
96 show an oblique rough foliation forming an angle in the range between 20° and 30° to the vein
97 boundary (Fig. 1a). The ultramylonites are fine grained, with a macroscopic flinty aspect, and show
98 a pervasive foliation oriented at a very low angle to the vein boundary (Fig. 1c).

99 **3. Microstructure of deformed quartz veins**

100 In the kinematic reference system adopted here for the shear zones, the X axis is parallel to the
101 stretching direction, the XY plane is parallel to the vein boundary, and the Z direction is orthogonal
102 to the vein boundary. Thin sections were cut parallel to the XZ plane. The microstructure and the
103 CPO of quartz in deformed quartz veins were analysed by: polarized light microscopy, computer

integrated polarization microscopy (CIP) and electron backscattered diffraction (EBSD). CIP allowed the expeditious microstructure-linked analysis of the c-axis orientations of the coarse grained protomylonites over large thin section areas (mm² to cm²). The details of the CIP and EBSD methods are given in the Appendix. Assuming simple shear within the tabular-shaped quartz veins, the shear strain γ localized into the vein was estimated from the angle θ between the internal oblique foliation and vein boundary according to the equation (Ramsay, 1980):

$$\tan 2\theta = -2/\gamma$$

3.1 Protomylonitic quartz veins

3.1.1. Ribbon grains

Weakly deformed quartz veins (Figs. 1a, 2a and, in supplementary online material, SOM1a) are characterized by largely predominant monocrystalline quartz ribbons, with different crystallographic orientation, which define a foliation inclined 20-30° to the vein boundary. Shear strains γ of 1.3 and 2.1 were estimated for the 2 analysed protomylonite samples.

The cumulative results of the microstructural analysis of 2 thin sections are shown in Fig. 2 (thin sections shown in Figs. 2a and SOM1a). In Figs. 2b and SOM1b, the different quartz ribbons are colour-coded, based on the CIP analysis, as a function of their dominant c-axis orientation according to the look-up-table of Figs. 2c and SOM1d. The cumulative c-axis CPO of the ribbons from the 2 thin sections shows a clustering (i) along a girdle approximately orthogonal to the ribbon elongation, and (ii) along the pole figure periphery, with a main clustering of the c-axes at a high angle to the ribbon elongation (Figs. 2c and SOM1d). We observe a difference in the ribbon microstructure depending on the c-axis orientation allowing the distinction of 3 end-member types: (1) Y-type ribbons, with c-axis close to Y (Fig. 3a); (2) Z-type ribbons, with c-axis close to Z (Fig. 3b); (3) XZ-type ribbons, with c-axis plotting along the pole figure periphery in intermediate position between X and Z. The XZ-type ribbons can be further distinguished in XZa- and XZb-types with the c-axis almost orthogonal and parallel to the ribbon elongation, respectively (Figs. 3c-

129 f).

130 The aspect ratio of ribbons is shown, for the different ribbon c-axis orientations, in the pole figure
131 of Fig. 2d. The measured aspect ratios are minimum values, given that most of the ribbons exceed
132 in length the thin section width, but there is a clear relationship between the measured aspect ratios
133 and the c-axis orientations (Fig. 2d): (i) the lowest aspect ratios (as low as about 2) belong to XZ-
134 type ribbons, and especially to XZa-types; and (ii) most of the high aspect ratios (as high as 17.5)
135 belong to Y-type ribbons.

136 **3.1.2. Recrystallization of ribbons**

137 The quartz ribbons of protomylonites show incipient recrystallization to fine-grained aggregates
138 that are distinguished with a black colour in the microstructural sketches of Figs. 2b and SOM1b.
139 On average over the whole thin section, the recrystallized aggregates form about 10% of the area.
140 The new grains have an average grain size, determined from EBSD data (see Appendix for the
141 methods), between 10 and 20 μm . Figure 2e shows the area fraction of recrystallized aggregates for
142 to the different c-axis orientations of the host ribbons and indicates that recrystallization is larger (as
143 much as 23% of ribbon area) in Z- and XZ-type ribbons. In Y-type ribbons, the recrystallization is
144 very limited or absent. The different crystallographic orientations of the ribbons also translate into a
145 difference of the internal deformation microstructures and of the geometry of the recrystallized
146 aggregates:

147 1) Y-type ribbons show subgrains elongated parallel to the ribbon elongation, sweeping undulose
148 extinction and limited recrystallization preferentially located at the ribbon boundaries (Fig. 3a).

149 2) Z-type ribbons show weak undulose extinction, a single set of deformation lamellae (fine
150 extinction bands, FEB: Derez et al., 2015) and recrystallized aggregates scattered across the ribbon
151 or arranged along sharp discontinuities aligned sub-parallel to the ribbon elongation (Fig. 3b). In the
152 most deformed ribbons (or portions of ribbons), recrystallized aggregates are clustered into
153 elongated domains, inclined at variable angle with respect to the ribbon elongation, locally forming

154 intersecting sets (lower ribbon portion in Fig. 3b). Coarse (100's of μm in size) polygonization and
155 recrystallization resemble the blocky localized extinction bands described in Derez et al. (2015)
156 (Fig. 3b).

157 3) XZ-type ribbons typically show bands of recrystallization arranged in two intersecting sets (Figs.
158 3c-f). These bands of recrystallization commonly correspond to micro-shear zones (μSZs) as
159 inferred from the displacement of the orthogonal set of μSZs . The dominant set of μSZs is
160 commonly oriented sub-parallel to the vein boundary. The other set is oriented at a high angle to the
161 vein boundary, sub-parallel to Z or slightly rotated consistently with the shear sense (i.e. clockwise
162 in all the images presented here showing dextral sense of shear: Figs. 4 and SOM1c). The direction
163 of the μSZs are slightly different in different ribbons (Figs. 4 and SOM1c). The μSZs of each set
164 have roughly a regular spacing (in the range between 10's of μm to 300 μm) on a local (sub-
165 millimetric) scale, but the spacing and the spatial density are variable across the ribbon. On a local
166 scale, the μSZs of both sets show a comparable thickness. The thickness of the μSZs correlates with
167 the amount of accommodated slip (Fig. SOM2).

168 The XZa-type ribbons are almost free of an optically visible internal distortion (except for a weak
169 undulose extinction) in between incipient μSZs (Fig. 3c). The domains cut by the μSZs preserve a
170 roughly square-lozenge shape up to relatively high degree of ribbon recrystallization. The XZb-type
171 ribbons commonly show a strong internal distortion manifested by undulose extinction and wide
172 extinction bands (WEBs of Derez et al., 2015; e.g. outlined by white arrows in Fig. 3f) (Fig. 3d).
173 The recrystallization aggregates of both XZa- and XZb-type have a strong CPO (evaluated with the
174 gypsum plate) different from that of the host ribbon (e.g. Fig. 3c). In XZa-type ribbons, the position
175 of c-axis of the recrystallized aggregates in pole plots is orthogonal to the boundary of the μSZs
176 (Figs. 3c-e; “c-normal” shear bands of van Daalen et al., 1999). In XZb-type ribbons, the position of
177 c-axis of the aggregates is almost parallel in pole plots, or slightly rotated with the sense of shear,
178 to the boundary of the μSZs (Figs. 3d-3f; “c-parallel” shear bands of van Daalen et al., 1999). The
179 CPO within the μSZs has been investigated in more detail by EBSD (see below).

180 **3.1.3 Distribution of fluid inclusions**

181 In protomylonites, fluid inclusions are mainly present within recrystallized aggregates, along the
182 μ SZ selvages and associated with polygonized domains of ribbons. In the latter case, subgrains are
183 locally outlined by fluid inclusions. In secondary electrons SEM images on broken surfaces (Figs.
184 SOM3a-b), the grain boundaries of recrystallized grains commonly show regularly arranged pores
185 with crystallographically-controlled etch-pit type shapes (Mancktelow and Pennacchioni, 2004).
186 Within relatively undeformed portions of XZ- and Z-type ribbons, local fluid inclusions are
187 scattered and not arranged in trails. Y-type ribbons are mainly free of fluid inclusions.
188 Recrystallized aggregates next to the μ SZs, commonly decorated with fluid inclusions, contain
189 locally small mica flakes that are aligned to define an internal foliation (Figs. SOM 3c-d).

190 **3.2. Mylonitic quartz veins**

191 Mylonitic quartz veins show a layered microstructure (Fig. 5a) determined by the alternation of: (i)
192 high aspect ratio (>7) monocrystalline ribbons; (ii) partially recrystallized ribbons; and (iii)
193 completely recrystallized layers. The amount of bulk recrystallization is close to 50% of the area.
194 The grain size of the recrystallized grains is comparable with the one along the μ SZ within the
195 ribbons of the protomylonites. Shear strains γ of 3.5 and 6.6 have been estimated for the mylonite
196 samples.

197 The monocrystalline ribbons are coarsely polygonized with prevalent subgrain boundaries
198 orthogonal to the ribbon elongation (Z-type ribbons). Ribbon recrystallization occurred at the
199 boundaries and along sharp bands trending parallel to the ribbon elongation (especially in Z-type
200 ribbons; e.g. Figs. 5a-b). The layers of partially recrystallized ribbons include lozenge-shaped to
201 elliptical quartz ribbon porphyroclasts (mainly XZa-type) embedded in the aggregate of
202 recrystallized grains (Fig. SOM3e). Completely recrystallized layers show an extinction banding
203 parallel to the foliation.

204 The cumulative CIP-determined c-axis pole figure of the monocrystalline ribbons resembles a type-

205 I girdle dominated by a concentration of c-axes in two small circles around the foliation pole (Fig.
206 5c). The bulk pole figure of the pervasively recrystallized domains consists of a short girdle (low
207 density of c-axis poles at the pole figure periphery) oriented at a high angle to the foliation (Fig.
208 5d).

209 **3.3 Ultramylonitic quartz veins**

210 Ultramylonites consist of a dominant (> 90% area) matrix of fine-grained (10-15 μm determined by
211 EBSD; see below) recrystallized grains that includes isolated quartz porphyroclasts (ribbon
212 porphyroclasts) and high aspect ratio (> 50) monocrystalline ribbons (Fig. 5e). The extinction
213 banding of the mylonitic aggregate and the ribbon grains define a foliation oriented at a low ($\sim 5^\circ$)
214 angle to the vein boundary yielding a shear strain $\gamma > 10$. The recrystallized grains show a shape
215 preferred orientation defining a foliation oblique to the extinction banding and inclined consistently
216 with the shear sense (Figs. SOM3g-h).

217 The ribbon porphyroclasts range in shape from lozenge- to lenticular- and fish-shaped and have an
218 asymmetry with stair-stepping geometry climbing against the sense of shear (Figs. SOM3f-g-h). As
219 inferred from CIP and optical (gypsum-plate inserted: Fig. SOM3d) analysis, all the porphyroclasts
220 have a similar c-axis orientation, about orthogonal to the mylonitic foliation. The CIP-determined
221 bulk CPO of the ultramylonite shows a strong maximum close to Y, which is part of a single girdle
222 inclined with respect to Z consistently with the sense of shear (Fig. 5g). This bulk CPO, derived
223 from layers with different CPO, has been investigated in detail by EBSD (see below).

224

225

226 **5. EBSD analysis**

227 The EBSD analysis (Figs. 6-10) was performed on selected microstructures of protomylonite and
228 ultramylonite. Information of EBSD analytical conditions are reported in the Appendix A. In
229 protomylonites, Y- and XZ-type ribbons, and the associated recrystallization aggregates along μSZs ,

230 were investigated as microstructural end-members of the ribbon evolution. In ultramylonite, we
231 have investigated both the CPO banding of the pervasively recrystallized matrix and a ribbon
232 porphyroclast that survived such high strains.

233 **5.1 EBSD analysis of protomylonite**

234 **5.1.1. Y-type ribbon**

235 The analysed Y-type ribbon (Fig. 6a) shows a c-axis distribution in pole figure forming a short
236 girdle centred on the Y-axis and oriented orthogonal to the ribbon elongation (Fig. 6b). The subgrain
237 boundaries are mostly straight and sub-parallel to the ribbon elongation with a spatial density
238 increasing towards the zones of incipient recrystallization at the ribbon boundaries. The subgrains
239 of highly polygonized domains and the few new grains have a similar grain size of about 15-20 μm .
240 The misorientation angle distribution (MAD) (both correlated and uncorrelated) shows a strong
241 maximum at low angle misorientations ($< 20^\circ$) and, for correlated misorientations, at around 60°
242 (Fig. 9a). In crystal coordinates, the low angle misorientation ($< 15^\circ$) axes show higher density
243 towards the c-axis and weakly around $\{m\}$; for high angle misorientations (close to 60°) there is a
244 high density towards the c-axis (Fig. 6c). In sample coordinates, the low angle misorientation axes
245 show high density close to the Y-axis (Fig. 6c) and at the pole figure periphery coinciding with $\{m\}$
246 poles, and there is an overall distribution to define a girdle sub-parallel to the ribbon elongation.
247 The high angle misorientations axes (mainly related to misorientations with angle $\sim 60^\circ$: Fig. 10a)
248 show high density around Y (i.e., sub-parallel to the c-axis) (Fig. 6c).

249 **5.1.2. XZa- and XZb-type ribbons**

250 The EBSD analysis was conducted on both XZa- (Figs. 7 and SOM6) and XZb-type ribbons (Fig.
251 8) and on included μSZs with different degrees of evolution: incipient (one to few grains thick),
252 evolved (in the range between few grains and 100s μm thick), and mature (several 100s μm thick).
253 The μSZs of XZa- and XZb-type ribbons are similar in their microstructural evolution and are
254 described together.

255 5.1.2.1 Internal distortion of the host ribbons

256 Both XZa-type and XZb-type ribbons show a heterogeneous internal distortion (Figs. 7b and 8b)
257 consistent with rotation of crystallographic directions around an axis sub-parallel to Y. This results
258 in a dispersion along the periphery to over 45° of the c-axis orientations (Figs. 7b and 8b). In the
259 XZa-type ribbon, the low-angle low misorientation boundaries are heterogeneously distributed,
260 wavy and poorly interconnected. In the XZb-type ribbon, low angle boundaries are straight with
261 sets sub-parallel to the trace of rhombohedral planes (low angle boundaries of areas (1) and (2) of
262 Fig. 8a). The MAD (Figs. 10b-c) for both types of ribbons show two maxima at low angle
263 misorientations ($< 15^\circ$) and at around 60° , similar to what observed for the Y-type ribbon. In crystal
264 coordinates, all the analysed portions of XZa- and XZb-type ribbons show, as a bulk, a widely
265 scattered distribution across the entire plot of low angle misorientation axes, but with increasing
266 density towards the positive and negative rhombs (see scheme of Fig. 6e for reference) and
267 especially towards the c-axis. It is of note that the distribution maxima are weak in all cases. This
268 bulk distribution probably masks a rather more heterogeneous distribution of misorientation axes as
269 indicated by the plots for the areas 1 and 2 in Fig. 8f showing more distinct clustering towards the c-
270 axis (area 1) and along a girdle between rhombohedral crystallographic planes {r} and {z} (area 2)
271 (see scheme of Fig. 6e for reference). The analysis of more strongly deformed portions of the XZ-b
272 type ribbon adjacent to the incipient μ SZs α and β also indicates distinct local patterns of low angle
273 misorientation axis in comparison to the rest of the host ribbon (Figs. SOM4a-b).

274 In sample coordinates, the misorientation axes of XZa-type ribbon are clustered at the periphery of
275 the pole figure close to the c-axis orientations of the host ribbon (Fig. 7e) for both low and high
276 angle misorientations. For XZb-type ribbons the bulk misorientation axes are: (i) strongly clustered
277 off-axis in the between Y and X in a region including the direction of {r} and the c-axis for low
278 angle misorientations; and (ii) sub-parallel to the host c-axis for high angle misorientation (basically
279 of 60°).

280 5.1.2.2 Incipient μ SZs

Incipient μ SZs are defined by discontinuous linear arrays of one-grain-thick recrystallization aggregates in alternation with, and flanked by, discontinuous subgrains rows (e.g. Fig. 8a). The new grains have the same size (about 10-20 μ m) as the surrounding subgrains (Figs. 7a-b and SOM5a). The contact area between the host and the incipient μ SZs is defined by one-subgrain-thick zone. The μ SZ traces are sub-parallel to the trace of rhombohedral crystallographic planes of the host ribbon (Figs. 8b-c). The c-axes of the new grains are distributed, in a rotational sense consistent with the μ SZ sense of shear (e.g., sinistral for the μ SZs α and β that are inclined more than 45° to the shear plane: Fig. 8), along the pole figure periphery. The spreading of these c-axis orientations ranges from orientations close to that of the host grain to almost orthogonal orientations (Fig. 8c). The axis distributions of new grains, together with the lattice distortion of the host grain, are consistent with rotations around Y (anticlockwise for the sinistral μ SZs α and β and clockwise for the dextral μ SZ ϕ , ϵ and δ). The host ribbon can be in direct contact with highly misoriented new grains even in one-grain-thick μ SZs.

The misorientation analysis of low angle boundaries (misorientations in the range of $2-15^\circ$) in the host grain adjacent to incipient μ SZs α and β (enclosed in the black polygons marked in Fig. 8a) shows misorientation axes clustering parallel to primary ($\langle r \rangle$ and $\langle z \rangle$) or secondary ($\langle \pi \rangle$ and $\langle \pi' \rangle$) rhombohedral directions (inverse pole figure of Fig. SOM4). In sample coordinates, these axes show a clustering that is close to the Y-axis (Fig. SOM4). The small number of new grains of incipient μ SZs (that show subgrain boundaries anyway) does not allow a statistically meaningful analysis of the misorientation axes.

5.1.2.3 Evolved μ SZs

Evolved μ SZs consist of recrystallized aggregates with a thickness of a few grains (μ SZs δ of Fig. 7a, and ϕ of Fig. 8a). A transition zone (< 100 μ m in thickness) between host crystal and the μ SZ aggregate is discontinuously present and includes a high spatial density of low- and high-angle boundaries, and relatively high lattice distortion gradients ($\sim 0.25-0.5$ $^\circ/\mu$ m, point-to-point smallest

306 misorientation angle). These transition zones alternate with domains where recrystallized grains are
 307 in sharp contact with a weakly distorted portion of host grain (Fig. 7a: $\mu\text{SZ } \delta$). High spatial density
 308 of subgrain boundaries is observed at intersections and stepover domains between μSZs . The
 309 subgrains next to μSZs and the new grains have comparable mean grain size of 10-20 μm (Figs.
 310 SOM5b and 7c). The 2 analysed μSZs are sub-parallel to the trace of either one of the positive $\{r\}$
 311 or negative $\{z\}$ rhombohedral crystallographic planes ($\mu\text{SZ } \delta$: Fig. 7b) and to the $\{m\}$
 312 crystallographic plane ($\mu\text{SZ } \phi$: Fig. 8b).

313 As for incipient μSZs , the c-axis of new grains of evolved μSZs within both XZa- and XZb-type
 314 ribbons are distributed in a rotational sense from the host orientation with rotation axis sub-parallel
 315 to Y (Figs. 7c and 8d). Recrystallized grains are polygonal to sub-rectangular in shape, which
 316 results in common triple and four-grain junctions, and show a strong shape preferred orientation
 317 inclined consistently with the shear sense of the μSZs . The grain size is homogeneous within a
 318 single μSZ , but can be slightly different (of few μm) in different μSZs (Figs. SOM5c). Pores are
 319 observed both at triple junctions and along the grain boundaries (Figs. SOM3a-b).

320 In relatively coarse (grain size $>15 \mu\text{m}$) and high aspect ratio (>3) new grains, the boundaries of
 321 local subgrains are mostly oriented orthogonal to grain elongation (e.g. Figs. 7a and 8a). However,
 322 recrystallized grains are dominantly strain-free (lattice distortion gradient $<0.2 \text{ }^\circ/\mu\text{m}$, point-to-point
 323 smallest misorientation angle). Though the number of data is very small, the misorientations axis
 324 related to these subgrain boundaries plot close to either rhombohedral ($\langle r \rangle$ and $\langle z \rangle$) or peripheral
 325 ($\langle m \rangle$ and $\langle a \rangle$) crystal axes when analysed individually. The MAD for the evolved μSZs is
 326 comparable to the MADs for the host ribbons, in the case of $\mu\text{SZ } \phi$ (Fig. 9g), but differs in $\mu\text{SZ } \delta$
 327 (Fig. 9e) for the presence of a wide range of misorientation angles also including intermediate
 328 values between 10° and 60° . In sample coordinates the misorientation axis distribution for both low
 329 and high angle ($15\text{--}45^\circ$) misorientations of both the evolved $\mu\text{SZ } \delta$ (Fig. 7f) and ϕ (Fig. 8g) shows a
 330 higher density spot eccentric to the Y-directions (in addition to the spot close to c-axis direction
 331 observed for high angle misorientations).

332 5.1.2.4 Mature μ SZs

333 The 2 analysed mature μ SZs belong to XZa-type ribbons (Figs. 7 and SOM6) and trend parallel to
334 the trace of one $\{r\}$ plane of the host ribbon (e.g., μ SZ ε in Figs. 7a-b). An irregular, discontinuous
335 contact zone ($< 200 \mu\text{m}$ thick) is locally present between the host ribbon and the recrystallized
336 aggregate of the μ SZs that involves a higher distortion and spatial density of subgrains of the ribbon
337 (Figs. 7a and SOM6a). The recrystallized aggregate of the μ SZs includes, close to its boundaries,
338 relatively coarse relics of the host ribbons that show a core-and-mantle transition to the
339 recrystallized grains in the interior of the μ SZs. The subgrains in the host transition zone and within
340 clasts inside the μ SZs have a comparable size ($10\text{-}20 \mu\text{m}$, e.g. Fig. SOM6d) as the new
341 recrystallized grains of the μ SZs.

342 Similar to incipient and evolved μ SZs, the mature μ SZs also show a CPO with crystallographic
343 axes dispersed (with rotation axis parallel to Y) from the orientations of the host grain (Figs. 7d and
344 SOM6e-g). In the thicker μ SZs of Fig. SOM6a, there is still a dispersion of crystallographic axes
345 around Y, but the c-axis maxima are also spread towards intermediate positions of the pole figure (3
346 columns on the left of Figs. SOM6e-g), that can be in part associated with the larger distortion (and
347 therefore crystallographic dispersion) of the host grain (Fig. SOM6b). The different domains
348 distinguished in the mature μ SZ of Fig. SOM6a, show distinct CPO, though still mainly referable to
349 different degrees of rotational spreading of crystallographic axes around Y from the host
350 orientation. These domains likely represent coherent portion of the host grain, dissected during the
351 incipient stage of the μ SZ evolution (as can be seen in the host grain of Fig. SOM6e), which
352 underwent rigid rotation before extensively recrystallized in the μ SZ.

353 The MADs of both the analysed mature μ SZs is comparable with those of the evolved μ SZ δ (Figs.
354 9f and 9h) .

355 In crystal coordinates, the low angle misorientation axis distributions have very low maxima for all
356 domains, with concentrations along girdles between $\{r\}$ and $\{z\}$ poles (e.g. domains ω and ψ) and

357 between $\{m\}$ and $\langle a \rangle$ directions (e.g. domains ξ and ψ) (Figs. 7g; Figs. SOM6e-g). In sample
358 coordinates there are stronger maxima of low angle misorientation axis towards the centre of the
359 pole figure (Y-axis) in all domains with a tendency to distribute along a girdle in domain ξ (Fig. 7g;
360 Figs. SOM6e-g).

361 **5.2 EBSD analysis of ultramylonite**

362 **5.2.1. Recrystallized matrix**

363 The EBSD map of the ultramylonite in Fig. 10a includes a large portion of recrystallized matrix
364 showing a CPO banding and a large ribbon porphyroclast.

365 The bulk c-axis pole figure (Fig. 10b) shows a girdle slightly inclined to the YZ plane, with the
366 sense of shear, and a peripheral concentration fading progressively towards the foliation plane and
367 therefore resembles the type of pole figure determined for the protomylonites and mylonites (Figs.
368 2c and 5c, respectively). This bulk pole figure results from the combination of distinct c-axis CPO
369 characteristic of the different layers composing the ultramylonite microstructure and referable to 3
370 main types (Figs. 10c-f): (1) layers with a c-axis short girdle, orthogonal to foliation, centred on the
371 Y-axis (Fig. 10e) and showing a dominant red colour in Fig. 10a (e.g. layer III); (2) layers with c-
372 axis maxima concentrated, along the bulk girdle, at intermediate positions between Y and the pole
373 figure periphery (referred to as “intermediate orientation”: Fig. 10f; layer IV) and showing violet
374 and purple colour in Fig. 11a; (3) layers with c-axis maxima towards the pole figure periphery
375 (referred to as “peripheral orientation”: Figs. 10c-d; layer I-II) and showing dominant blue and
376 green colours in Fig. 10a (e.g. domain I-II). The layers with the dominant peripheral c-axis direction
377 commonly contain grains with an intermediate orientation, but rarely grains with a Y-orientation.
378 These layers also commonly include quartz porphyroclasts.

379 The MAD indicates the presence of a strong maximum for correlated misorientations at low angle
380 misorientations ($< 15^\circ$) and a weak one for misorientations around 60° (Fig. 9i) for the bulk
381 microstructure and also for the individual layers with distinct CPO. The misorientation axis

distributions in crystal coordinates are very similar for all the different layers except for those containing the ribbon porphyroclasts, and show high density towards the c-axis orientation for both low and high ($\sim 60^\circ$) misorientations (2nd-3rd plots of Figs. 10b-f). For low angle misorientations the distribution of axes is broad with the maximum intensity increasing from the layers with peripheral directions (max = 1.6 multiple of uniform distribution, mud) to the intermediate directions (max = 2.29 mud) and to the Y-directions (max = 3.68 mud). For high angle misorientation the axes strongly concentrate around the c-axis orientation. In sample coordinates, the misorientation axes plots are also very similar for the different layers with misorientation axes clustered around Y, for low angle misorientations, and around the dominant c-axis orientation of the layer for high angle misorientations.

The mean (geometric) grain size of recrystallized grains in ultramylonites is $\sim 9 \mu\text{m}$ with negligible differences between the layers with different CPO (Fig. SOM8). The recrystallized aggregates show a strong oblique SPO. Grains belonging to layers with a Y- and intermediate c-axis orientations have a slightly larger aspect ratio (Y-orientation: R mean = 3.06; $\sigma = 1.26$; intermediate-orientation: R mean = 2.92; $\sigma = 1.29$) than those with peripheral maximum (R mean = 2.38; $\sigma = 1.05$).

5.2.2 Ribbon porphyroclasts

Asymmetric ribbon porphyroclasts are common within recrystallized layers with peripheral c-axis maxima. (Figs. 10a, 10g and 10i) As described above, the asymmetry of the ribbon porphyroclast is opposite to that commonly shown by mineral fishes in mylonite (e.g. Pennacchioni et al., 2001; ten Grotenhuis et al., 2002). This shape derives from dissection of ribbon grains along μSZs that are sub-parallel to a rhombohedral planes and suitably oriented for being activated as C' shear bands. The internal distortion of the porphyroclasts is manifested by undulose extinction and zones of high subgrain density especially close to the porphyroclast tips.

The c-axes of the ribbon porphyroclasts plot along the periphery of the pole figure dispersed over a range of $\sim 80^\circ$ from directions nearly orthogonal to the ultramylonitic foliation to directions at a low angle to foliation in the NW-SE pole figure quadrant for this “dextral” quartz mylonite (Fig. 10g).

408 The recrystallized aggregate surrounding the ribbon porphyroclasts show a c-axis preferred
409 orientation distributed along the pole figure periphery (Fig. 10h) with two c-axis maxima: (i) close
410 to the c-axis orientation of the ribbon porphyroclast; and (ii) close to the peripheral maxima at the
411 end of the CPO girdle visible in the bulk

412 The MAD for both the porphyroclast and the surrounding aggregate show a strong peaks at low
413 ($<15^\circ$) misorientations and a weaker one at about 60° (Figs. SOM7f-g). In crystal coordinates, the
414 misorientation axes distributions of both porphyroclast and recrystallized aggregate show (2nd-3rd
415 plots of Figs. 10g-h): (i) slightly higher density close to the periphery of the IPF along a {m} to $\langle a \rangle$
416 girdle and close to the c-axis for low angle misorientations; and (ii) high density around the c-axis
417 for misorientations around 60° . In sample coordinates, the low angle misorientation axes cluster
418 around Y, while the high angle misorientation axes overlap in orientation with the c-axis orientation
419 (4th-5th plots of Figs. 10g-h).

420 **6. CL imaging**

421 The CL in quartz is a powerful tool for investigating microstructural complexity and possible signs
422 of fluid-rock interaction (e.g. Bestmann and Pennacchioni, 2015). Two main observations come
423 from CL investigation: (i) recrystallization in and polygonalization around μ SZs are associated
424 with a lower (darker) CL-signal that overprint the heterogeneous CL signal of protomylonitic quartz
425 grains (Figs. SOM15a-f); (ii) ultramylonite textural domains are characterized by different CL
426 signatures (Figs. SOM15g-h). Detailed results of CL investigations on Rieserferner quartz veins are
427 reported in SOM.

428

429

430 **7. Discussion**

431

432

433

434

435 **From ribbons to dynamic recrystallization**

436 To a first approximation, the deformed quartz veins of Rieserferner show 2 main stages of evolution
437 with increasing strain: (i) formation of ribbon grains at low strain, with only subordinate
438 recrystallization; and (ii) ribbon dismantling by localized to pervasive dynamic recrystallization.
439 Ribbons dominate the microstructure at low bulk strain ($\gamma < 2$) and recrystallization became
440 widespread, for shear strain in a range between 3 and 6, to pervasive at $\gamma > 10$, when $> 90\%$ of the
441 vein volume was converted to an aggregate of small (10 μm mean grain size) dynamically
442 recrystallized grains. A similar evolution, from ribbon to fine-grained mylonites, was described for
443 deformed quartz veins within tonalites of Adamello pluton (Pennacchioni et al., 2010) that formed
444 and deformed in a similar context of pluton cooling as Rieserferner quartz veins. In Adamello,
445 Pennacchioni et al. (2010) determined that transition from non-recrystallized elongate-ribbon grains
446 to pervasively recrystallized veins occurred abruptly at $\gamma = 3$, a value roughly coinciding with the
447 threshold for widespread recrystallization estimated for Rieserferner veins. This γ value is also
448 remarkably similar to the effective shear strain recalculated in Heilbronner and Kilian (2017) for
449 pervasive recrystallization of Black Hill Quartzite during the general shear experiments described
450 by Heilbronner and Tullis (2006).

451 ***Non-recrystallized ribbon portions***

452 The pristine quartz veins were coarse grained and, in protomylonites, each ribbon represents a
453 stretched non-recrystallized crystal. Different initial crystallographic orientations of the vein
454 crystals caused different deformation behaviours during vein boundary-parallel simple shear (e.g
455 Bouchez, 1977; Mancktelow, 1981). Y-type ribbons behaved as the most plastically compliant
456 grains and stretched to high aspect ratios without significant recrystallization (Figs. 2d-e). This
457 implies that $\{m\} \langle a \rangle$ was the easy (most efficient in accommodating strain, and/or slip system with

low critical resolved shear stress) slip system at the conditions of deformation, as also supported by the low angle misorientation axis distribution showing a relatively strong maximum close to c-axis in crystal coordinates (Fig. 6c) and the resulting maximum parallel to the Y-direction in sample coordinates. Boundary trace analysis (Prior et al., 2002; Piazzolo et al., 2008) of subgrains with misorientation axes either around $[c]$ and $\langle m \rangle$ are consistent with the local occurrence of both $\{m\}\langle a \rangle$ and $(c)\langle a \rangle$ slip (Fig. SOM7). Misorientation around $\langle m \rangle$ (oriented NE-SW in the pole figure of Fig. 6b) could also explain the dispersion into a girdle (orthogonal to $\langle m \rangle$) of the c-axis by a distortional “tilting” or “flexural slip” along the basal plane with slip along the $\langle a \rangle$ nearly orthogonal to the misorientation axis (and roughly parallel to the shortening direction). This c-axis dispersion and the absence of a dispersion around the c-axis reflect the different efficiency of the 2 slip systems, with the favoured $\{m\}\langle a \rangle$ slip effectively accommodating crystal elongation and inducing negligible internal distortion of the ribbon.

The XZ- and Z-type ribbons derived from vein crystals with c-axis orthogonal to the Y-direction that should disadvantage the activity of $\{m\}\langle a \rangle$ slip. These ribbons were less strain-compliant than Y-types as indicated by their lower aspect ratio; the higher internal distortion resulted in faster hardening and in a higher degree of recrystallization at the same bulk strain. This is consistent with the experimental results of Muto et al. (2011) on synthetic single quartz crystals with different initial orientations chosen to activate the 3 main slip systems of quartz ($(c)\langle a \rangle$, $\{m\}\langle a \rangle$, and $\{m\}[c]$ under the same experimental conditions) even though there are remarkable differences in the microstructural and CPO evolution in the experiments compared with our natural samples as it will be discussed below.

XZ- and Z-type ribbons experienced lattice distortion, formation of subgrains, and incipient recrystallization, and show a widespread occurrence of Dauphiné twinning. In XZ-types ribbons the internal distortion is manifested by a dispersion of crystallographic axes around the Y-direction (similarly to the dispersion of c-axis observed for non recrystallized domains in Muto et al., 2011). Part of the internal distortion was accomplished through rotations around low angle misorientation

axes as indicated by the MAD (Figs. 9a-d). In all XZ-type ribbons, we infer that $\{m\}\langle a \rangle$ slip system still partially assisted intracrystalline deformation despite the unfavorable crystal orientation. This is suggested by the clustering of low angle misorientation axes towards the c-axis in crystal coordinates (Figs. 7e, 8e and SOM6c) and by trace analysis of a few subgrains (Fig. SOM10-12). As discussed for Y-type ribbons, the efficiency of $\{m\}\langle a \rangle$ slip resulted in a very minor lattice distortion associated with the misorientation around c-axis and this would explain the absence of any major dispersion of crystallographic axes around [c] in all pole figures of Figs. 7- SOM6. This interpretation is also supported by the fact that, in sub-plots of low angle misorientation axis distributions in crystal coordinates considering smaller ranges of misorientations (2-5°, 5-10° and 10-15°), the c-axis maxima are stronger at very low angle misorientations (Fig. SOM13-14).

In XZb-type ribbons, the distribution of low angle misorientation axis towards [c] in crystal coordinates is close to uniform (Fig. 8e). In sample coordinates, this distribution results in an eccentric maximum with respect to Y that does not coincide with the c-axis position in the pole figure. This maximum rather coincides with the position of $\{r-z\}$ suggesting that available slip systems (or combinations of slip systems) with misorientation axis close to the Y-direction were preferentially activated (e.g. Neumann, 2000; Lloyd et al., 2004; Morales et al., 2011). The heterogeneity in the deformation and activation of specific slip systems is illustrated by the analysis of the areas 1 and 2 of the same ribbon that show different types of distribution of low angle misorientation axes towards the c-axis and towards $\{r-z\}$. In the XZa-type ribbon of Fig. 7a the low angle misorientation axes distribution in sample coordinates shows a distribution along a girdle between the two peripheral c-axis directions suggesting the activation of slip systems with misorientation axis close to the Y-direction.

In general terms, this preferential activation of slip system with misorientation axis close to the kinematic vorticity axis may be aided also by the elastic and plastic anisotropic properties of quartz. The most compliant directions in quartz are close to $\langle m \rangle$ and $\langle r \rangle$, whereas the most stiff directions

510 are close to $\langle z \rangle$ (McSkimin et al., 1965; Menegon et al., 2011). This elastic anisotropy may be also
511 reflected in the differential activation of slip system (Menegon et al., 2011), activating preferentially
512 those slip system that exploit $\{m\}$ or $\{r\}$ planes.

513

514 ***Recrystallization within μ SZs of XZ-type ribbons***

515 In XZ-type ribbons, incipient recrystallization occurred along μ SZs. These recrystallization
516 microstructures have been already described for quartz and their origin has been interpreted in
517 different ways (e.g. van Daalen et al., 1999; Vernooij et al., 2005, 2006a, b; Trepmann et al., 2007,
518 2017; Stipp and Kunze, 2008; Menegon et al., 2008, 2011; Derez et al., 2015; Kjøl et al., 2015).
519 Similar μ SZs have also been described in feldspars (Stünitz et al., 2003; Menegon et al., 2013) and
520 in calcite (Bestmann and Prior, 2003; Rogowitz et al., 2016). The main characteristics of the μ SZs
521 in the quartz ribbons of the Rieserferner veins are summarized and discussed below.

- 522 a) The CPO of recrystallized aggregates of μ SZs show a dispersion of the crystallographic
523 axes, from the crystallographic orientations of the host grain, consistent with the sense of
524 shear of the μ SZs and with a rotational axis roughly coinciding with the vorticity axis of the
525 shear zone (Y-axis). The amount of dispersion does not scale with μ SZs thickness (and
526 accommodated slip). In fact, large rotations of crystallographic ($[c]$) axes ($\sim 90^\circ$) are also
527 observed for the new grains within incipient μ SZs. As discussed above, a smaller, but
528 similar dispersion of crystallographic axes is observed within the distorted host ribbon
529 grains.
- 530 b) The MAD for evolved and mature μ SZs include a wide range of misorientation angles
531 between 10° and 60° (except the evolved μ SZ ϕ : Fig. 9g). These MADs are significantly
532 different from those of both the host ribbons and ultramylonites that show clear and strong
533 peaks at low angle misorientations ($< 15^\circ$) and around 60° (Figs. 9b-d and 9i).
- 534 c) The misorientation axis distributions for low angle misorientations include high density
535 spots around different crystallographic orientations in the different μ SZs (e.g. $\{m\}$, $\{r-z\}$,

and $\langle a \rangle$ for $\mu\text{SZ } \epsilon$: Fig. 7g), but in sample coordinates higher density systematically occurs close, though slightly eccentric, to the Y-axis. Along with minor clustering towards the orientation of the c-axis they tend to form a girdle. ; showing also some correlation with misorientation axis distributions of the host ribbon. The eccentricity of the maximum is interpreted to reflect either the deviation of the local vorticity vector with respect to the bulk vorticity vector of the sample (i.e., the Y-axis), or the difficulty to precisely place the sample coordinate frame in a protomylonite and exactly cut the sample parallel to the principal kinematic sections (or both factors). High density of the low angle misorientation axes “close to Y” therefore implies a main rotation parallel to the vorticity axis with some preferential activation of well-oriented slip systems. This rotation of subgrains, controlled by the vorticity axis, is supported by the fact that also high angle misorientations (15-45°) between new grains within the μSZs show very similar maxima close to Y (Fig. SOM6). This suggests the occurrence of a purely kinematic “rigid body” rotation of the new grains around Y (e.g. Bestmann and Prior, 2003; Trepmann et al., 2007; Stipp and Kunze, 2008). A feature less easy to interpret is the dispersion of the misorientation axes to form a girdle in sample coordinates nearly orthogonal to grain SPO especially in mature μSZs (e.g. $\mu\text{SZs } \epsilon$, Fig. 7g, and ξ , Figs. SOM6e-h). In the $\mu\text{SZ } \epsilon$ (Fig. 7) the girdle is clearly subparallel to the trace of the subgrain and grain boundaries internal to the elongated grains .

d) Dauphiné twinning occurred pervasively within the host ribbons, but the orientation of μSZs is not systematically linked to Dauphiné twin boundaries in contrast to what was reported by Menegon et al. (2011).

e) There is crystallographic control on the orientation of the μSZs whose trend is subparallel to the trace of $\{r-z\}$, $\{m\}$ or (c), as reported in van Daalen et al. (1999), Vernooij et al. (2006a, b) and Kjøl et al. (2015). Negative rhombs $\langle z \rangle$ are the least compliant crystallographic directions in quartz (in terms of its anisotropic elastic properties, McSkimin et al., 1965; Menegon et al., 2011) and they may act as site of accumulation of dislocation and defects promoting recovery processes and/or micro-fracturing along them.

f) The grain size of the new grains is in the range between 10 and 20 μm for the differently

evolved μ SZs and is similar to the mean (geometric) grain size of the ultramylonitic recrystallized matrix (10 μ m). In the μ SZs the grain size of new grains is similar to the size of the subgrains locally developed at the boundary of the μ SZs (e.g. Bestmann and Prior, 2003; Trepmann et al., 2007). This supports the occurrence of a component of SGR recrystallization during incipient μ SZ nucleation or at the moving μ SZs boundary during progressive strain accumulation (e.g. Halfpenny et al., 2012). The size of the new recrystallized grains in the μ SZs was determined by the occurrence of recovery processes in the parent grains and cannot therefore be completely ascribed to a cataclastic process which has been inferred to occur during initial stages of μ SZ development by some authors (e.g. van Daalen et al., 1999; Vollbrecht et al., 1999; Kjøl et al., 2015)

g) The μ SZs were preferentially infiltrated by fluids and formed the backbones for fluid redistribution into the host ribbons as indicated by (i) the clustering of fluid inclusions along the μ SZs; and (ii) the pervasive resetting of the CL signature along and nearby μ SZs (e.g. Fig. SOM15e). The presence of mica, precipitated along incipient μ SZs and deformed within the aggregate of more evolved μ SZs (Figs. SOM3c-d), suggests that part of the fluid infiltration did not just post-date shearing. There are not evident fluid-inclusion trails within the host ribbon subparallel to the μ SZs that could support the hypothesis of an origin of the μ SZs from nucleation on precursor, healed microcracks.

Strain hardening of XZ-type ribbons resulted in development of crystallographically-controlled μ SZs. We infer that initial recrystallization along the μ SZs is associated with SGR as indicated by: (i) the discontinuous presence of a zone of subgrain polygonization in the host ribbon flanking the μ SZs (e.g. Bestmann and Prior, 2003); and (ii) by the similarity in size between the host ribbon subgrains and recrystallized new grains. The MADs of μ SZs show a wide range of high misorientation angles that indicate the occurrence of a concurrent deformation mechanism together with the incipient SGR. This concurrent mechanism must be at the base of the sudden change in orientation of new grains within μ SZs to the host and neighbour grains since the incipient stages of recrystallization and is indicated by a rotation of crystallographic axes preferentially around the

591 vorticity axis Y, but also around other directions (third column of Fig. SOM6). This mechanism
592 apparently became inactive in mylonites/ultramylonites despite the similarity in grain size of
593 recrystallized aggregates. We envisage that process of grains reorientation within the μ SZs as a
594 “rigid-body” rotation of grains, initiated as subgrains by SGR, related to the geometric roughness of
595 the μ SZs and to the confined slip along the μ SZs (similarly to the model presented by Trepmann et
596 al., 2017). This process is essentially an example of viscous grain boundary sliding which is in part
597 kinematically-controlled by the orientation of the local vorticity axis. The roughness results from
598 both the heterogeneous degree of subgrain/new grain evolution along the μ SZs that is renewed by
599 continuous formation of new subgrains at the μ SZs. Thickening of the μ SZs in fact occurred by
600 progressive incorporation of the host ribbon selvages and in mature shear zones the aggregate at the
601 core of the shear zone experienced higher degree of rotation, as shown by van Daalen et al. (1999)
602 in similar μ SZs in quartz (e.g. Fig. SOM6). Probably, thickening of the recrystallized aggregate
603 decreased the influence of the geometric roughness during confined shear and the efficiency of
604 “rigid body” rotation mechanisms, leaving the complete control on recrystallization process to
605 SGR recrystallization in mature μ SZs and in the following stages of mylonitization.

606 Our observation and interpretation are very similar to the results of Kjøl et al., (2015), who
607 describe the development of localized recrystallization along crystallographically-controlled
608 features similar to μ SZs in hardened quartz grains. Despite the similarities, we do not observe
609 striking evidence for cyclical embrittlement induced by fluid pressure oscillation or the evidence for
610 pressure-solution processes as suggested by Kjøl et al. Lack of (unexploited) fluid inclusion trails
611 point to a different origin for μ SZs. Initial brittle processes and micro-cataclasis locally induced by
612 anisotropic rheological properties of quartz may explain some of the above described characteristics
613 (e.g. high angle misorientation of new grains in incipient μ SZs) but we do not observe any other
614 evidence for it.

615 The observations from the Rieserferner deformed quartz veins are difficult to reconcile with many
616 experimental results of Muto et al. (2011). We observe, as in their experiments, that the initial

617 crystallographic orientation of the crystals resulted in a different strength of the grains that
618 promoted recrystallization of XZ-type ribbons badly oriented for easy glide. However, Muto et al.
619 (2011) observed the development of distinct domains of recrystallized grains with a Y-max CPO in
620 all crystals independently of the starting crystallographic orientation, which is not found in the
621 Rieserferner veins. In the experiments recrystallization within crystals with $\{m\}[c]$ and $(c)\langle a \rangle$
622 orientations was not spatially organized into μ SZs as in the Rieserferner XZ-type ribbons.

623 *Ultramylonitic quartz veins*

624 The quartz ultramylonites consist of a fine-grained aggregate of recrystallized grains. A typical
625 feature of mylonite and ultramylonite is the presence of CPO banding that is interpreted to be
626 inherited from the former vein quartz crystals and to derive from recrystallization of ribbons (and
627 therefore of vein crystals) with different original crystallographic orientations (e.g. Pauli et al.,
628 1996; Lloyd et al., 1992; Pennacchioni et al., 2010; Morales et al., 2011; Price et al., 2016)
629 persisting up to very high strains ($\gamma > 10$). The bulk c-axis CPO of the pervasively recrystallized
630 ultramylonites is comparable in type to the CPO of the ribbon protomylonites and shows a girdle at
631 a high angle to the mylonitic foliation (slightly inclined to the foliation normal according with sense
632 of shear) and a wide peripheral spreading becoming more rarefied close to the foliation. The mean
633 (geometric) grain size of recrystallized grains ($\sim 10 \mu\text{m}$), almost identical within the different layers
634 (at the contrary of Heilbronner and Tullis, 2006), is comparable (albeit slightly smaller and more
635 homogeneous) with the recrystallization grain size within the μ SZs of XZ-type ribbons. This
636 suggests that, throughout the whole deformation/recrystallization history and in all microstructures,
637 the recrystallized grain size was controlled by subgrain formation and recrystallization by SGR (as
638 also indicated by MAD; e.g. Halfpenny et al., 2012). Despite there was a clear difference in strength
639 between the differently oriented ribbons in the protomylonites, there is not a consequent variation in
640 subgrain and new grain sizes that should be expected according to grain size piezometry (Stipp and
641 Tullis, 2003). The individual misorientation axes distribution in crystal coordinates for the layers
642 with different CPO all show a more or less broad clustering towards the c-axis, that is however

643 weaker for the layers with a dominance of peripheral orientations (e.g. layers I and II of Fig. 10).
 644 The misorientation axis distributions in sample coordinates shows, for all layers, that the slip
 645 systems with misorientation axes well aligned with the Y-axis of the shear zones were preferentially
 646 activated and indicate a control of the bulk shear zone kinematic framework on recrystallization.

647 In Rieserferner ultramylonites, despite the evidence that the favoured slip system was $\{m\}\langle a \rangle$,
 648 there is no indication of any relevant strain partitioning between layers with different CPO in
 649 recrystallized aggregates and therefore of significant strength differences of recrystallized
 650 aggregates (as instead proposed by Heilbronner and Tullis, 2006; Toy et al., 2008; Muto et al.,
 651 2011). In Rieserferner ultramylonites there is no evidence of cannibalism of $\{m\}\langle a \rangle$ against the
 652 other slip systems, at least for the range of investigated strain and no significant reset of the CPO
 653 occurred. As recalled above, the microstructure appears homogeneous in terms of grain size and
 654 show only minor differences in the grain aspect ratios. These observations are not dissimilar from
 655 the conclusions of Pennacchioni et al. (2010), who also noted that (i) dynamic recrystallization,
 656 occurring rather abruptly in a range of γ between 2 and 3, did not significantly altered the CPO from
 657 weakly deformed ribbon mylonites to strongly deformed and pervasively recrystallized veins; and
 658 (ii) initial crystal orientations badly oriented for dominant $\{m\}\langle a \rangle$ persisted up to high strain.

659 In the experiments of Muto et al. (2011) on synthetic single crystals all the different starting
 660 orientations developed distinct domains of recrystallized grains with c-axis Y-maximum CPO and
 661 the area of these domains increased with increasing bulk shear strain and extent of dynamic
 662 recrystallization. They noted that there was a reset from the initial $\{m\}[c]$ and $(c)\langle a \rangle$ orientations
 663 that was basically complete for 100% recrystallization and $\gamma < 3$. In practice, these experiments
 664 imply that a quartz vein with initial random orientation of crystals would end up at relatively low
 665 strain in a homogeneous quartz ultramylonite with strong Y-max CPO without any inheritance from
 666 the original microstructure. This is in stark contrast with the evolution derived for the Rieserferner
 667 sheared quartz veins and other natural examples (e.g. Pennacchioni et al., 2010; Rahl and Skemer,
 668 2016). A main reason for such contrast could be the difference in recrystallization mechanism

and/or fluid conditions in the experimental/natural case. As pointed out by Muto et al. (2011) replacement of the original crystal orientation by growth of more favourable (Y-maximum) orientations requires grain boundary migration, whereas the Rieserferner veins were deformed in a dominant SGR regime. At natural strain rates, the experimental conditions of Muto et al. (2011) likely extrapolate to temperatures slightly higher than those estimated for deformation in the Rieserferner quartz veins (i.e. ca. 450 °C). The dominance of SGR during shearing may also explain, in part, the presence of a CL banding in ultramylonites that we interpret as difference in Ti concentration between the different layers. As described by Bestmann and Pennacchioni (2015) dominant SGR is not efficient in completely resetting the Ti concentrations even at stages of pervasive deformation. The CL signature associated with the deformation microstructures of the Rieserferner veins are however suggestive of more water-rich conditions compared with the Sierra Nevada sample of Bestmann and Pennacchioni (2015).

681

682 **8. Conclusions**

683 Mylonitization of coarse grained quartz veins resulted in a complex evolution during deformation at
684 temperature of ~ 450 °C, in large part derived by the initially different crystallographic orientations
685 of the vein crystals. The following points summarize the main results of the study.

- 686 • Depending on the initial crystallographic orientations vein crystals manifested, in early
687 stages of shearing, different strengths resulting in distinct aspect ratios and degree of
688 incipient recrystallization of developing ribbon grains. The most favourably oriented
689 crystals were Y-type ones, indicative that {m}<a> was the easy slip system. Ribbons with c-
690 axis orthogonal to Y underwent early hardening and recrystallized along conjugate sets of
691 crystallographically-controlled μ SZs.
- 692 • Recrystallization in μ SZs initiated most likely by SGR. Once formed, new grains rotated
693 around Y (up to misorientations > 90°), accordingly with the μ SZ shear sense, since the
694 incipient μ SZ slip. Distorted ribbons show a similar (but lower) rotational spreading of

crystallographic axes. This rotational CPOs resulted from both the preferential activity of slip systems which formed subgrain boundaries with a misorientation axis coinciding with Y (especially in the host ribbon) and passive grain rotation.

- Grain rotation within the μ SZs was associated with the confined shear.
- Pervasive recrystallization and high shear strains were not capable of resetting the initial texture to a c-axis Y-maximum CPO as it would be expected from the evidence of the preferential activity of $\{m\}\langle a \rangle$ slip. Quartz ultramylonites show a domainal texture inherited from deformation and recrystallization of original crystals with a different CPO.
- In ultramylonites the misorientation angle/axis plots indicate that recrystallization by dominant SGR was assisted by the preferential activity of slip systems which formed subgrain boundaries with a misorientation axis parallel to Y, though $\{m\}\langle a \rangle$ was still the most efficient slip system, and/or passive rotation around Y.
- Within the different domains, grains with c-axis parallel to Y did not grow “rapidly” with increasing strain at the expenses of other grains in contrast to what is observed in the experiments of Muto et al. (2011). If a selective replacement by Y-grains of other grains did effectively occur with strain accumulation, the process was sluggish.
- The grain size of recrystallized grains does not depend significantly on (i) the amount of strain and degree of recrystallization; (ii) the CPO of the parent ribbon grain (protomylonite) or of the recrystallized layers (ultramylonite). This contrasts with the observation the inferred strength between ribbons and with the evidence of preferential $\{m\}\langle a \rangle$ slip.

Acknowledgements

Rudiger Kilian and Ren   Heilbronner are thanked for the assistance and guidance with the CIP analysis. Giulia Degli Alessandrini, Anna Rogowitz are thanked for discussion. Financial support from the University of Padova (“Progetto di Ateneo” CPDA140255) and from the Foundation “Ing. Aldo Gini” is acknowledged.

722 **Appendix – Methods and Analytical techniques**

723 **CIP Microscopy / Image Analysis / Microstructural feature quantification**

724 Computer-integrated polarization microscopy (CIP: Heilbronner and Pauli, 1993) was mainly aimed
725 at evaluating the c-axis orientation of the coarse grained ribbon protomylonites. The CIP
726 microphotographs were acquired on a Zeiss Axioplan, with attached a Basler Ace (acA1600-20gm)
727 camera, at the Institute of Geology and Paleontology of Basel University (Switzerland). Areas of 20
728 mm² were imaged with a resolution of ~ 3µm/pixel with a magnification of 2.5x each. To obtain a
729 bulk pole figure of representative areas of the thin section, microphotographs were stitched (with a
730 consequent decrease in resolution) and then processed with the CIP software suite for texture
731 analysis and orientation imaging. Crystallographic orientations are plotted on equal area, lower
732 hemisphere pole figures.

733 Optical images and processed EBSD maps were analysed in some cases with Paror and Surfor
734 (FABRIC software suite, Heilbronner and Barret, 2014) to estimate grain shapes, shape preferred
735 orientations and the orientation of µSZs (reported in rose diagram in Fig.4 and SOM1C)

736 Several scan images of the same thin section (no polarizer, crossed polarized, gypsum-plate inserted
737 and CIP images) have been compared and analysed by image analysis to define the areal extension
738 of each ribbon, its bulk c-axis orientation and its microstructural features (Aspect Ratio; AR;
739 Recrystallization amount: R_{exx}%, given as area fraction, Area%). These methods have some
740 limitation: (1) image optical resolution and the possibility to discern localized recrystallization
741 features. For example, R_{exx}% quantification (Fig. 2e) in those cases where the recrystallization is
742 localized it represent a good approximation of the real value, whereas where the recrystallization is
743 scattered and irregularly distributed all over the ribbon, this values represent a minimum estimation.
744 (2) Thin section dimensions commonly are too small to contain mm-cm ribbons. The reported AR
745 value (Fig. 2d) is therefore a minimum value of AR.

746 **EBSD analysis**

Electron backscattered diffraction analysis was carried out with: (i) FEG-SEM Zeiss 1540 EsB (Flamenco acquisition software, Oxford Instruments) at the Material Science Department – Geozentrum Nordbayern Erlangen; and (ii) JEOL 6610 LV SEM equipped with a NordLys Nano EBSD detector (AZTec acquisition software, Oxford Instruments); and (iii) JEOL 7001 FE SEM equipped with a NordLys Max EBSD detector (AZTec acquisition software, Oxford Instruments) at the Electron Microscope Centre of Plymouth University. Each thin section was SYTON-polished for at least 6 hours and carbon coated (about 3.5nm coating thickness). Analytical conditions, steps size, acquisition rates and other map characteristics are reported for each individual map in Table SOM1. All data have been processed (noise reduction following e.g. Bestmann and Prior, 2003) and analysed using CHANNEL5 software of HKL Technology, Oxford Instruments.

Monoclinic sample symmetry has been used. Quartz was the only mineral phase to be indexed, using trigonal symmetry (Laue group -3m). Critical misorientation for the distinction between low- and high-angle boundaries have been chosen at 15°, allowing grain boundary completion down to 0°. In addition, grain boundaries with 60°±5° of misorientation were disregarded from grain detection procedure, to avoid any contribution from Dauphiné twinning in the definition of grains.

The pole figures and the misorientation axis distributions in sample coordinates are equal area, lower hemisphere projections oriented with the general shear zone kinematics reference system (X = stretching lineation; Z = pole to general shear plane/vein boundary). The inverse pole figures for misorientation axis distribution in crystal coordinates are upper hemisphere projections.

Grain size analysis

Grain sizes are obtained from the grain detection routine in Channel5 Tango software. Equivalent grain diameters are obtained from grain area (μm^2). The minimum cut-off area below which grains are not considered have been set to 1 μm^2 ; therefore only grains composed of 4 to 9 pixels (according to map acquisition step-size) have been considered. Grain size data are then plotted as area-weighted distributions as frequency against square-root grain-size-equivalent grain diameters (as in Herweg and Berger 2004). The grain size distribution is close to a Gaussian distribution when

773 plotted in this way, therefore it gives us a good estimation of the mean grain size. The geometric
774 mean grain size is obtained graphically as the maximum frequency grain size of the distribution
775 curve. The distribution curve is obtained interpolating distribution data with a 6th degree polynomial
776 equation in Excel-MS Office. The arithmetic mean, instead, have been calculated directly from the
777 equivalent grain diameter database without any area-weighting process.

778 Subgrain size have been determined in the same way but, setting the critical misorientation at 2° in
779 Channel5 Tango grain detection routine. Then, only those subgrains useful for the analyses (those
780 close to the μ SZs) have been manually selected.

781

782

783 **References**

784 Bellieni, G., 1978. Caratteri geochemici del massiccio granodioritico tonalitico delle Vedrette di
785 Ries (Rieserferner) - Alto Adige Orientale. Rendiconti della Società Italiana di Mineralogia e
786 Petrologia 34, 527-548.

787 Berger, A., Herwegh, M., Schwarz, J. O., and Putlitz, B., 2011. Quantitative analysis of crystal/grain
788 sizes and their distributions in 2D and 3D. Journal of Structural Geology 33, 1751-1763.

789 Bestmann, M., Prior, D.J., 2003. Intragranular dynamic recrystallization in naturally deformed
790 calcite marble: diffusion accommodated grain boundary sliding as a result of subgrain rotation
791 recrystallization. Journal of Structural Geology 25, 1597-1613.

792 Bestmann, M., Pennacchioni, G., 2015. Ti distribution in quartz across a heterogeneous shear zone
793 within a granodiorite: The effect of deformation mechanism and strain on Ti resetting. Lithos 227,
794 37-56, doi:10.1016/j.lithos.2015.03.009.

795 Bouchez, J.-L., 1977. Plastic deformation of quartzites at low temperature in an area of natural
796 strain gradient. Tectonophysics 39, 25-50, doi:10.1016/0040-1951(77)90086-5.

797 Cesare, B., 1994. Hercynite as the product of staurolite decomposition in the contact aureole of
798 Vedrette di Ries, eastern Alps, Italy. Contributions to Mineralogy and Petrology 116, 239-246.

799 Dell'Angelo, L.N., Tullis, J., 1989. Fabric development in experimentally sheared quartzites.
800 Tectonophysics 169, 1-21.

801 Derez, T., Pennock, G., Drury, M., Sintubin, M., 2015. Low-temperature intracrystalline
802 deformation microstructures in quartz. Journal of Structural Geology 71, 3-23.

803 Gleason, G.C., Tullis, J., 1995. A flow law for dislocation creep of quartz aggregates determined
804 with the molten-salt cell. Tectonophysics 247, 1-23.

805 Gleason, G. C., Tullis, J., Heidelbach, F., 1993. The role of dynamic recrystallization in the

806 development of lattice preferred orientations in experimentally deformed quartz aggregates. *Journal*
807 *of Structural Geology* 15, 1145-1168.

808 Halfpenny, A., Prior, D. J., Wheeler, J., 2012. Electron backscatter diffraction analysis to determine
809 the mechanisms that operated during dynamic recrystallisation of quartz-rich rocks. *Journal of*
810 *Structural Geology* 36, 2-15.

811 Heilbronner, R. P., Pauli, C., 1993. Integrated spatial and orientation analysis of quartz c-axes by
812 computer-aided microscopy. *Journal of Structural Geology* 15, 369-382.

813 Heilbronner, R., Tullis, J., 2006. Evolution of c axis pole figures and grain size during dynamic
814 recrystallization: Results from experimentally sheared quartzite, *Journal of Geophysical Research*
815 111, B10202, doi:10.1029/ 2005JB004194.

816 Heilbronner, R., & Barrett, S. (2014). *Image analysis in earth sciences: microstructures and textures*
817 *of earth materials* . Springer Science & Business Media.

818 Heilbronner, R., Kilian, R., 2017. The grain size(s) of Black Hills Quartzite deformed in the
819 dislocation creep regime. *Solid Earth Discussion*, doi:10.5194/se-2017-30

820 Herwegh, M., & Berger, A., 2004. Deformation mechanisms in second-phase affected
821 microstructures and their energy balance. *Journal of structural geology* 26, 1483-1498.

822 Hirth, G., Teyssier, C., Dunlap, W.J., 2001. An evaluation of quartzite flow laws based on
823 comparisons between experimentally and naturally deformed rocks. *International Journal of Earth*
824 *Sciences* 90, 77-87, doi:10.1007/s005310000152

825 Hirth, G., Tullis, J., 1992. Dislocation creep regimes in quartz aggregates. *Journal of Structural*
826 *Geology* 14, 145-159.

827 Hobbs, B.E., 1968. Recrystallization of single crystals of quartz. *Tectonophysics* 6, 353-401.

828 Kilian, R., Heilbronner, R., Stünitz, H., 2011. Quartz grain size reduction in a granitoid rock and the
829 transition from dislocation to diffusion creep. *Journal of Structural Geology* 33, 1265-1284,

830 doi:10.1016/j.jsg.2011.05.004

831 Kj  ll, H.J., Viola, G., Menegon, L., S  rensen, B.E., 2015. Brittle–viscous deformation of vein
832 quartz under fluid-rich low greenschist facies conditions. *Solid Earth* 7, 213-257.

833 Lloyd, G. E., Law, R. D., Mainprice, D., Wheeler, J., 1992. Microstructural and crystal fabric
834 evolution during shear zone formation. *Journal of Structural Geology* 14, 1079-1100.

835 Lloyd, G. E., 2004. Microstructural evolution in a mylonitic quartz simple shear zone: the
836 significant roles of dauphine twinning and misorientation. *Geological Society of London, Special*
837 *Publications* 224, 39-61.

838 Luan, F.C., Paterson, M.S. ,1992. Preparation and deformation of synthetic aggregates of quartz.
839 *Journal of Geophysical Research* 97, 301-320.

840 Mancktelow, N.S., 1981. Strain variation between quartz grains of different crystallographic
841 orientation in a naturally deformed metasiltstone. *Tectonophysics* 78, 73-84.

842 Mancktelow, N.S., St  ckli, D.F., Grollimund, B., M  ller, W., F  genschuh, B., Viola, G., Villa, I. M.,
843 2001. The DAV and Periadriatic fault systems in the Eastern Alps south of the Tauern window.
844 *International Journal of Earth Sciences* 90, 593-622.

845 Mancktelow, N.S., Pennacchioni, G., 2004. The influence of grain boundary fluids on the
846 microstructure of quartz-feldspar mylonites. *Journal of Structural Geology* 26, 47-69.

847 Mancktelow, N.S., Pennacchioni, G., 2005. The control of precursor brittle fracture and fluid–rock
848 interaction on the development of single and paired ductile shear zones. *Journal of Structural*
849 *Geology* 27, 645-661.

850 Mancktelow, N.S., Pennacchioni, G., 2010. Why calcite can be stronger than quartz. *Journal of*
851 *Geophysical Research* 115, B01402, doi:10.1029/2009JB006526.

852 Menegon, L., Pennacchioni, G., Heilbronner, R., Pittarello, L., 2008. Evolution of quartz
853 microstructure and c-axis crystallographic preferred orientation within ductilely deformed

854 granitoids (Arolla unit, Western Alps). *Journal of Structural Geology* 30, 1332-1347.

855 Menegon, L., Pennacchioni, G., 2010. Local shear zone pattern and bulk deformation in the Gran
856 Paradiso metagranite (NW Italian Alps). *International Journal of Earth Sciences* 99, 1805-1825,
857 doi:10.1007/s00531-009-0485-6

858 Menegon, L., Piazzolo, S., Pennacchioni, G., 2011. The effect of Dauphiné twinning on plastic strain
859 in quartz. *Contributions to Mineralogy and Petrology* 161, 635-652.

860 Menegon, L., Stünitz, H., Nasipuri, P., Heilbronner, R., Svahnberg, H., 2013. Transition from
861 fracturing to viscous flow in granulite facies perthitic feldspar (Lofoten, Norway). *Journal of*
862 *Structural Geology* 48, 95-112.

863 Morales, L. F., Mainprice, D., Lloyd, G. E., Law, R. D., 2011. Crystal fabric development and slip
864 systems in a quartz mylonite: an approach via transmission electron microscopy and viscoplastic
865 self-consistent modelling. *Geological Society of London, Special Publications* 360, 151-174.

866 Muto, J., Hirth, G., Heilbronner, R., Tullis, J., 2011. Plastic anisotropy and fabric evolution in
867 sheared and recrystallized quartz single crystals. *Journal of Geophysical Research* 116, B02206,
868 doi:10.1029/2010JB007891

869 Neumann, B., 2000. Texture development of recrystallised quartz polycrystals unravelled by
870 orientation and misorientation characteristics. *Journal of Structural Geology* 22, 1695-1711.

871 Pauli, C., Schmid, S. M., Heilbronner, R. P., 1996. Fabric domains in quartz mylonites: localized
872 three dimensional analysis of microstructure and texture. *Journal of Structural Geology* 18, 1183-
873 1203.

874 Pennacchioni, G., Di Toro, G., Mancktelow, N.S., 2001. Strain-insensitive preferred orientation of
875 porphyroclasts in Mont Mary mylonites. *Journal of Structural Geology* 23, 1281-1298, doi:
876 10.1016/S0191-8141(00)00189-9

877 Pennacchioni, G., 2005. Control of the geometry of precursor brittle structures on the type of ductile

878 shear zone in the Adamello tonalites, Southern Alps (Italy). *Journal of Structural Geology* 27, 627-
879 644.

880 Pennacchioni, G., Mancktelow, N.S., 2007. Nucleation and initial growth of a shear zone network
881 within compositionally and structurally heterogeneous granitoids under amphibolite facies
882 conditions. *Journal of Structural Geology* 29, 1757-1780.

883 Pennacchioni, G., Menegon, L., Leiss, B., Nestola, F., Bromiley, G., 2010. Development of
884 crystallographic preferred orientation and microstructure during plastic deformation of natural
885 coarse-grained quartz veins. *Journal of Geophysical Research, Solid Earth* 115, B12405, doi:
886 10.1029/2010JB007674.

887 Pennacchioni, G., Zucchi, E., 2013. High temperature fracturing and ductile deformation during
888 cooling of a pluton: The Lake Edison granodiorite (Sierra Nevada batholith, California). *Journal of*
889 *Structural Geology* 50, 54-81.

890 Piazzolo, S., Montagnat, M., Blackford, J.R., 2008. Sub-structure characterization of experimentally
891 and naturally deformed ice using cryo-EBSD. *Journal of Microscopy* 230, 509-519.

892 Price, N. A., Song, W. J., Johnson, S. E., Gerbi, C. C., Beane, R. J., West, D. P., 2016.
893 Recrystallization fabrics of sheared quartz veins with a strong pre-existing crystallographic
894 preferred orientation from a seismogenic shear zone. *Tectonophysics* 682, 214-236.

895 Prior, D. J., Wheeler, J., Peruzzo, L., Spiess, R., Storey, C., 2002. Some garnet microstructures: an
896 illustration of the potential of orientation maps and misorientation analysis in microstructural
897 studies. *Journal of Structural Geology* 24, 999-1011.

898 Rahl, J. M., Skemer, P., 2016. Microstructural evolution and rheology of quartz in a mid-crustal
899 shear zone. *Tectonophysics* 680, 129-139.

900 Ramsay, J.G., 1980. Shear zone geometry: a review. *Journal of Structural Geology* 2, 83-99.

901 Ranalli, G., 2000. Rheology of the crust and its role in tectonic reactivation. *Journal of*

902 Geodynamics 30, 3–15.

903 Rogowitz, A., White, J. C., Grasemann, B., 2016. Strain localization in ultramylonitic marbles by
 904 simultaneous activation of dislocation motion and grain boundary sliding (Syros, Greece). *Solid*
 905 *Earth* 7, 355-366, doi:10.5194/se-7-355-2016

906 Romer, R.L., Siegesmund, S., 2003. Why allanite may swindle about its true age. *Contributions to*
 907 *Mineralogy and Petrology* 146, 297-307.

908 Rosenberg, C., 2004. Shear zones and magma ascent: a model based on a review of the Tertiary
 909 magmatism in the Alps. *Tectonics* 23, TC3002, doi:10.1029/2003TC001526

910 Schmid, S.M., Casey, M., 1986. Complete fabric analysis of some commonly observed quartz c-
 911 axis patterns. In: *Mineral and Rock Deformation: Laboratory Studies – The Paterson Volume* (eds
 912 B. E. Hobbs & H. C. Heard), pp. 263–86. American Geophysical Union, Geophysical Monograph
 913 vol. 36. Washington, DC, USA.

914 Steenken, A., Siegesmund, S., Heinrichs, T., 2000. The emplacement of the Rieserferner Pluton
 915 (Eastern Alps, Tyrol): constraints from field observations, magnetic fabrics and microstructures.
 916 *Journal of Structural Geology* 22, 1855-1873.

917 Stipp, M., Kunze, K., 2008. Dynamic recrystallization near the brittle-plastic transition in naturally
 918 and experimentally deformed quartz aggregates. *Tectonophysics* 448, 77-97.

919 Stipp, M., Tullis, J., 2003. The recrystallized grain size piezometer for quartz. *Geophysical*
 920 *Research Letters* 30, 2088, doi:10.1029/2003GL018444, 2003

921 Stipp, M., Stünitz, H., Heilbronner, R., Schmid, S.M., 2002. The Eastern Tonale fault zone: A
 922 “natural laboratory” for crystal plastic deformation of quartz over a temperature range from 250 °C
 923 to 700 °C. *Journal of Structural Geology* 24, 1861-1884, doi:10.1016/S0191-8141(02)00035-4.

924 Stünitz, H., Gerald, J. F., Tullis, J., 2003. Dislocation generation, slip systems, and dynamic
 925 recrystallization in experimentally deformed plagioclase single crystals. *Tectonophysics*, 372, 215-

926 233.

927 ten Grotenhuis, S.M., Passchier, C.W., Bons, P.D., 2002. The influence of strain localisation on the
928 rotation behaviour of rigid objects in experimental shear zones. *Journal of Structural Geology* 24,
929 485-499.

930 Toy, V.G., Prior, D.J., Norris, R.J., 2008. Quartz fabrics in the Alpine Fault mylonites: Influence of
931 pre-existing preferred orientations on fabric development during progressive uplift. *Journal of*
932 *Structural Geology* 30, 602-621, doi:10.1016/j.jsg.2008.01.001.

933 Trepmann, C.A., Stöckhert, B., Dorner, D., Moghadam, R. H., Küster, M., Röller, K., 2007.
934 Simulating coseismic deformation of quartz in the middle crust and fabric evolution during
935 postseismic stress relaxation – an experimental study. *Tectonophysics*, 442, 83-104.

936 Trepmann, C.A., Hsu, C., Hentschel, F., Döhler, K., Schneider, C., Wichmann, V., 2017.
937 Recrystallization of quartz after low-temperature plasticity – The record of stress relaxation below
938 the seismogenic zone. *Journal of Structural Geology*, 95, 77-92.

939 Tullis, J., 1977. Preferred orientation of quartz produced by slip during plane strain. *Tectonophysics*
940 39, 87-102.

941 Tullis, J., Christie, J., Griggs, D., 1973. Microstructures and preferred orientations of
942 experimentally deformed quartzites. *Geological Society of America Bulletin* 84, 297-314.

943 van Daalen, M., Heilbronner, R., Kunze, K., 1999. Orientation analysis of localized shear
944 deformation in quartz fibres at the brittle–ductile transition. *Tectonophysics* 303, 83-107.

945 Vernooij, M.G., 2005. Dynamic recrystallisation and microfabric development in single crystals of
946 quartz during experimental deformation (Doctoral dissertation, Diss., Naturwissenschaften,
947 Eidgenössische Technische Hochschule ETH Zürich, Nr. 16050, 2005).

948 Vernooij, M.G., Kunze, K., den Brok, B., 2006a. ‘Brittle’ shear zones in experimentally deformed
949 quartz single crystals. *Journal of Structural Geology* 28, 1292-1306.

950 Vernooij, M.G., den Brok, B., Kunze, K., 2006b. Development of crystallographic preferred
 951 orientations by nucleation and growth of new grains in experimentally deformed quartz single
 952 crystals. *Tectonophysics* 427, 35-53.

953 Vollbrecht, A., Stipp, M., Olesen, N. Ø., 1999. Crystallographic orientation of microcracks in quartz
 954 and inferred deformation processes: a study on gneisses from the German Continental Deep Drilling
 955 Project (KTB). *Tectonophysics* 303, 279-297.

956 Wagner, R., Rosenberg, C.L., Handy, M.R., Möbus, C., Albrecht, M., 2006. Fracture-driven intrusion
 957 and upwelling of a mid-crustal pluton fed from a transpressive shear zone - The Rieserferner Pluton
 958 (Eastern Alps). *Geological Society of America Bulletin* 118, 219-237.

959

960 **Figure captions**

961 Fig. 1 - Polished slabs of sheared quartz veins of the Rieserferner pluton. The vein boundary is
962 horizontal and the sense of shear is dextral (as can be inferred from the internal oblique foliation)
963 for all samples. (a) Protomylonite showing a coarse, irregularly developed foliation defined by
964 elongated to ribbon grains. The mean foliation inclination indicates a bulk shear strain $\gamma \simeq 1$. (b)
965 Mylonitic vein with a more homogeneous oblique foliation corresponding to a bulk shear strain $\gamma \simeq$
966 3.4. (c) Ultramylonitic vein within a weakly deformed host tonalite localizing shear strain $\gamma > 10$.

967 Fig. 2 - Microstructure and CPO of protomylonitic quartz vein. (a) Optical microphotograph
968 (crossed polarizers and inserted gypsum plate) of a thin section from the protomylonite shown in
969 Fig. 1a. (b) Sketch drawn from (a) showing the different ribbons (in different colours) and incipient
970 recrystallization aggregates (in black colour). The ribbons are colour-coded as a function of the
971 dominant c-axis orientation determined by CIP analysis, accordingly with the Look-Up Table
972 (LUT) reported in (c). (c) Pole figure (with a coloured LUT background) of the c-axis orientations
973 (small black circles) of the ribbons in the 2 analysed thin sections of protomylonite (see also Fig.
974 SOM1). The dashed line represents the trace of the average ribbon elongation. (d) Aspect ratios for
975 the different ribbon orientations. The aspect ratio values larger and lower than the mean value (6~7)
976 are evidenced in black and red characters, respectively. Underlined bold values represent actual
977 aspect ratios for ribbons completely included within the thin section. (e) Area fractions of
978 recrystallized aggregates for to the different c-axis orientations of the host ribbons. The red and
979 black values represent values larger and smaller than the bulk sample recrystallization (~10%),
980 respectively. High values occur mostly along the periphery of the pole figure. Low values dominate
981 close to the centre of the pole figure.

982 Fig. 3 – Optical microstructures of ribbons in the protomylonite with a schematic representation of
983 the [c] axis orientation determined by CIP analysis (lower-left pole figures). (a) Cross-polarized
984 microphotograph of a dark-gray to black Y-type ribbon almost free of recrystallization. (b) Cross-
985 polarized microphotograph of a Z-type ribbon with sharp longitudinal discontinuities sub-parallel to

the ribbon elongation and incipient recrystallization. Recrystallization occurred along the sharp discontinuities (some are indicated by white arrows) and, in the most strained part of the ribbon (down right), along conjugate microshear zones dominated by a synthetic Riedel-type set. (c) Microphotograph (crossed polarizers and inserted gypsum plate) of a XZa-type ribbon showing two sets of μ SZs. (d) Cross-polarized microphotograph of XZb-type ribbon with two sets of μ SZs. (e) CIP-derived c-axis orientation map of the microstructure in (c) coloured according to the LUT (equal area, lower hemisphere). (f) CIP-derived c-axis orientation map of the microstructure in (d) coloured according to the LUT. (g) c-axis CPO of the domain in (e) determined by CIP. (h) c-axis CPO of the domain in (f) determined by CIP.

Fig. 4 – Analysis of the orientations of fine-grained recrystallized aggregates in some ribbons of the protomylonite of Fig. 2b. A similar analysis of the 2nd studied protomylonite sample is reported in Fig. SOM1c. The orientations of the μ SZs in the selected areas (surrounded by the dashed line and showing un-blurred colour) are shown in the rose diagrams.

Fig. 5 – Optical microstructures and c-axis orientation map (from CIP) of a quartz mylonite and ultramylonite. (a) Circular polarization microphotograph of mylonite showing the alternation of un-recrystallized to partly recrystallized ribbons and lens-shaped domains, and completely recrystallized matrix. (b) c-axis orientation map (from CIP analysis) of the image in (a) showing the LUT in the lower left corner. (c) CIP-determined c-axis pole figures for non recrystallized ribbons of (b). (d) CIP-determined c-axis pole figure for recrystallized matrix of (b). (e) Cross-polarized microphotograph of a pervasively recrystallized quartz ultramylonite showing an extinction banding of the matrix, very elongated ribbons and small un-recrystallized ribbon porphyroclasts. (f) c-axis orientation map (from CIP analysis) of the image in (e) showing the LUT in the lower left corner. (g) CIP-determined c-axis pole figures of the ultramylonite in (f).

Fig. 6 - EBSD analysis of a Y-type ribbon. (a) Orientation map of the ribbon colour-coded according to the inverse pole figure in the lower right corner. Subgrain boundaries are colour-coded as a function of misorientations according to the legend in the upper left corner. (b) Pole figures for

1012 the orientations of $[c]$, $\langle a \rangle$ and $\{m\}$ crystallographic directions; (c) Misorientation axis distribution
 1013 in crystal (upper row) and sample (lower row) coordinate system for both low ($2-15^\circ$) and high
 1014 angle misorientations ($15-104^\circ$). (d) Scheme of misorientation axis distribution in crystal
 1015 coordinate system for hexagonal quartz showing the most common slip systems (edge dislocations)
 1016 for the different misorientation axes (redrawn from Neumann, 2000). (e) Optical microphotographs
 1017 (crossed polarizers) of the domain mapped in (a) (included in the white box).

1018 Fig. 7 - EBSD orientation imaging and data for an XZa-type ribbon, and included μ SZs, in a
 1019 protomylonite. (a) Orientation map colour-coded according to the inverse pole figure shown in the
 1020 upper right corner. Boundaries are colour-coded as a function of misorientations according to the
 1021 same legend in Fig. 6a. (b) Pole figures for the host ribbon showing the orientations of $[c]$, $\langle a \rangle$ and
 1022 $\{r\}$ crystallographic directions. Note the parallelism between one of the $\{r\}$ crystallographic plane
 1023 and the μ SZ trace (red line). (c) Pole figures ($[c]$, $\langle a \rangle$ and $\{m\}$ crystallographic directions) for the
 1024 recrystallized aggregate along the evolved μ SZ δ . (d) Pole figures ($[c]$, $\langle a \rangle$ and $\{m\}$
 1025 crystallographic directions) for the mature μ SZ in the lower part of the map (a). (e) Misorientation
 1026 axis distributions for low ($2-15^\circ$) and high ($15-104^\circ$) misorientation angles and in sample
 1027 coordinates for the host ribbon. (f) Misorientation axis distributions for low ($2-15^\circ$), intermediate
 1028 ($15-45^\circ$) and high ($45-104^\circ$) misorientation angles in crystal and sample coordinates for the evolved
 1029 μ SZ δ . (g) Misorientation axis distributions for low ($2-15^\circ$), intermediate ($15-45^\circ$) and high ($45-$
 1030 104°) misorientation angles in crystal and sample coordinates for the mature μ SZ ϵ . (h) Optical
 1031 microphotographs (crossed polarizers) of the domain mapped in (a) (included in the red box).

1032 Fig. 8 - EBSD orientation imaging and data of XZb-type ribbon, and included incipient to evolved
 1033 μ SZs. (a) Crystallographic orientation map with inverse pole figure (IPF) for colour-coding (with
 1034 respect to the X kinematic direction). The ribbon includes 2 incipient μ SZs (α and β) with antithetic
 1035 (left-lateral) sense of shear, and a main synthetic (right-lateral) evolved μ SZ (ϕ). (b) Pole figures
 1036 ($[c]$, $\{m\}$ and $\{r\}$ crystallographic orientations) for the host ribbon including the orientations (bold
 1037 lines) of the μ SZs (blue: α ; green: β ; red: ϕ). (c) Pole figure of the c-axis orientations (one-point-

per-grain) for recrystallized grains in the incipient μ SZs α and β , (d) Pole figures of c- and a-axis orientations (one-point-per-grain) for recrystallized grains in the evolved μ SZ ϕ . (e) Misorientation axis distributions for low (2-15°) and high (15-104°) misorientations in crystal and sample coordinates for the host ribbon. (f) Misorientation axis distributions (for the misorientation range 2-15°) in crystal and sample coordinates for two selected areas (1) and (2) shown in the orientation map (a). (g) Misorientation axis distributions for low (2-15°), intermediate (15-45°) and high (45-104°) misorientations in crystal and sample coordinates for the evolved μ SZ δ . (h) Optical microphotographs (crossed polarizers) of the domain (included in the red box) shown in the EBSD map (a).

1047

Fig. 9 - Misorientation angle distributions (MAD) for correlated (blue curve) and uncorrelated misorientations (red curve). The thin black curve represents the theoretical random distribution for any trigonal point group. M is the misorientation index. (a) Host Y-type ribbon of Fig. 6. (b) Host XZa-type ribbon of Fig. 7. (c) Host XZb-type ribbon of Fig. 8. (d) Host XZa-type ribbon of Fig. 7. (e) Evolved μ SZ δ of Fig. 7. (f) Mature μ SZ ε of Fig. 7. (g) Evolved μ SZ ϕ of Fig. 8. (h) Mature μ SZ of Fig. 9. (i) Ultramylonite of Fig. 11.

Fig. 10 - EBSD orientation imaging and data for the quartz ultramylonite. (a) Orientation map colour-coded according to the inverse pole figure shown below. The white solid lines bound domains (I-IV) with a different CPO analysed individually. The dashed white lines encompass quartz ribbon porphyroclasts (b)-(h) c-axis pole figures (1st column), pole figures for low angle misorientations (2nd column) and high angle misorientations (3rd column), and misorientations axis plots in sample coordinates for low (4th column) and high angle misorientations (5th column). In the pole figures, data are reported as one-point-per-grain except for (g) ; (i) Crossed polarizer microphotograph of the ultramylonite (red box indicate the analysed area).

1062

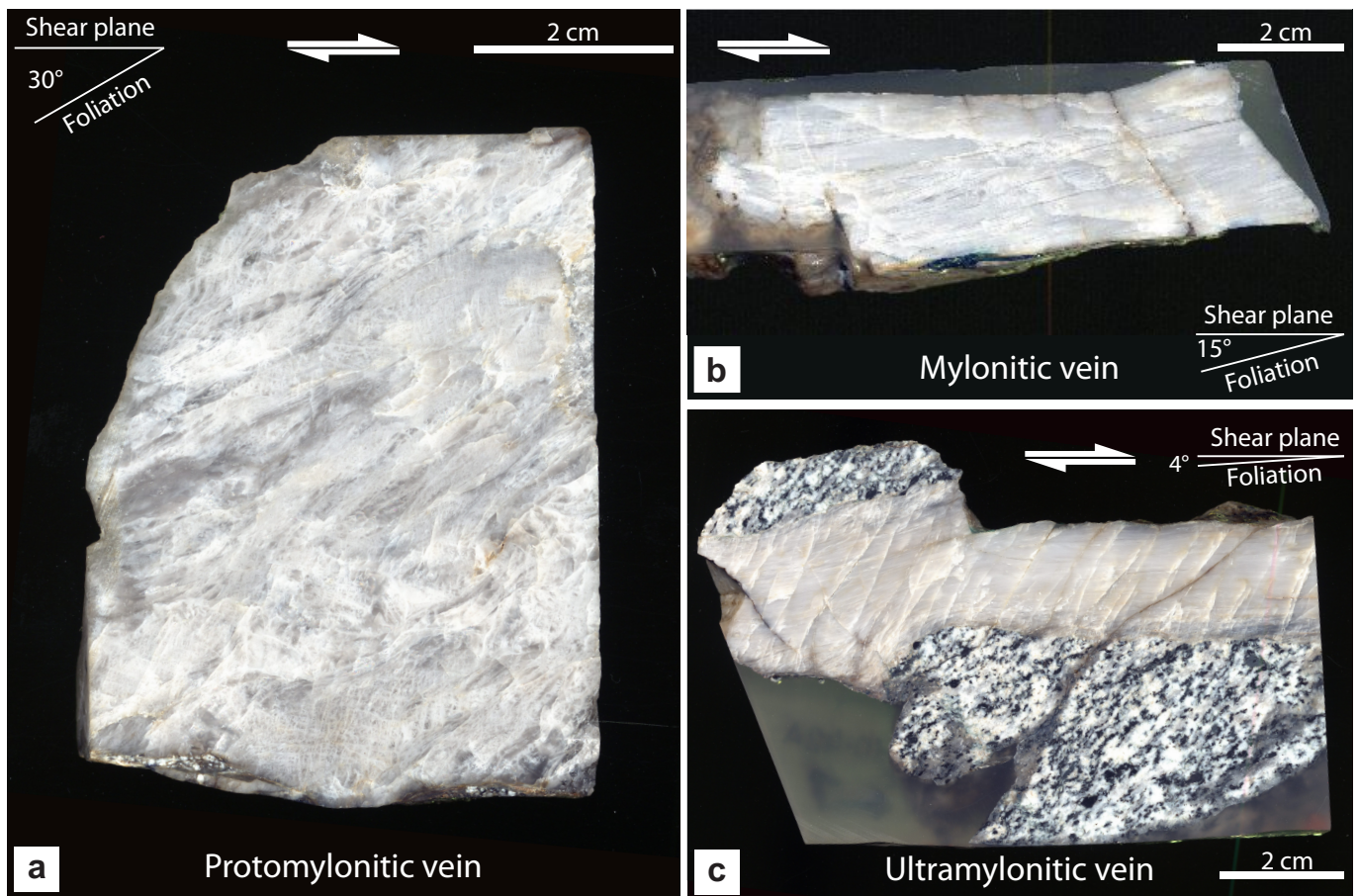


Figure 1

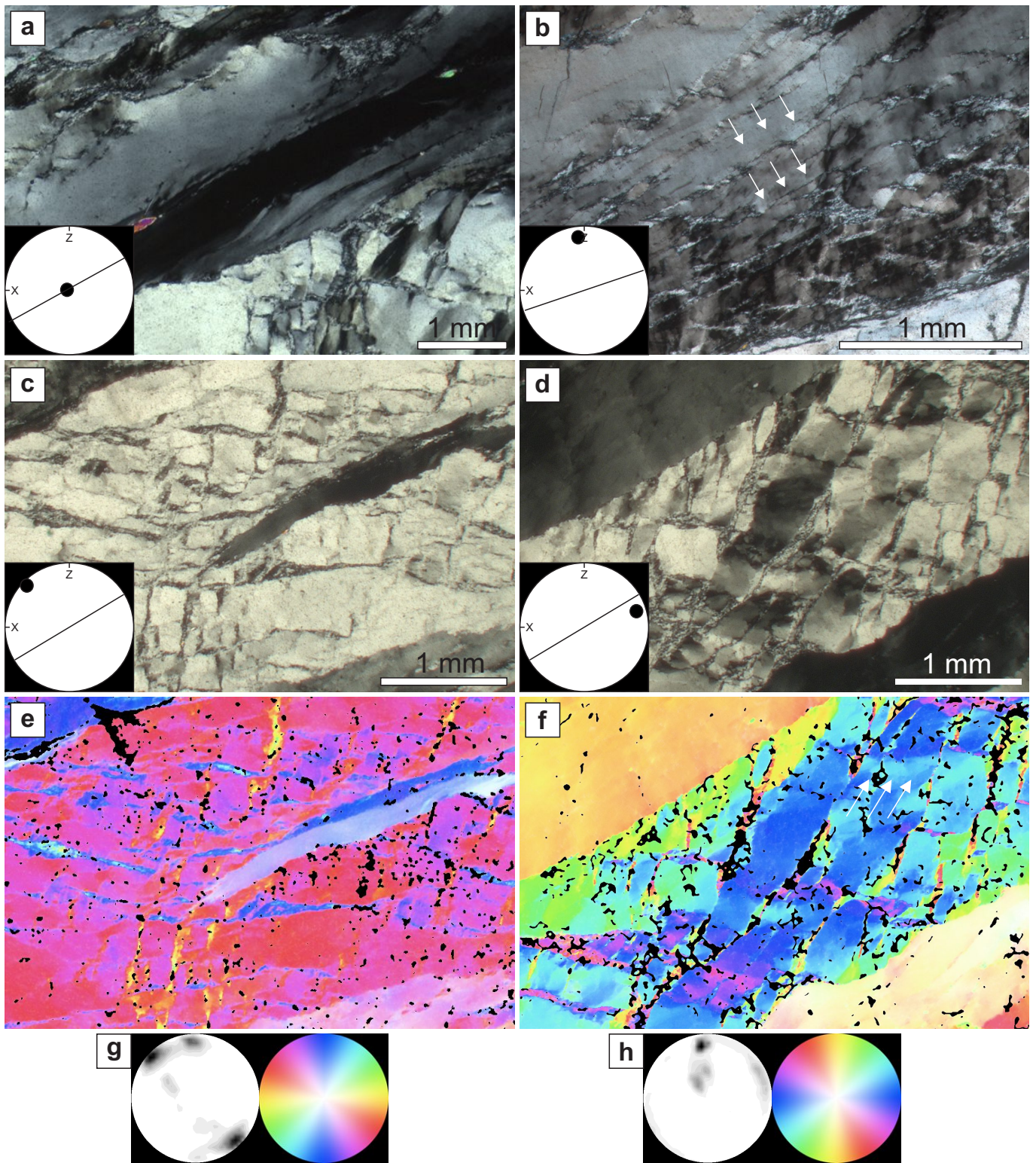


Figure 3

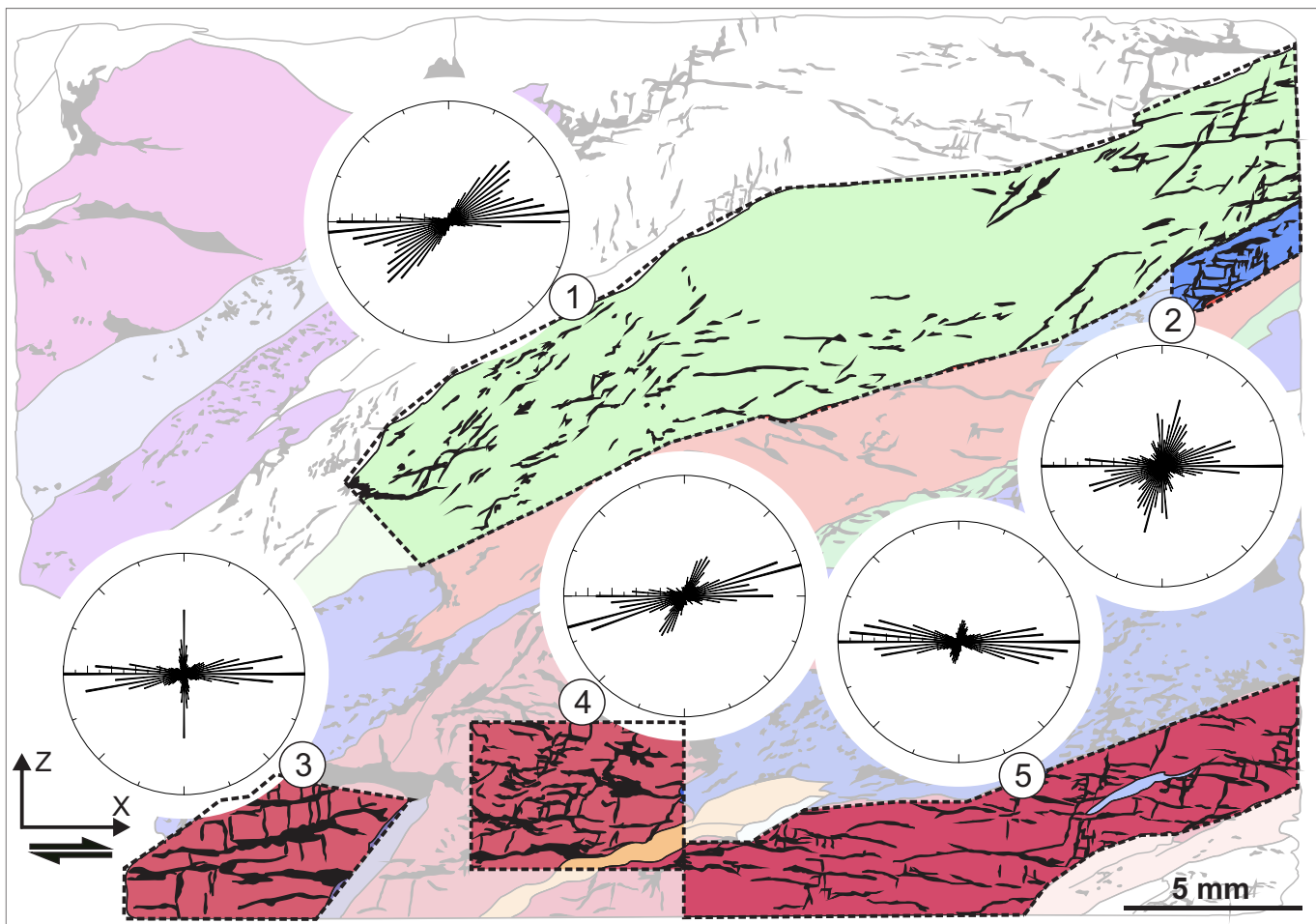


Figure 4

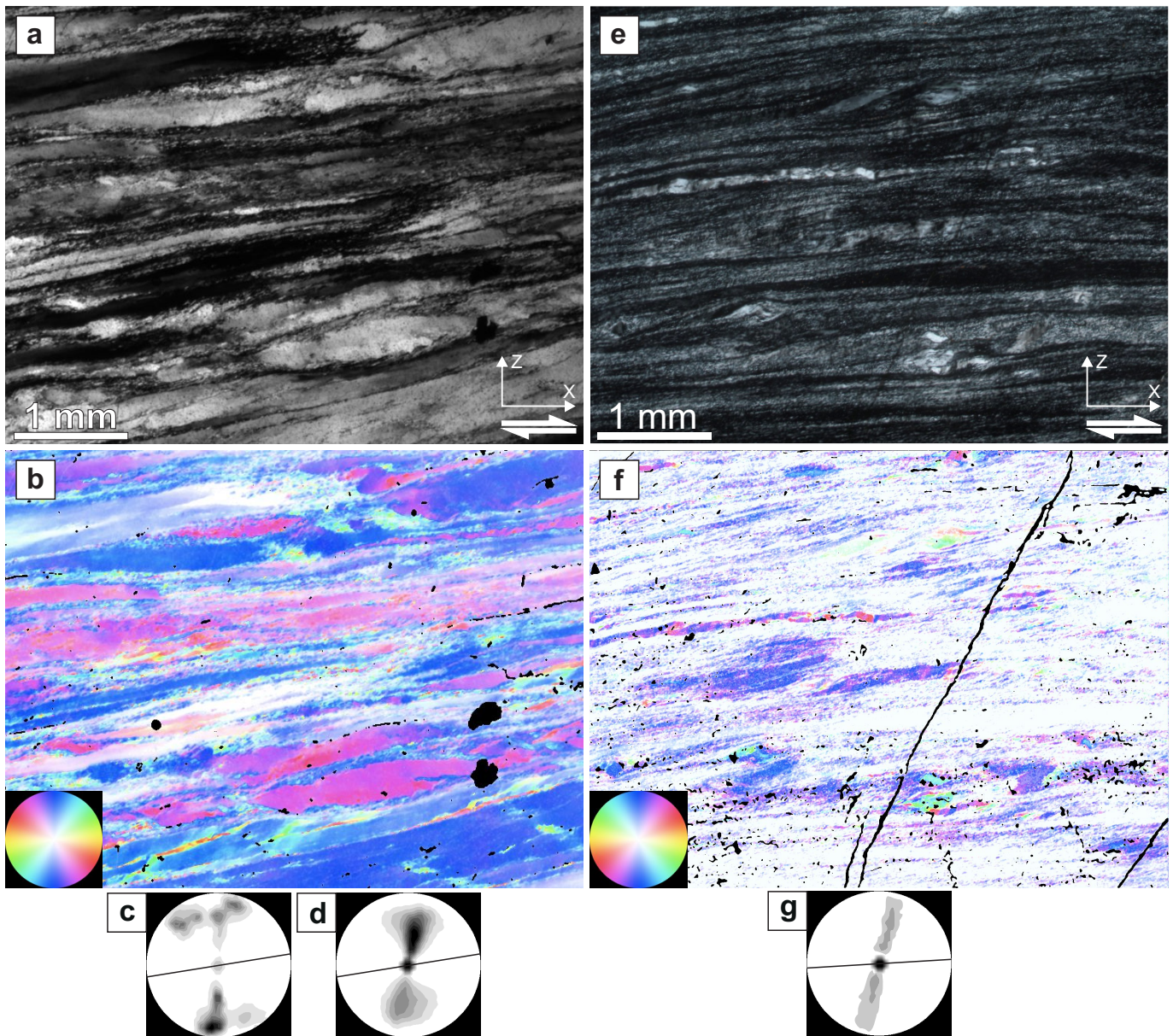


Figure 5

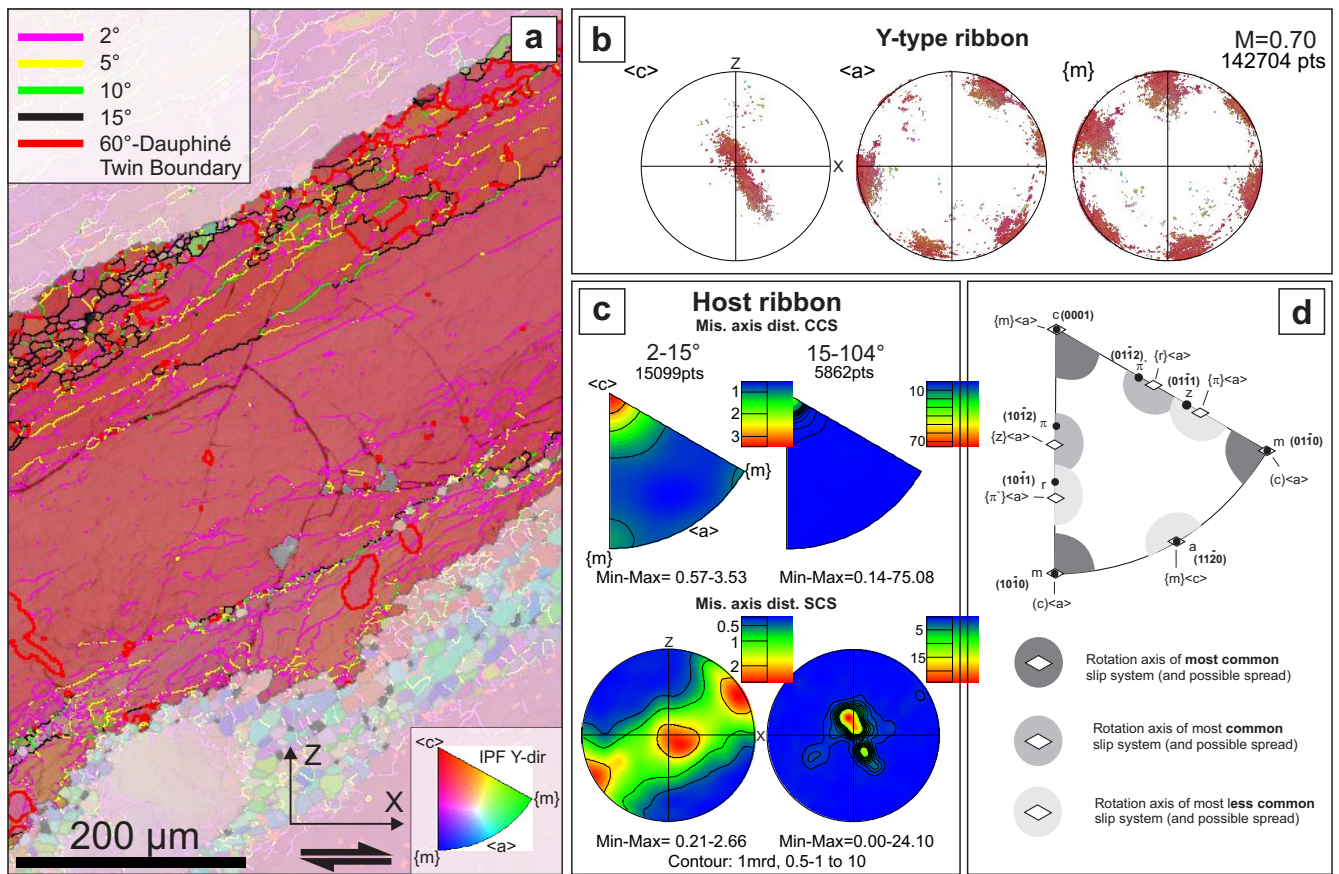


Figure 6

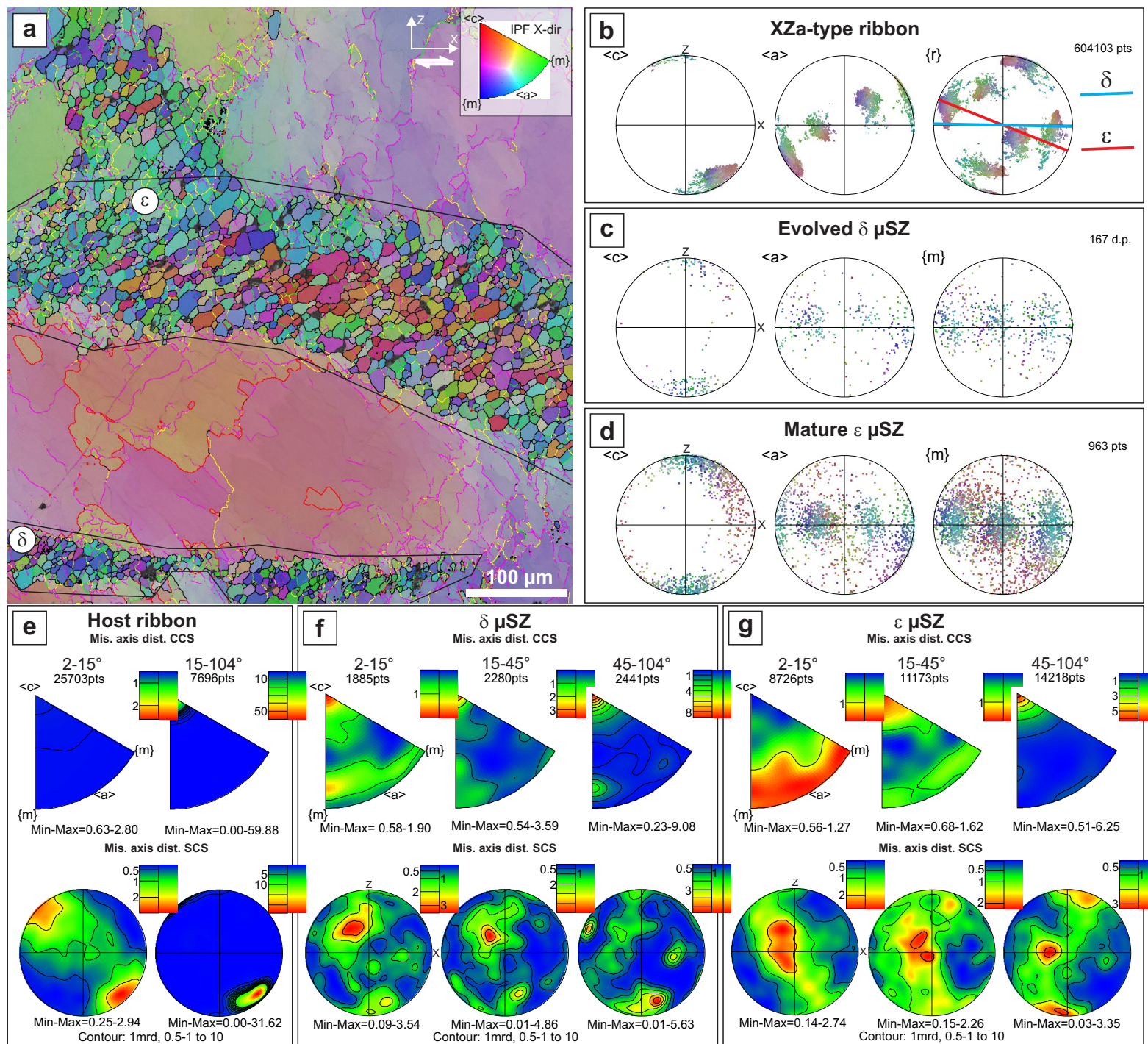


Figure 7

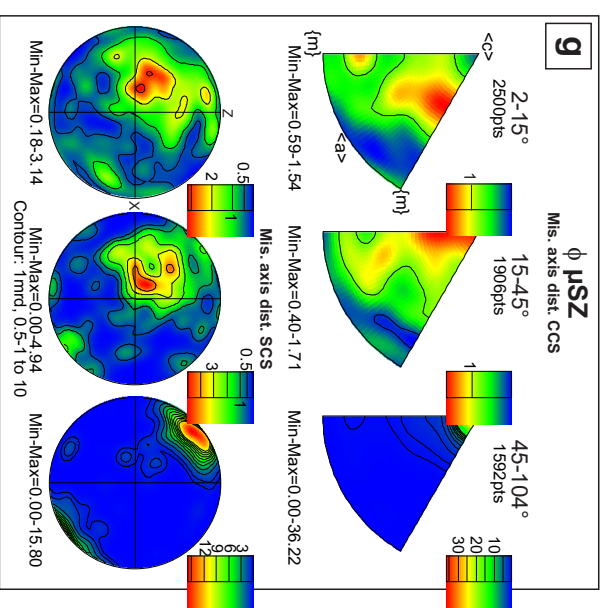
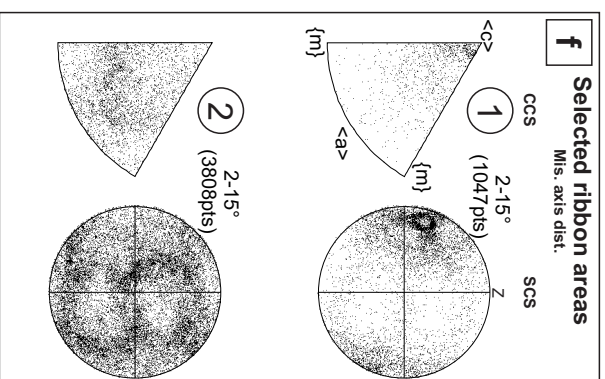
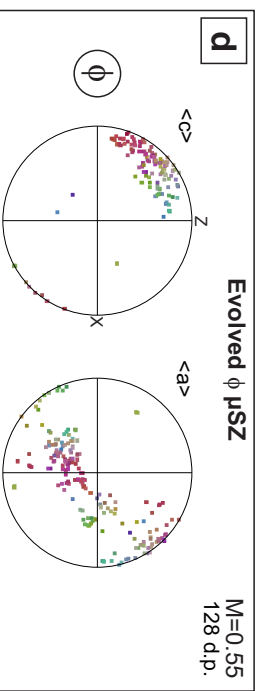
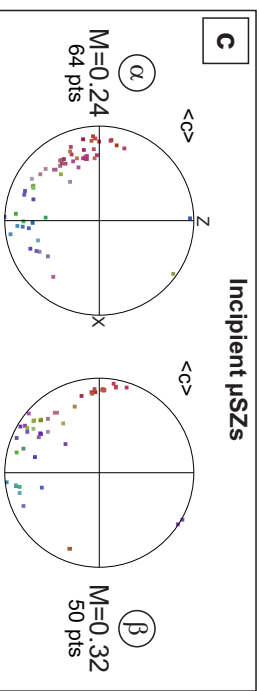
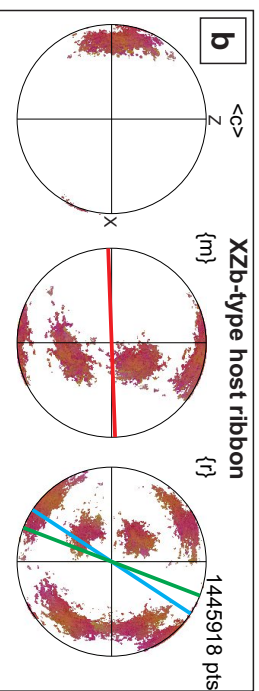
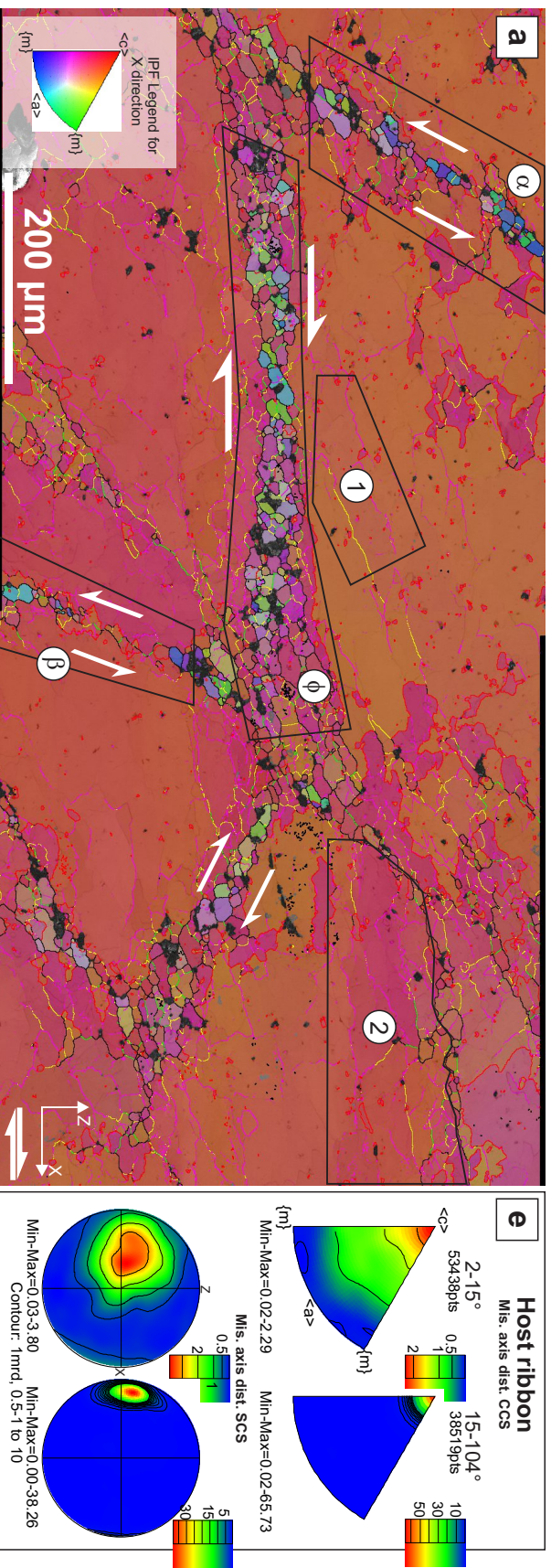


Figure 8

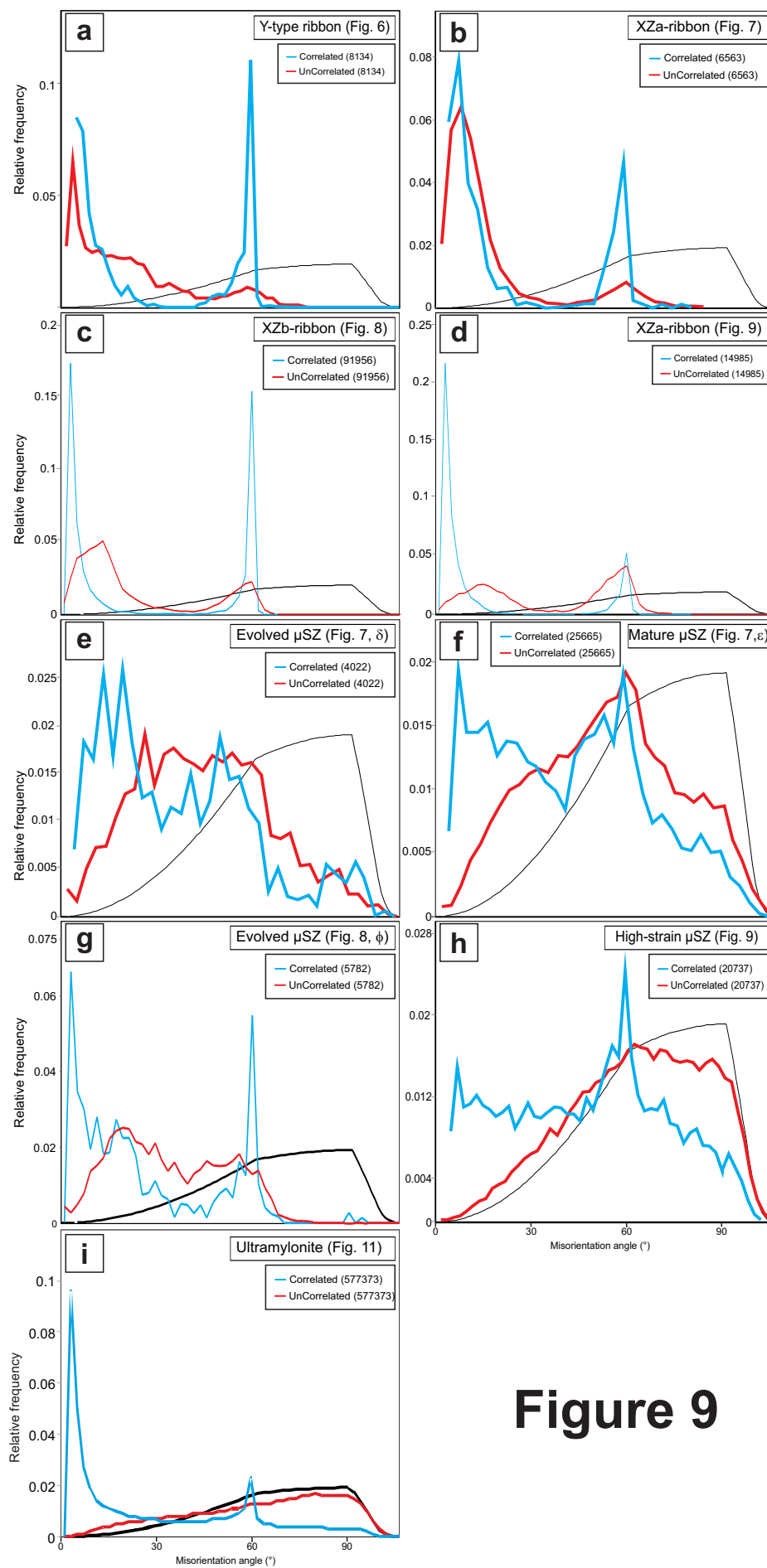


Figure 9

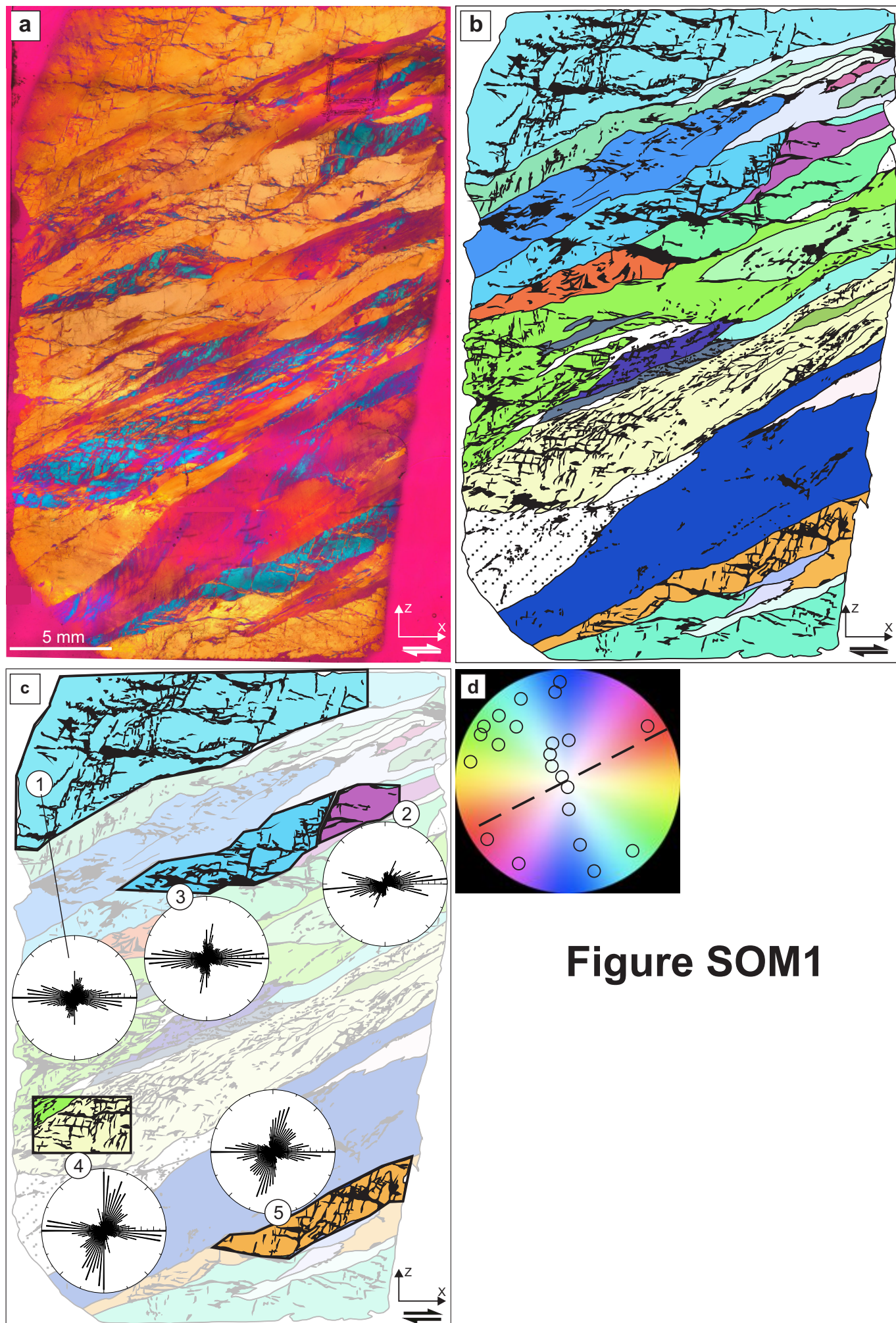


Figure SOM1

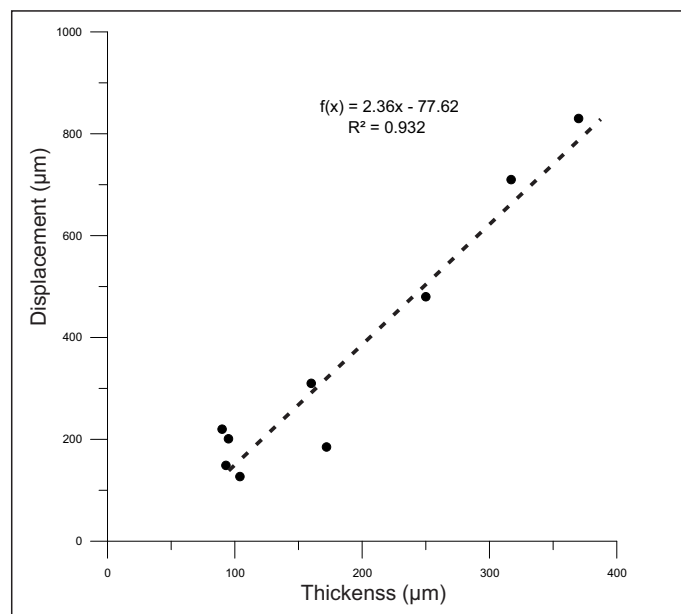


Figure SOM2

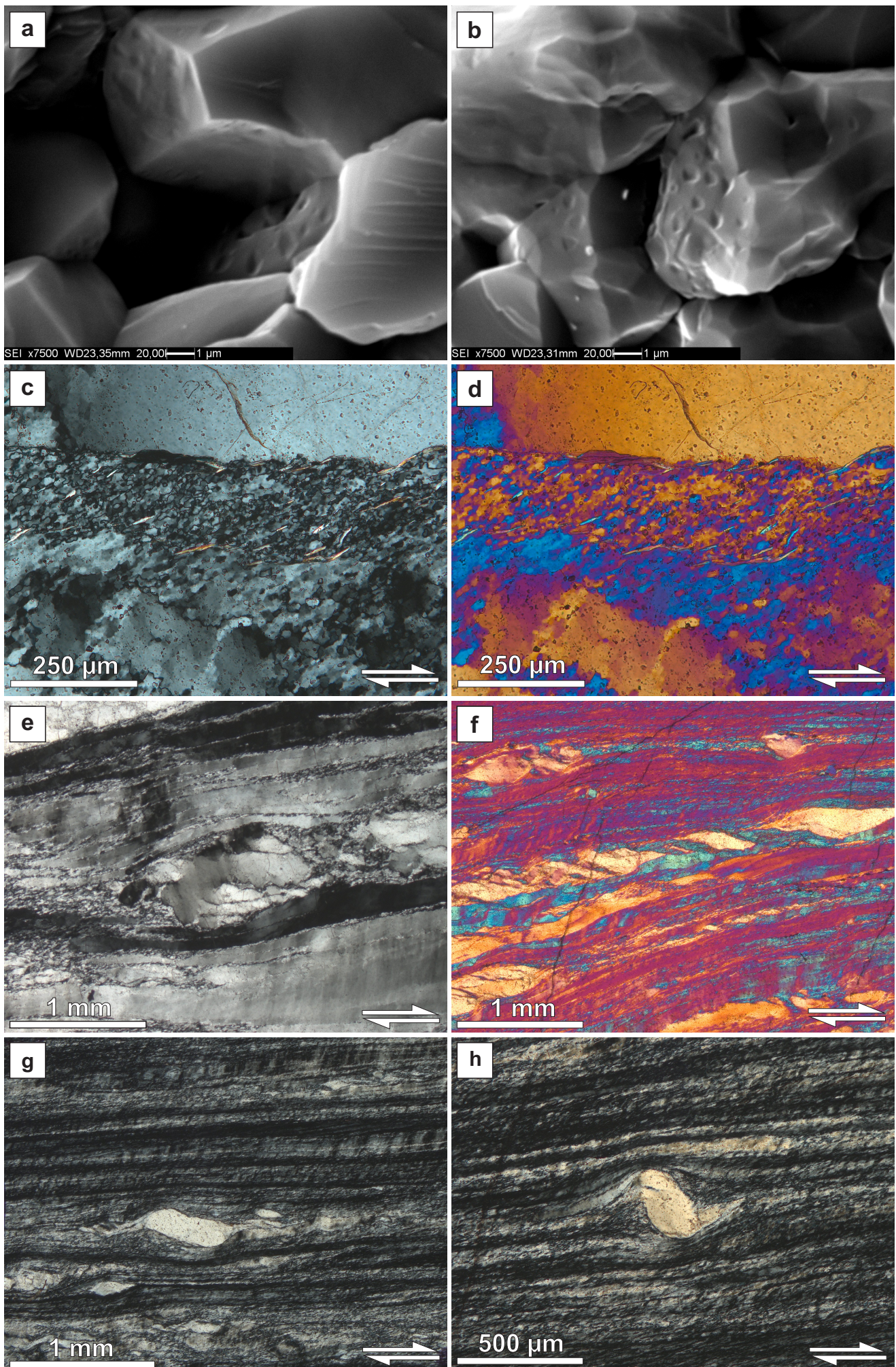


Figure SOM3

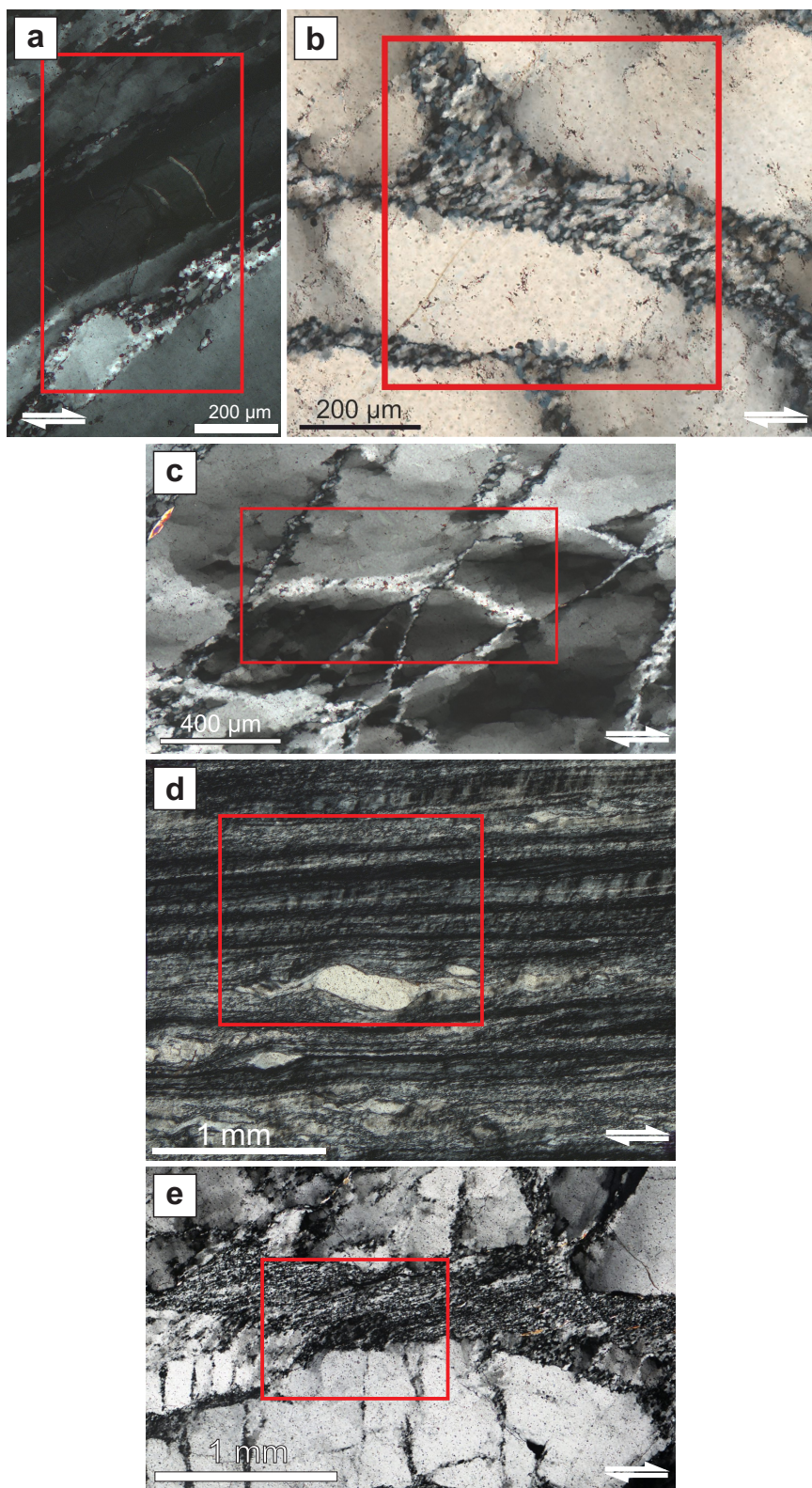


Figure SOM4

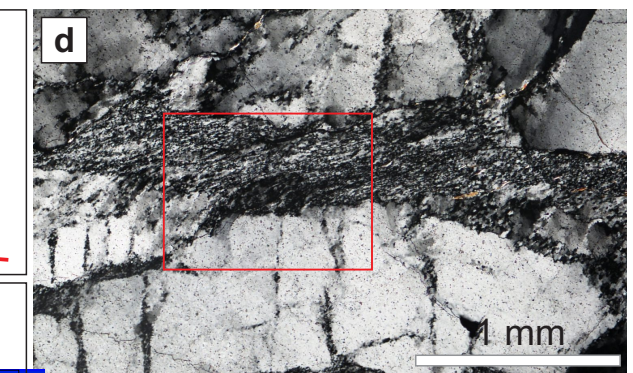
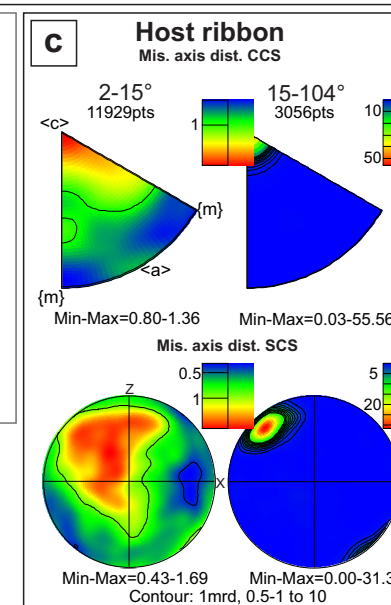
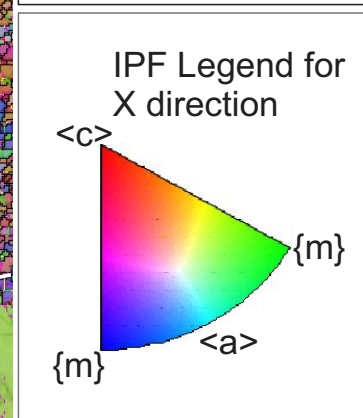
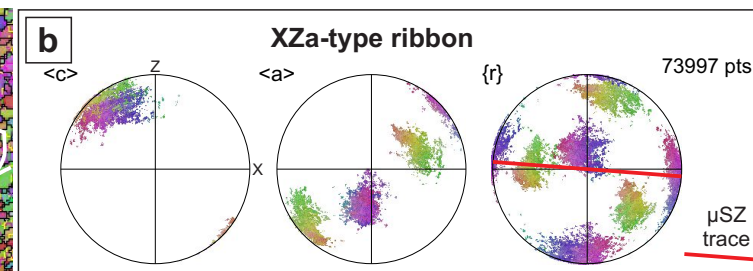
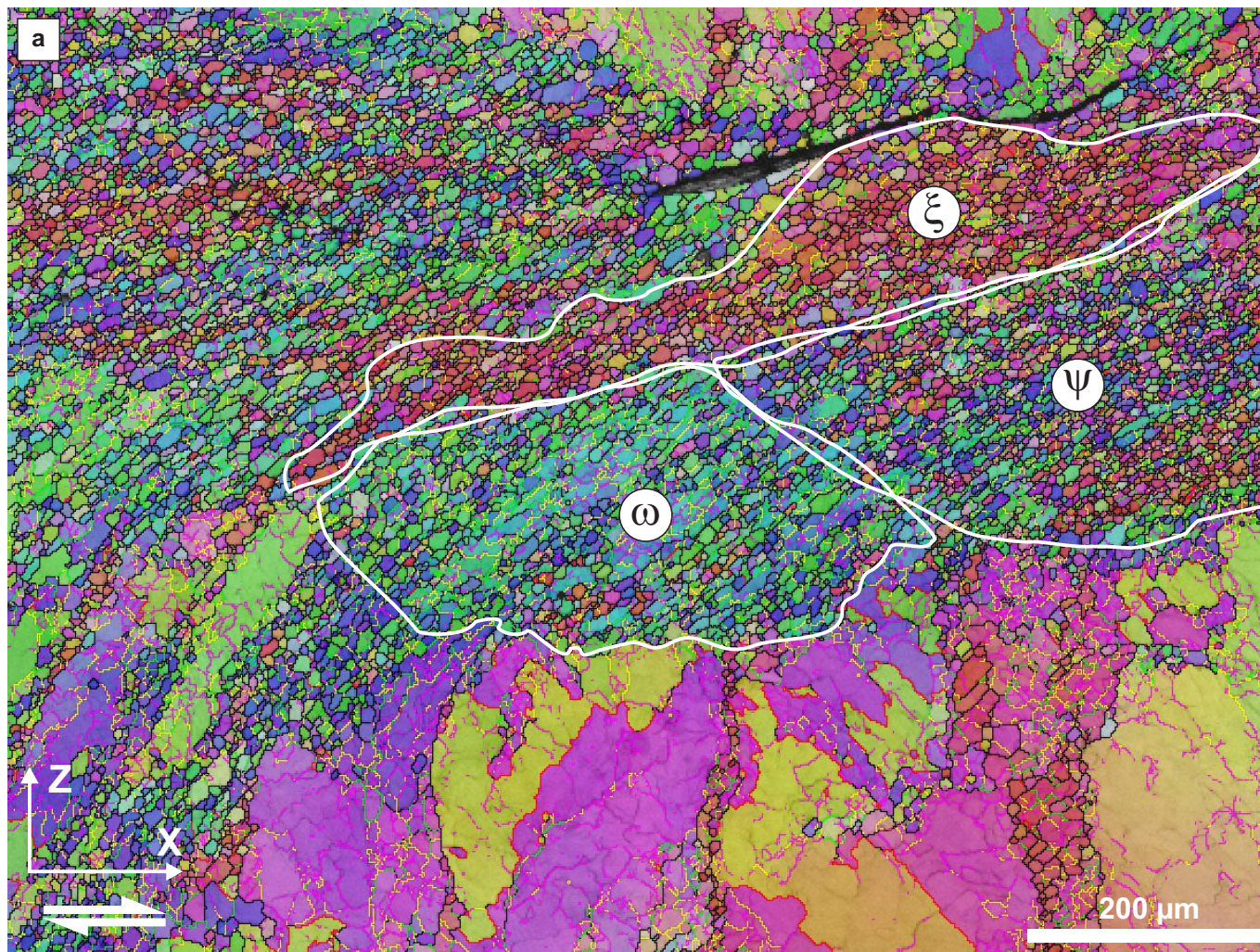
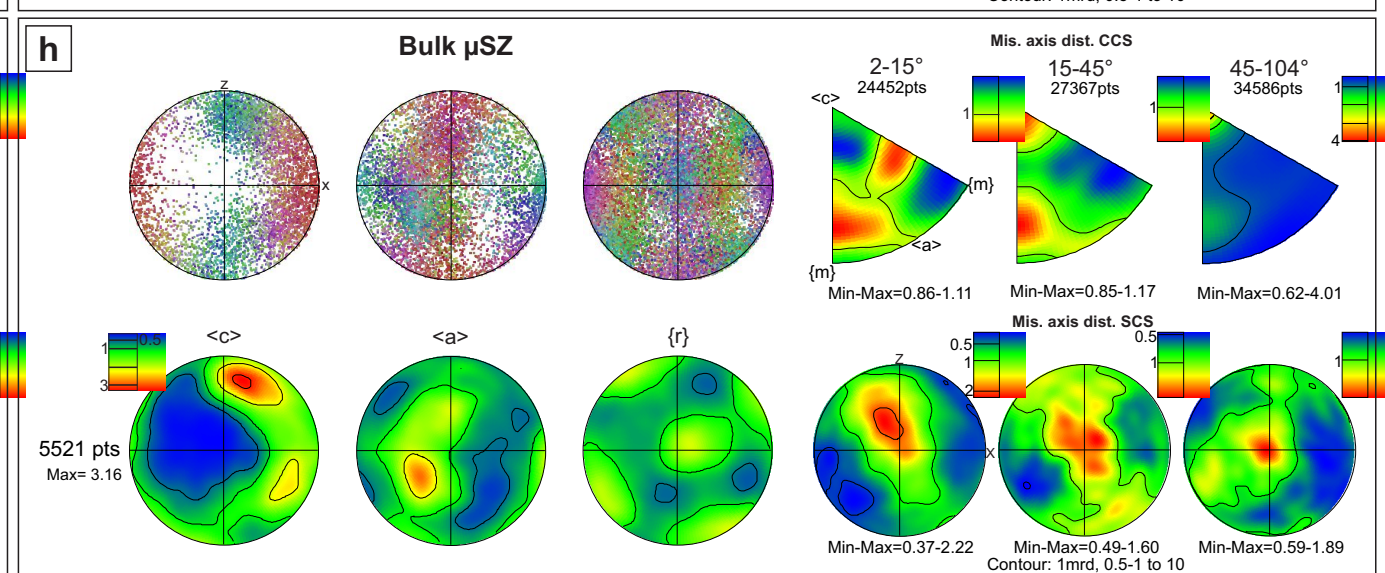
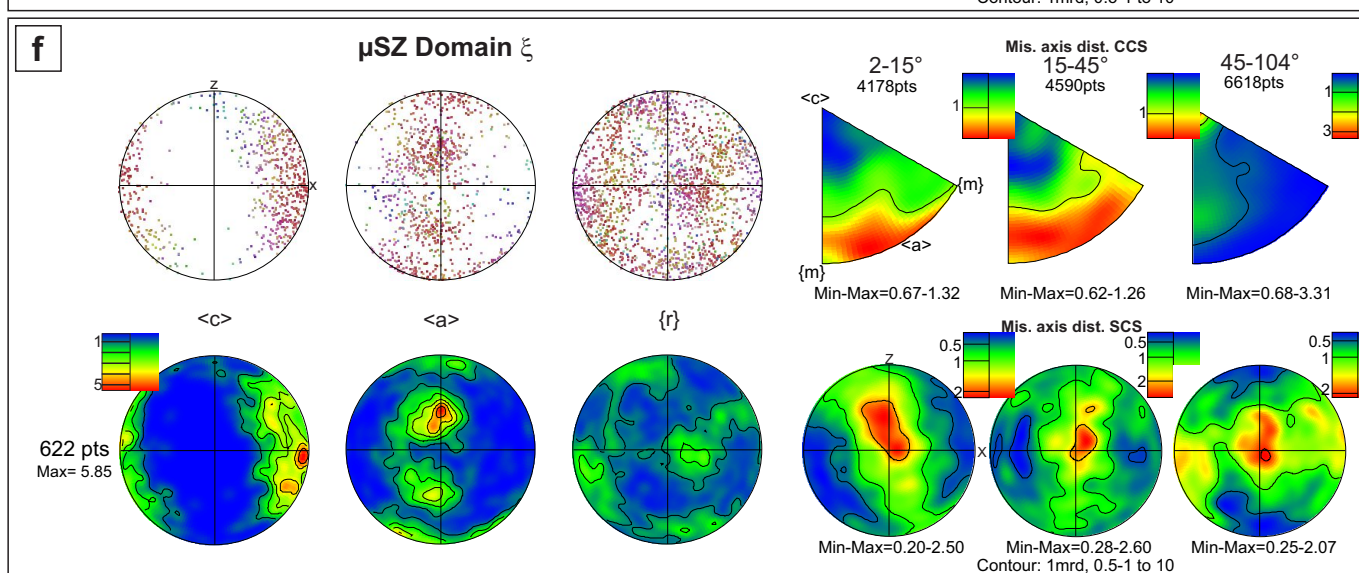
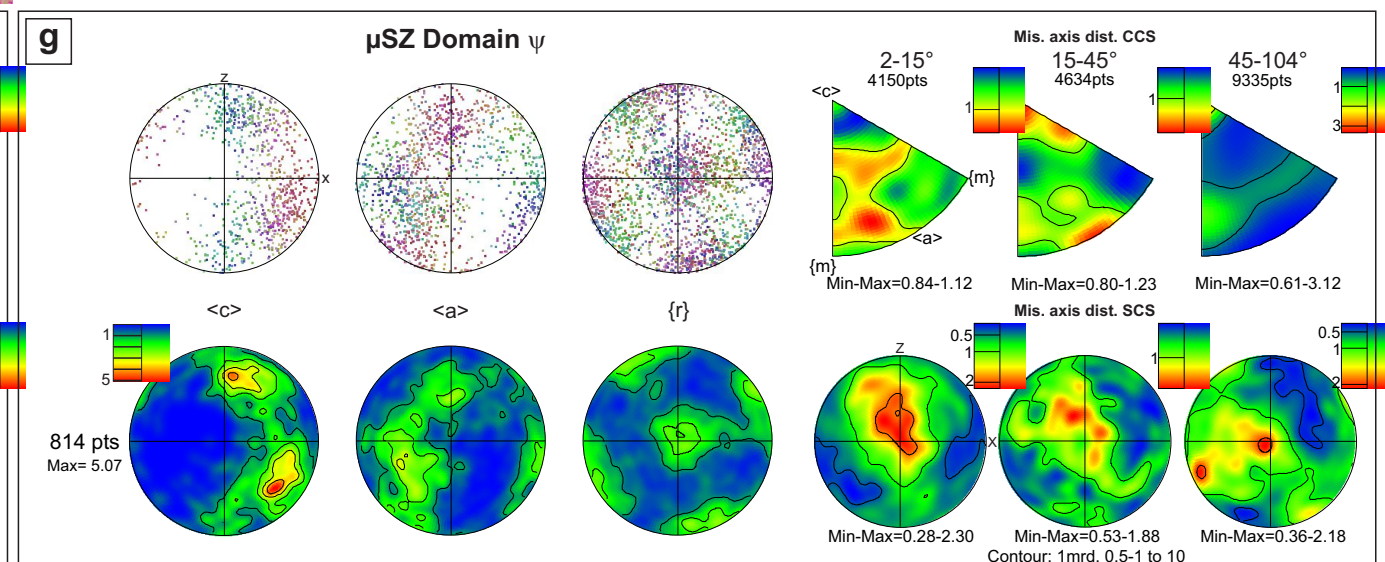
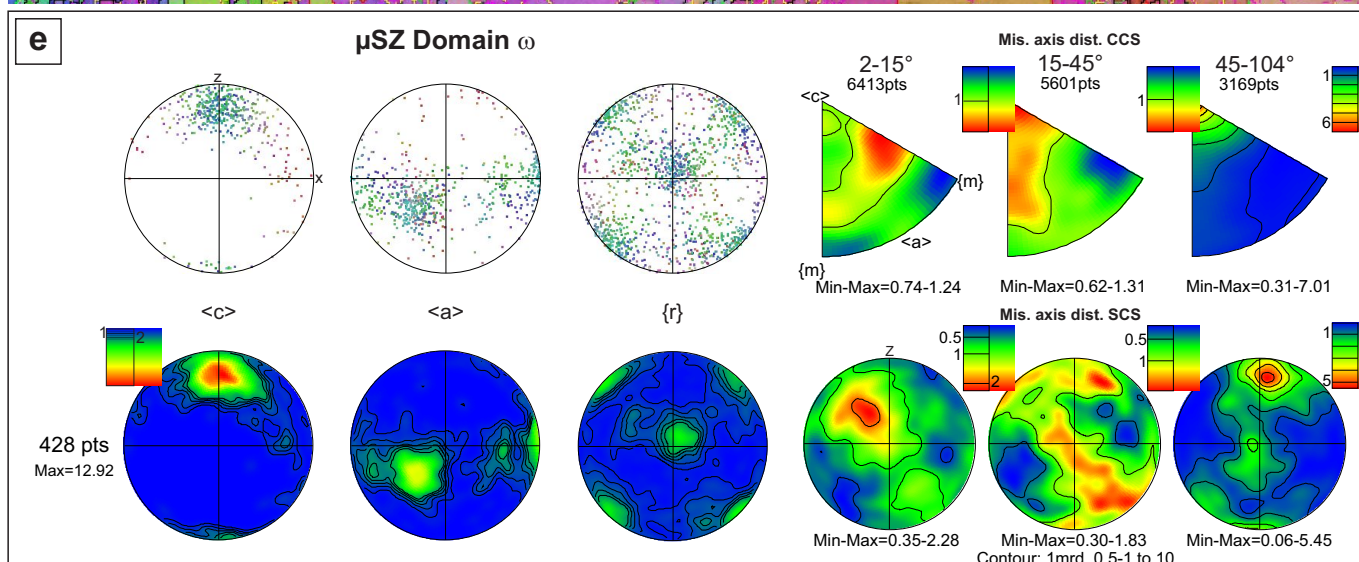


Figure SOM5



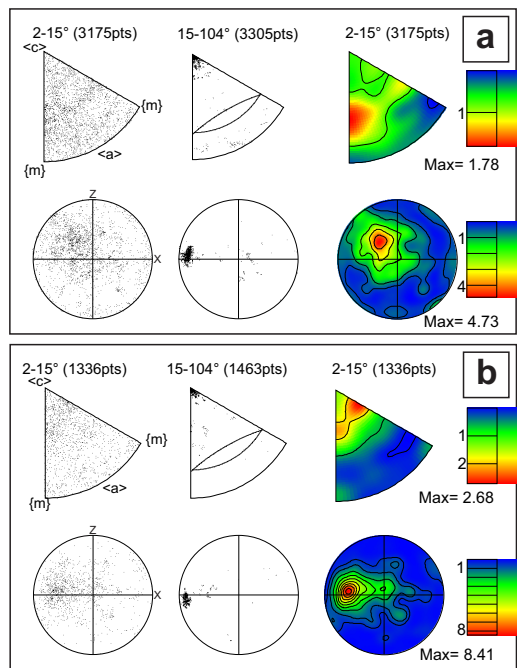


Figure SOM6

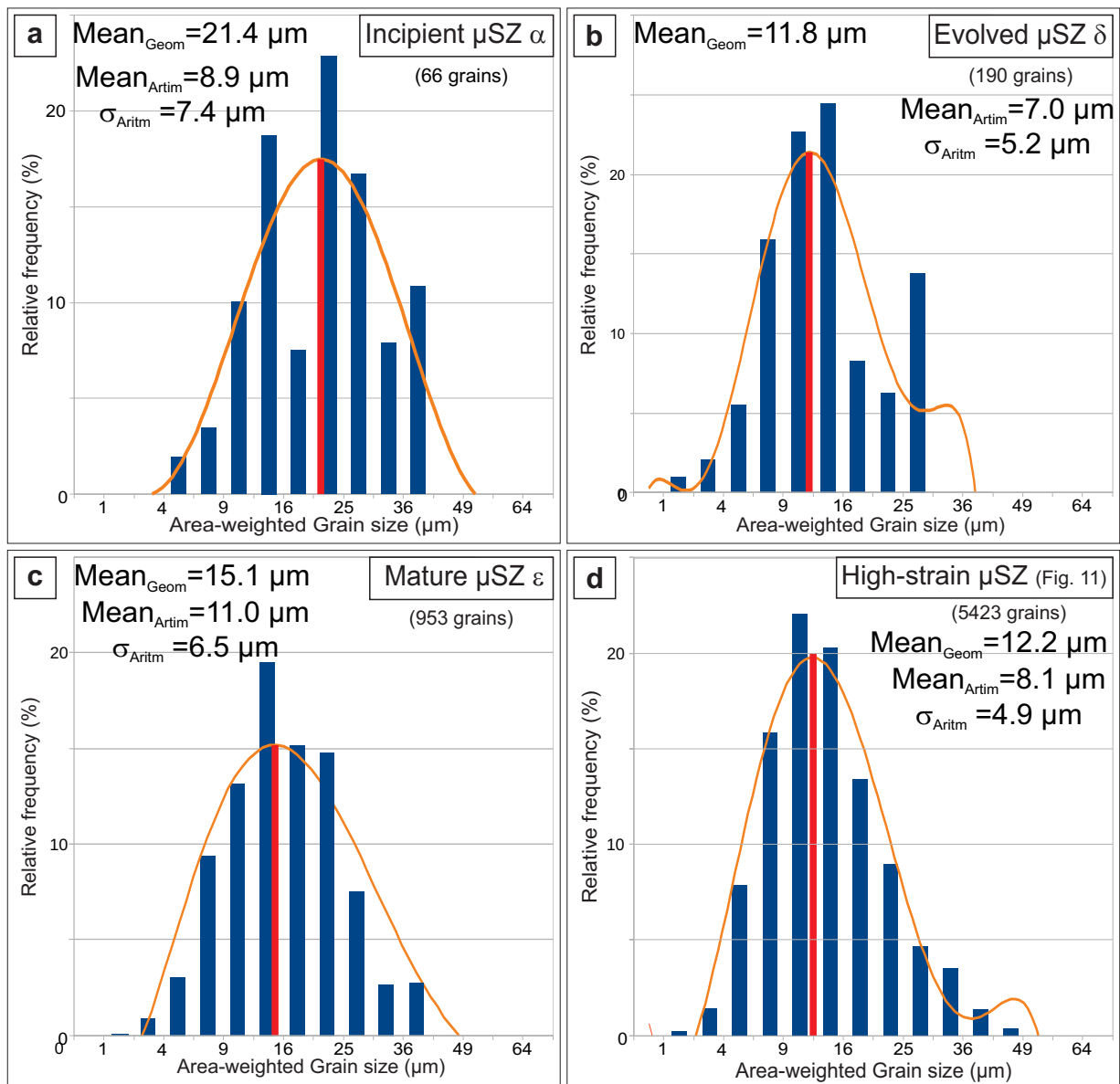


Figure SOM7

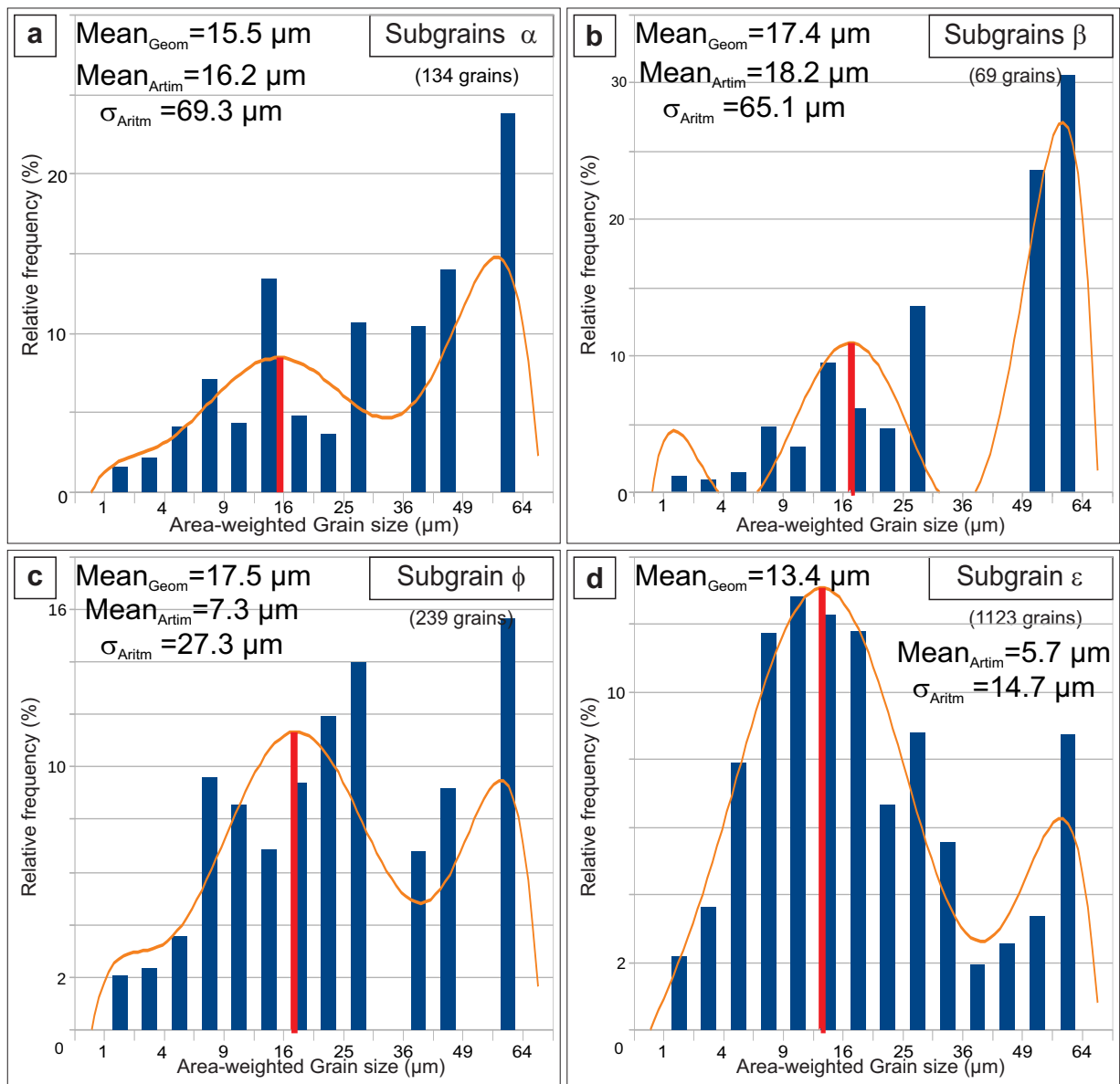


Figure SOM8

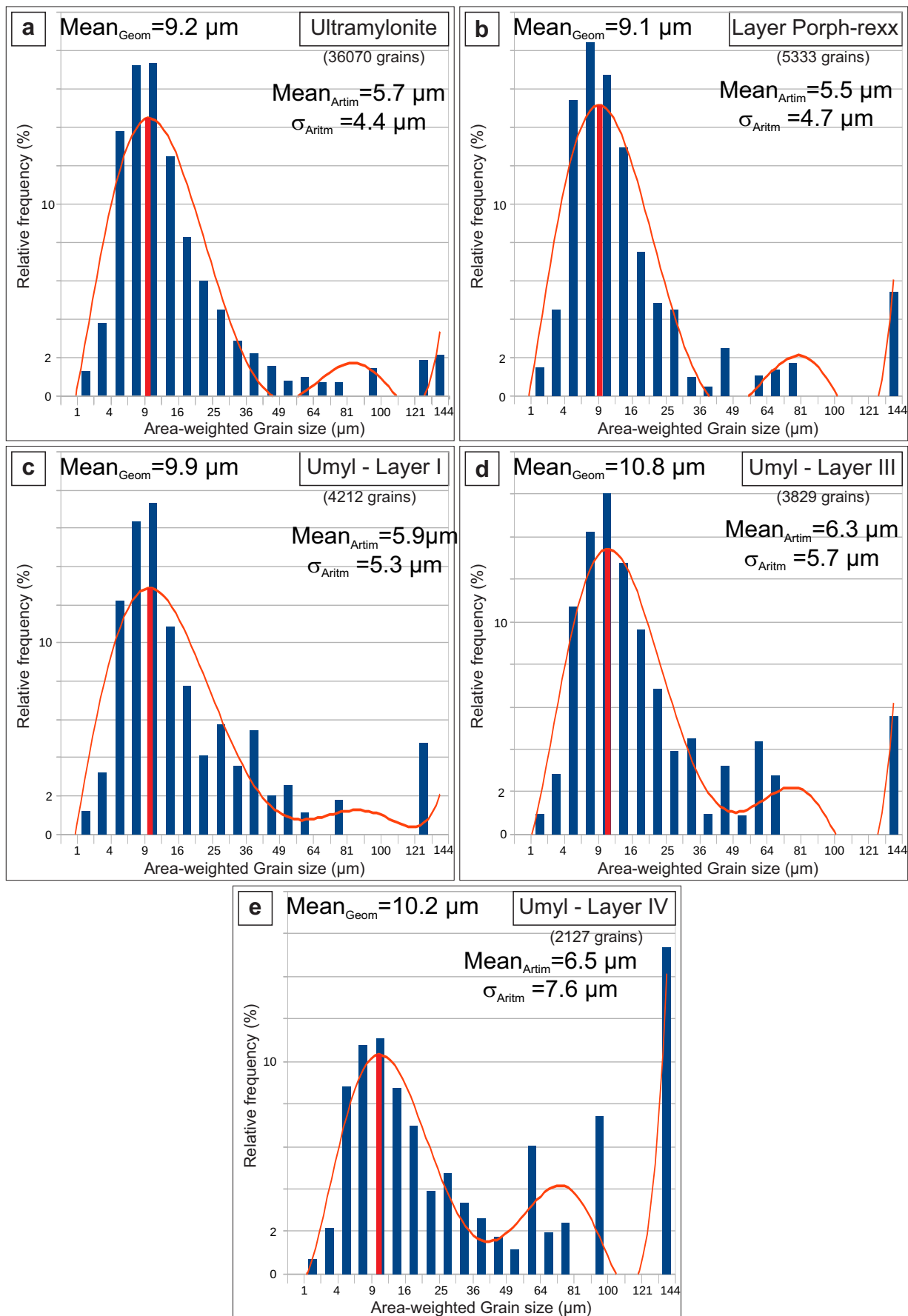


Figure SOM9

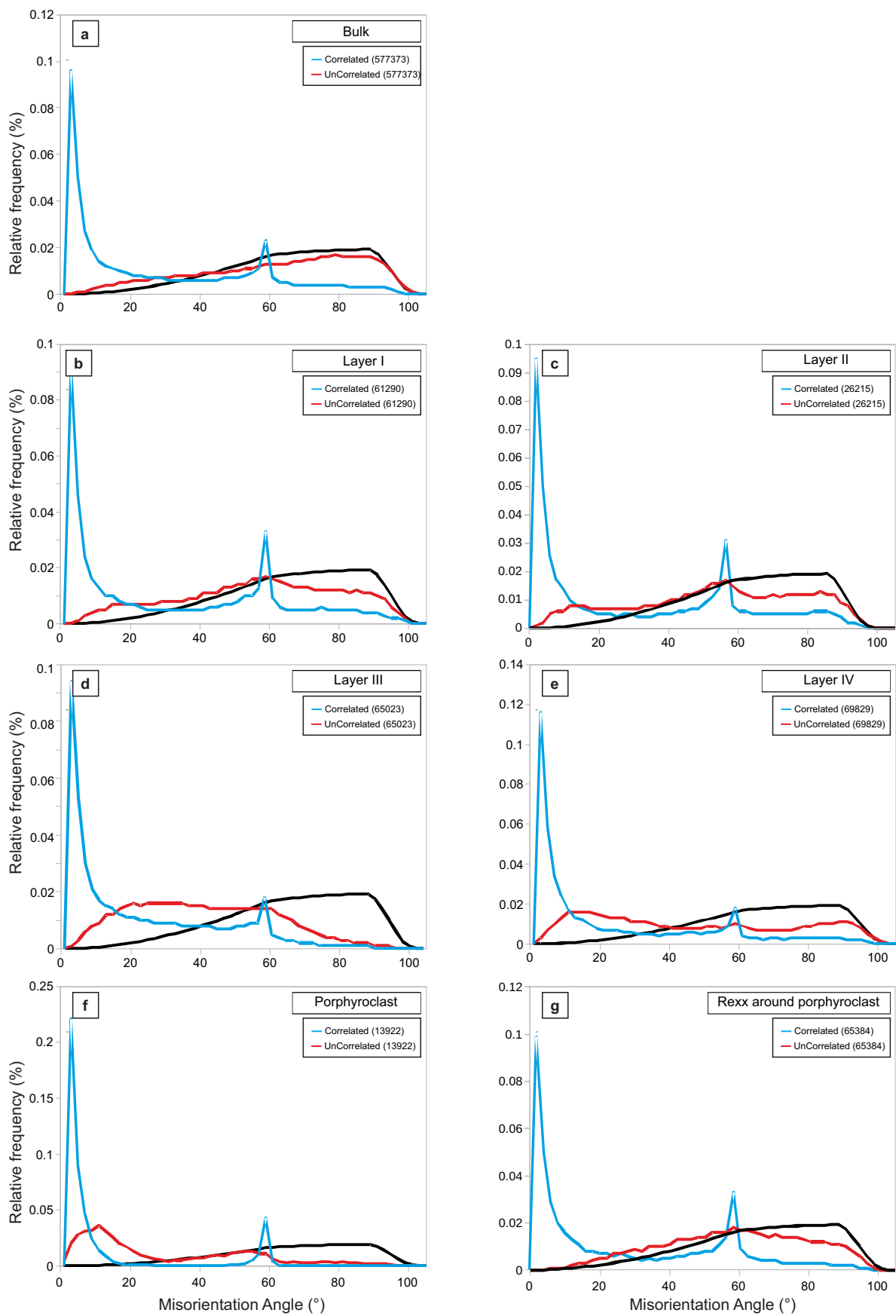


Figure SOM10

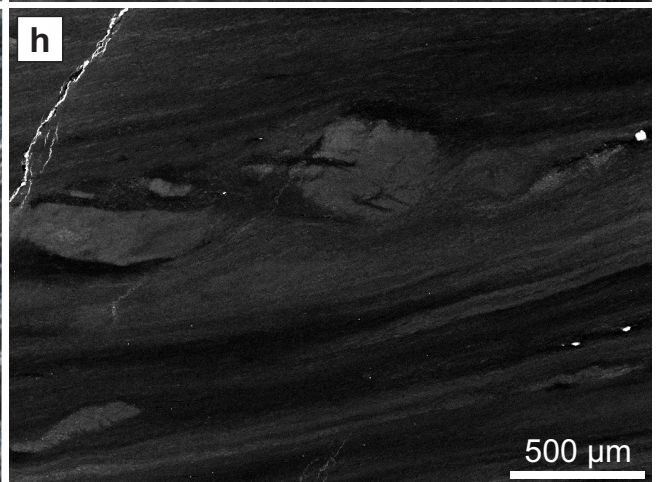
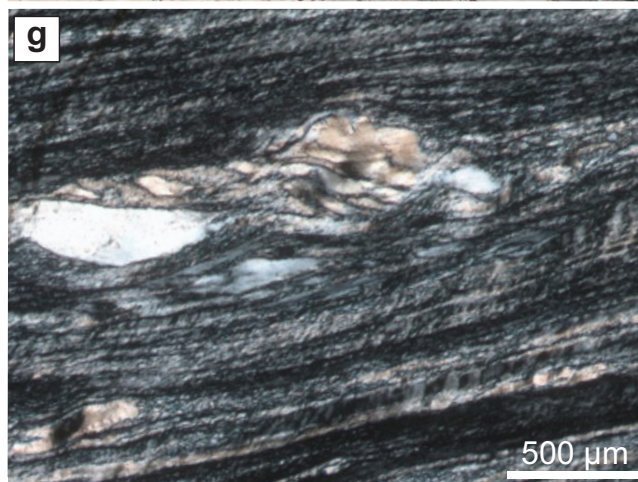
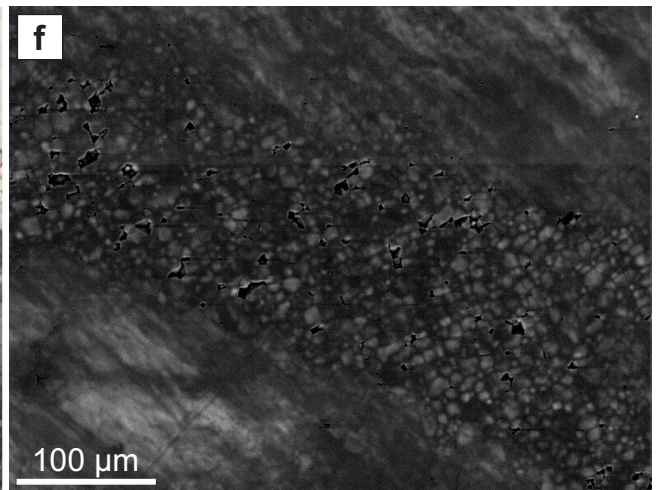
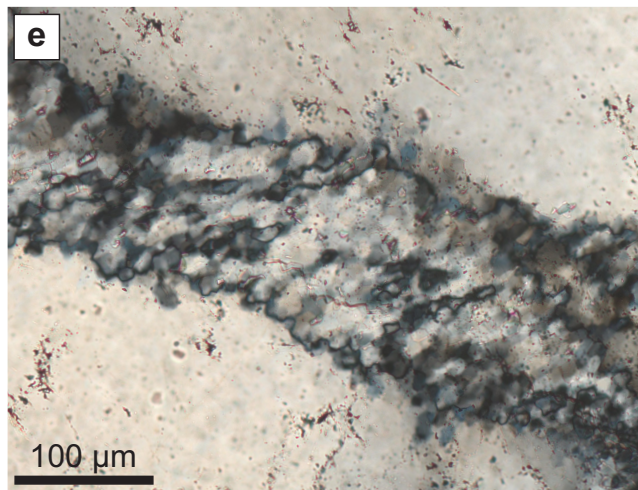
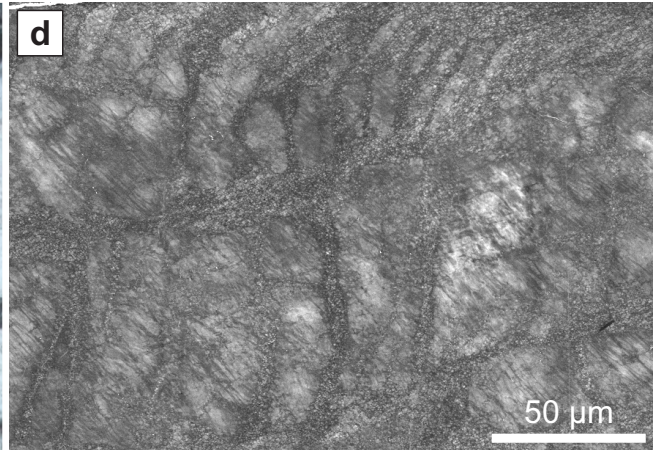
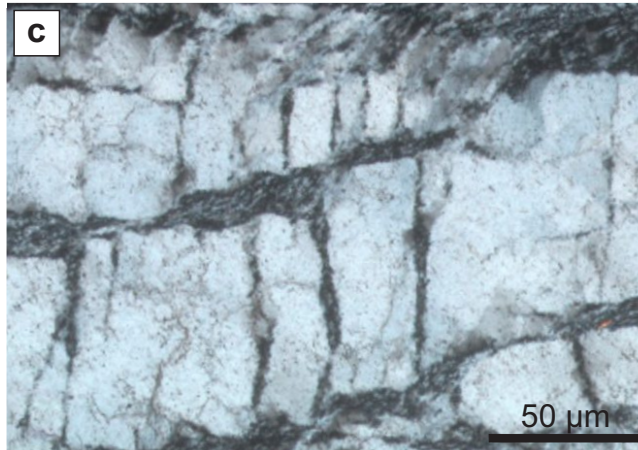
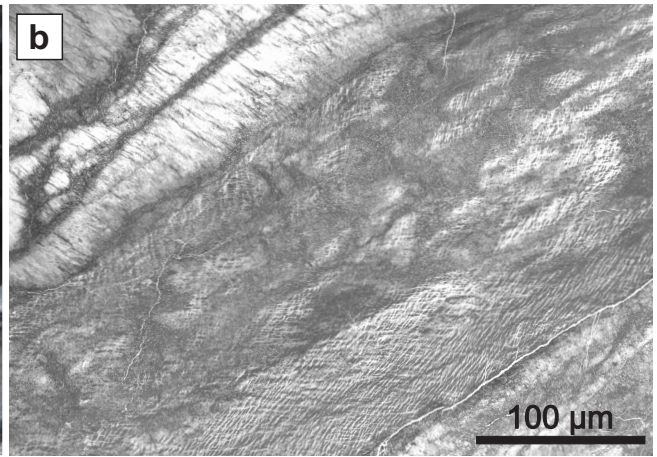
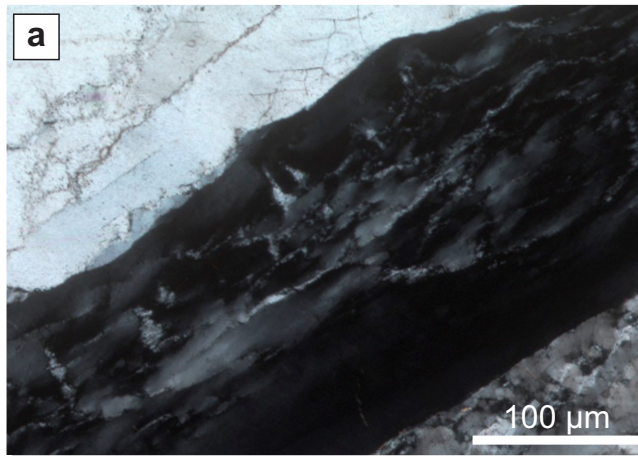


Figure SOM11

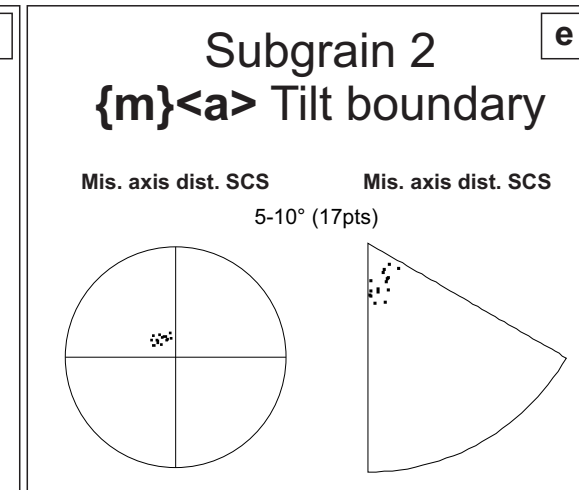
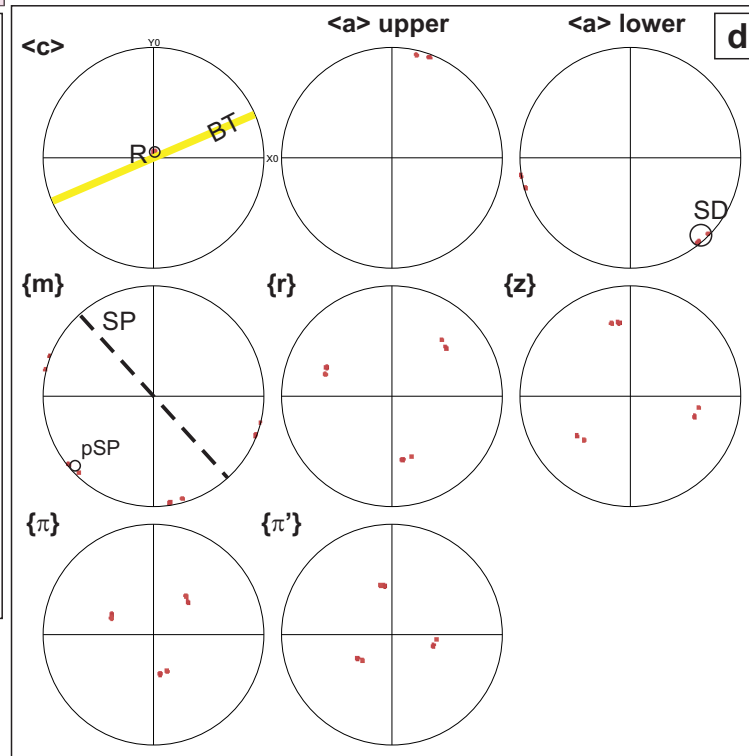
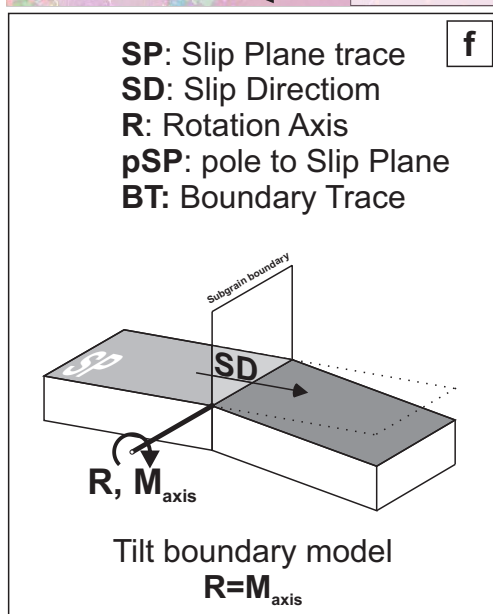
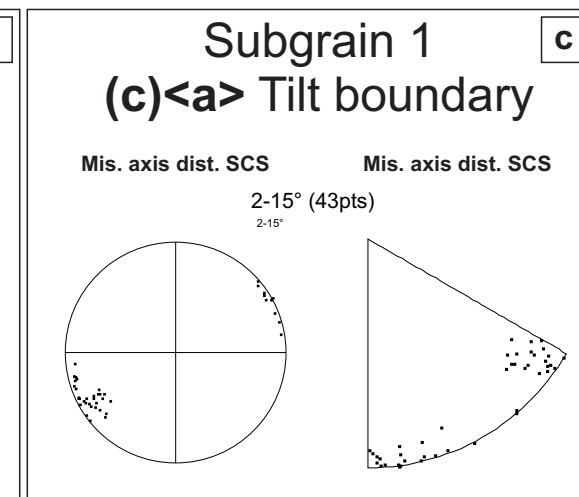
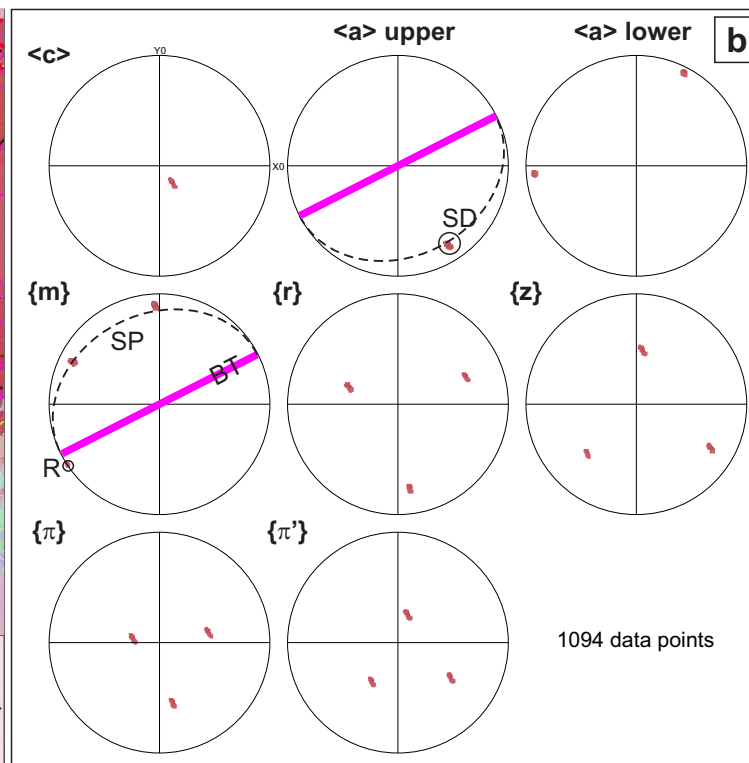
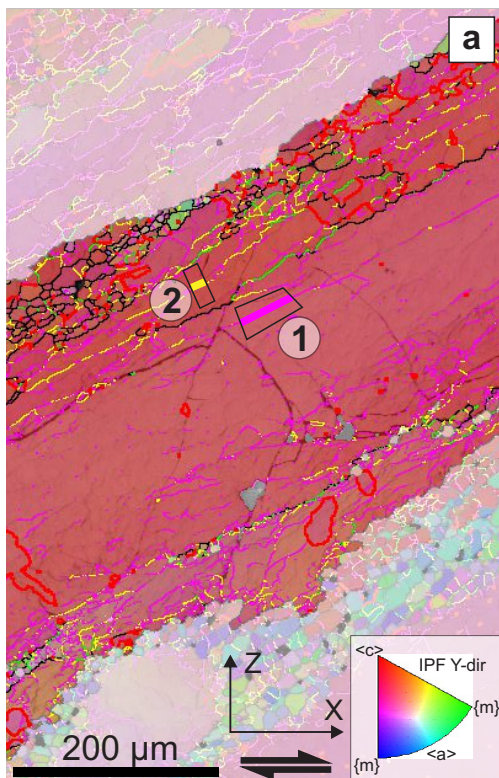


Figure SOM12

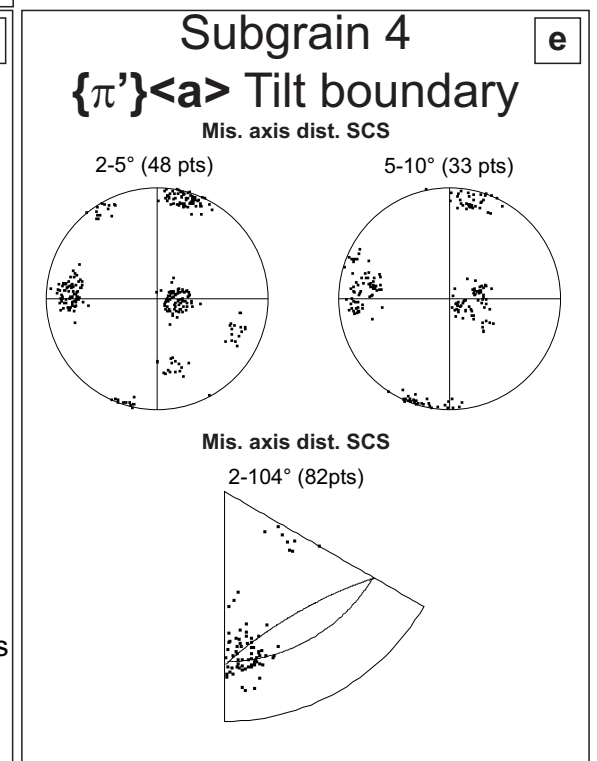
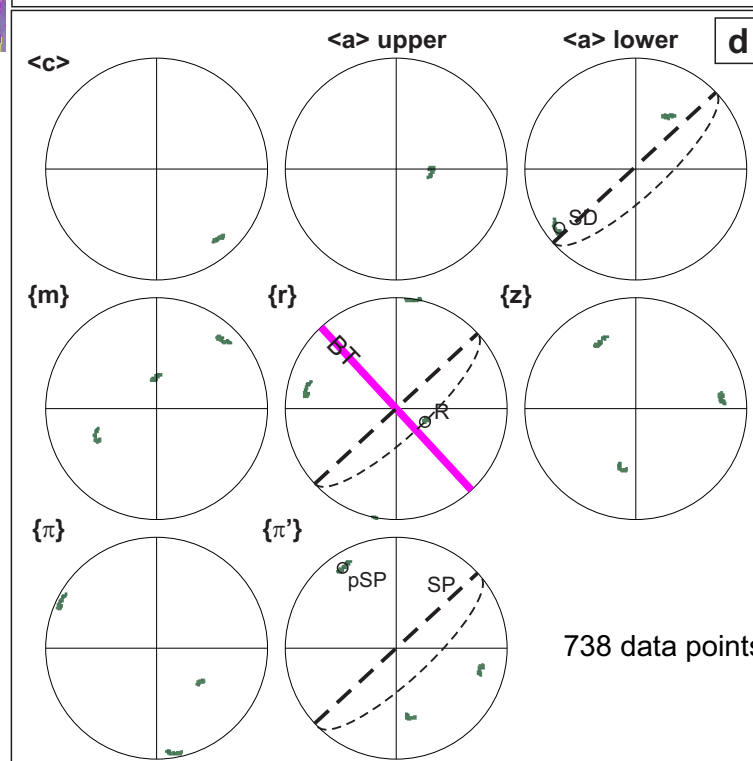
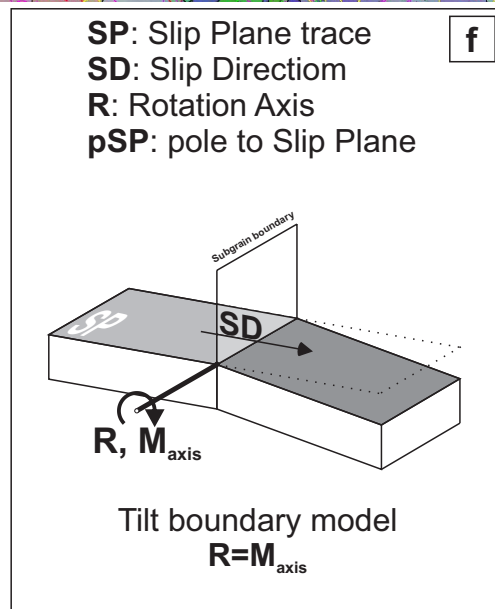
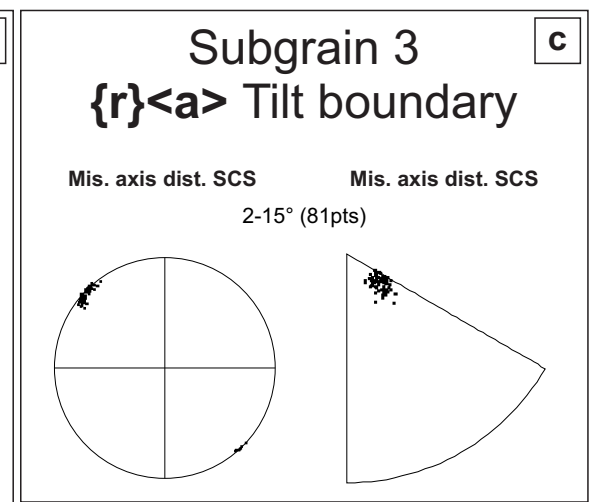
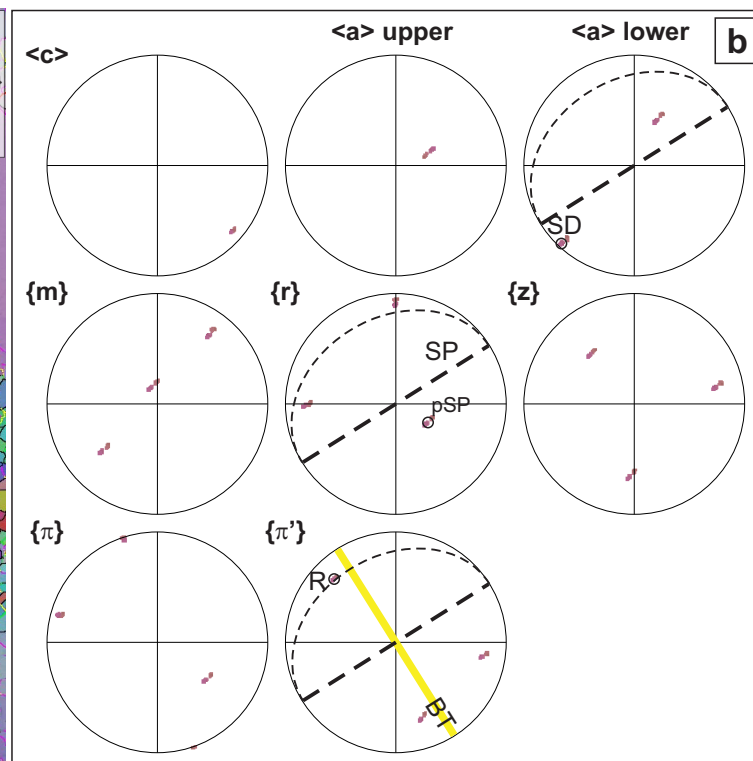
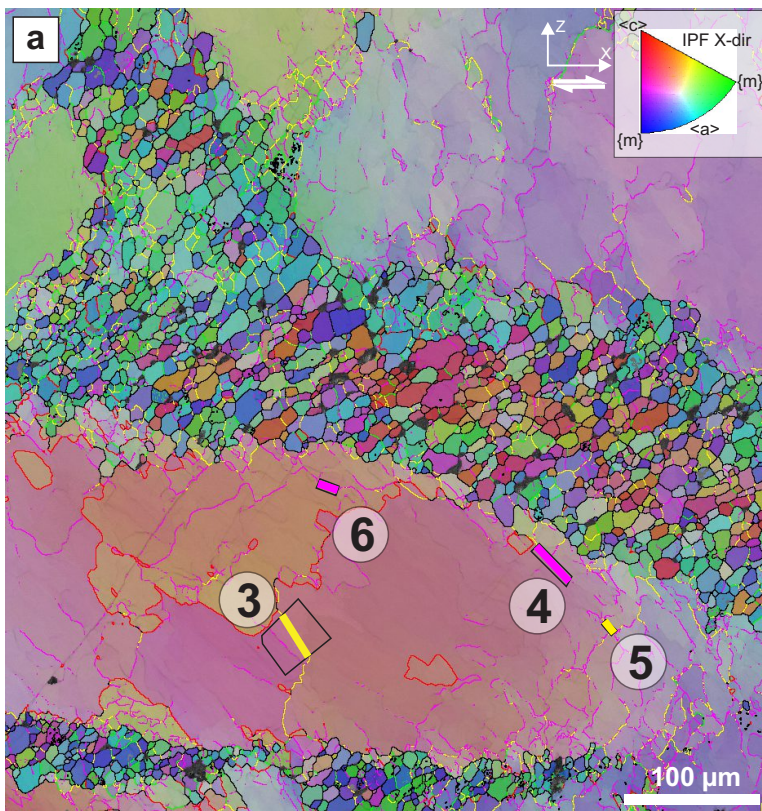


Figure SOM13

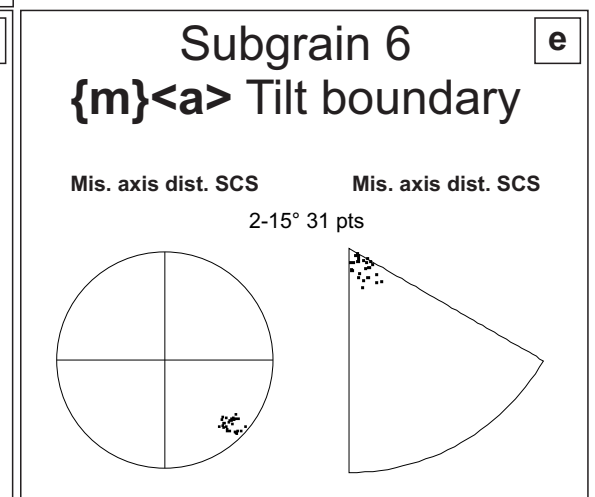
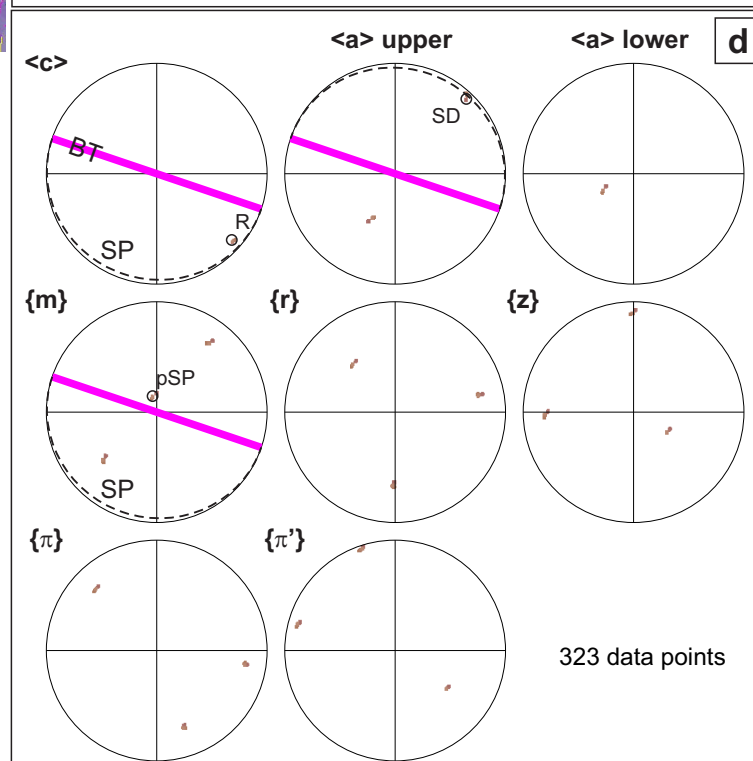
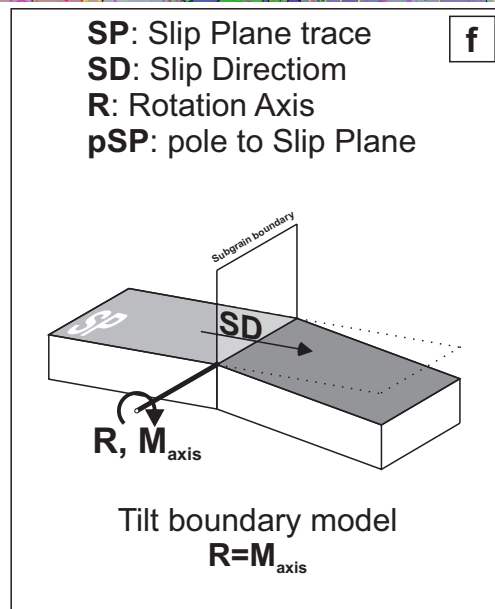
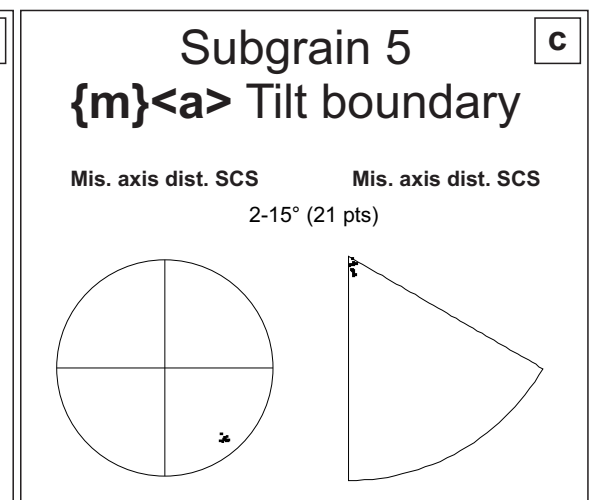
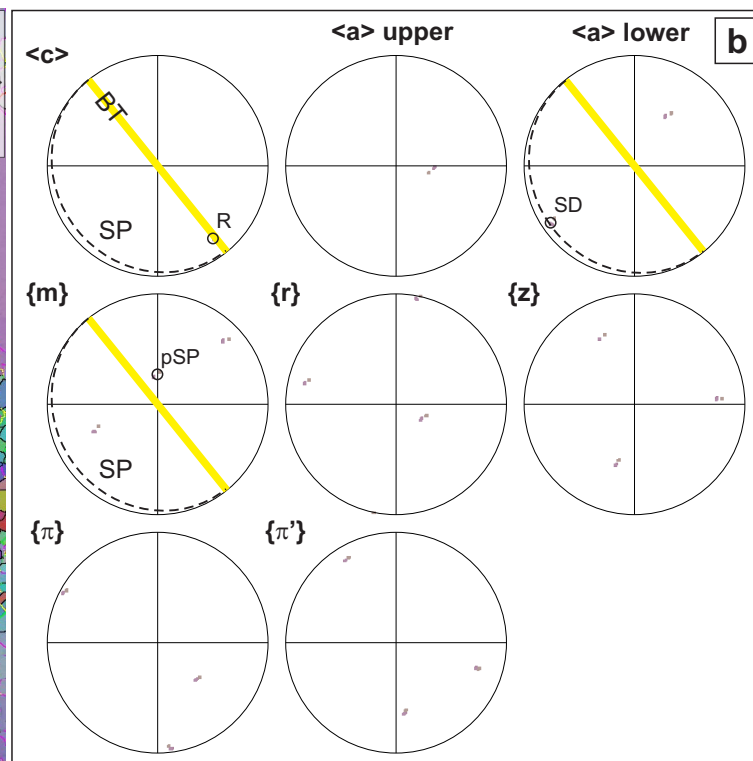
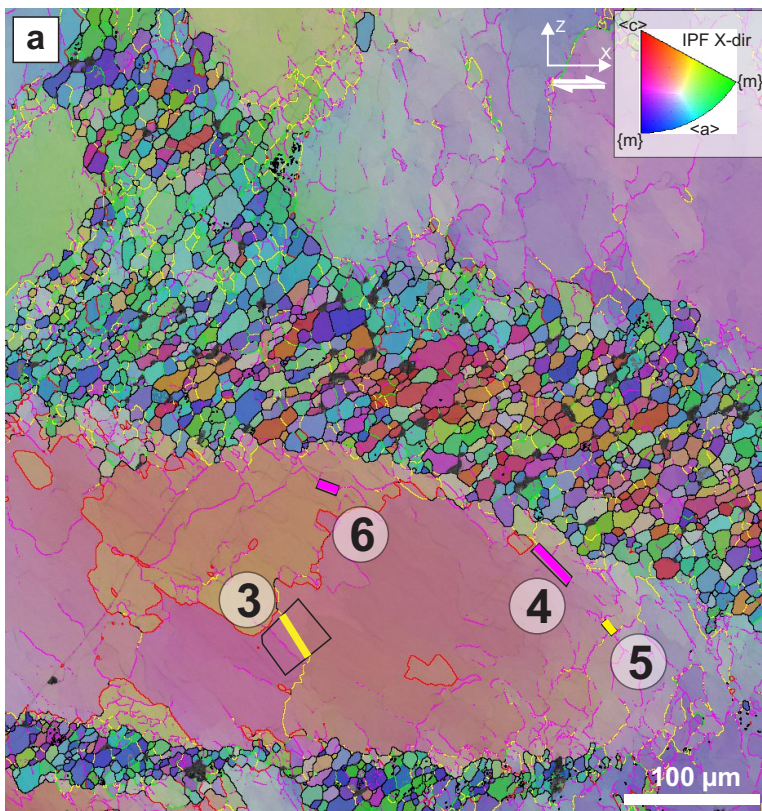


Figure SOM14

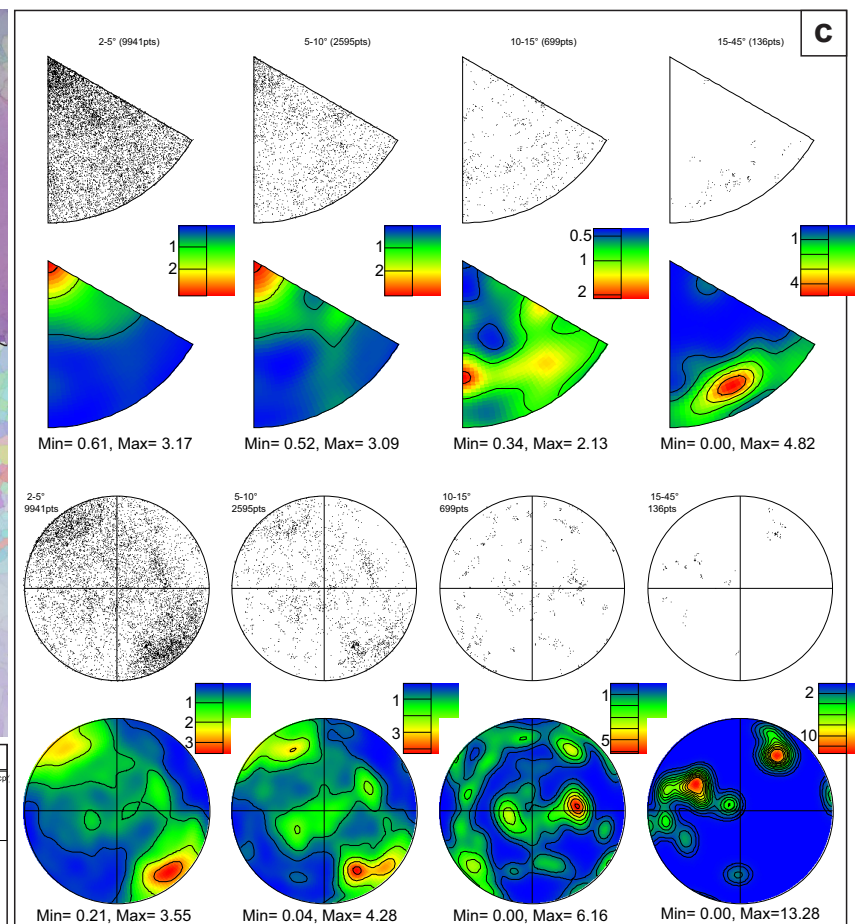
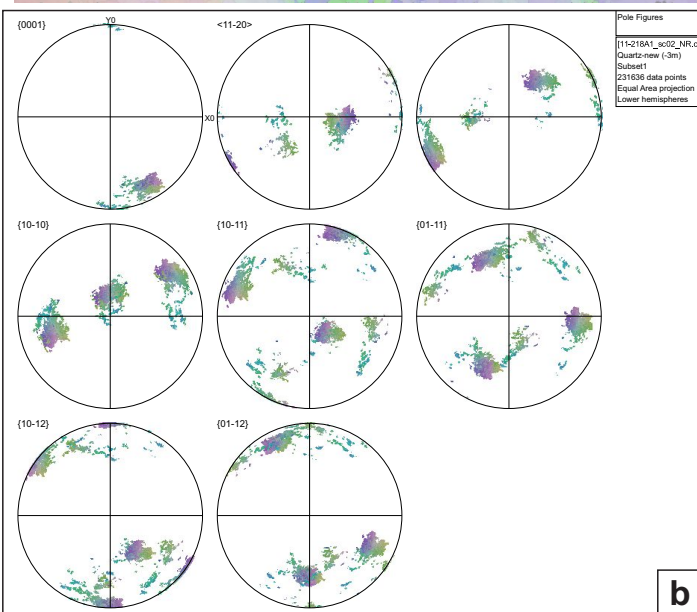
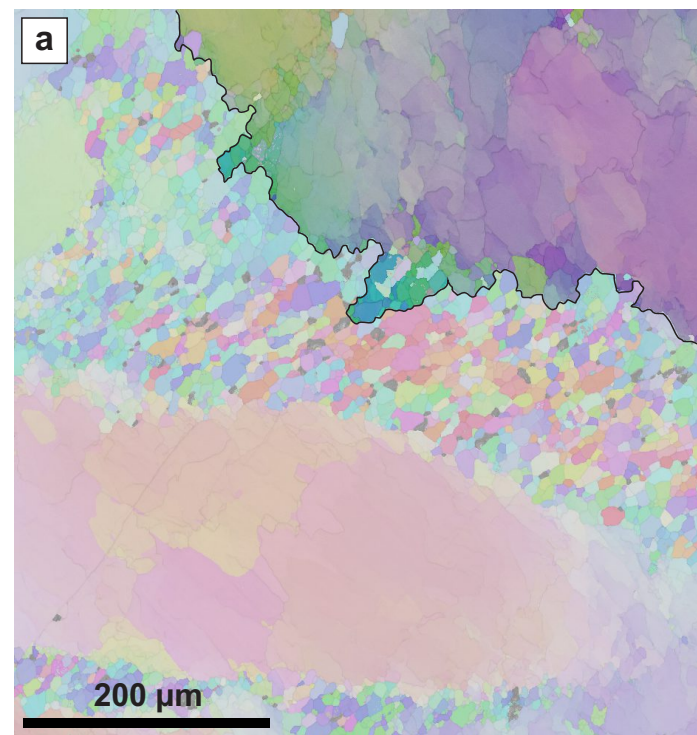


Figure SOM15

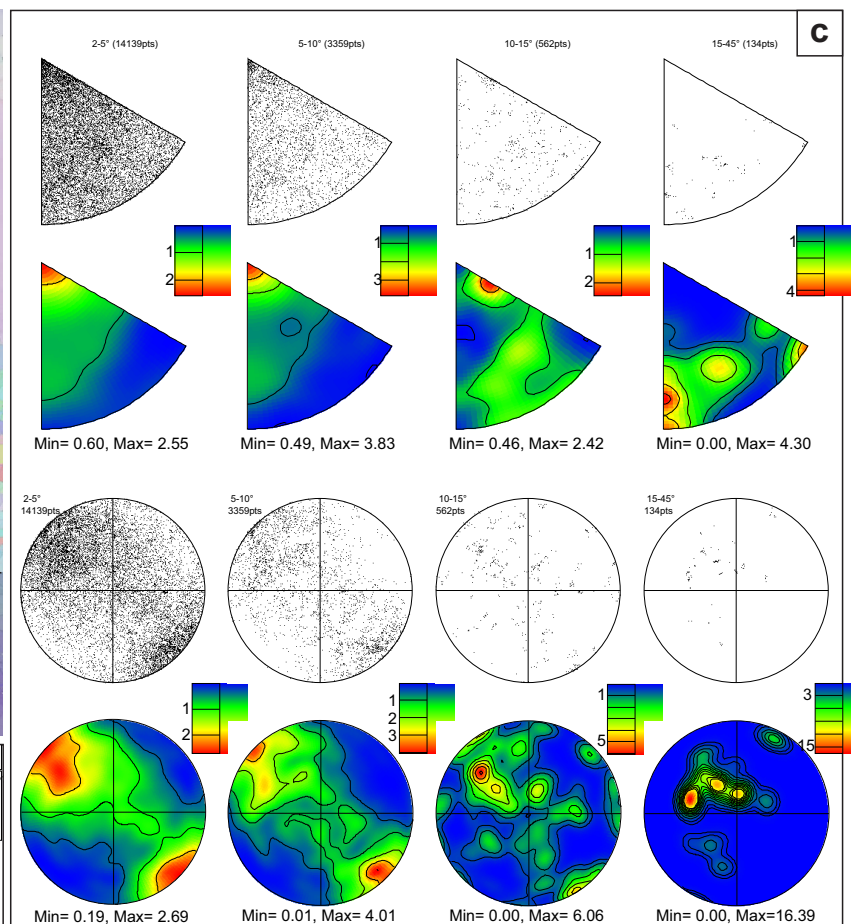
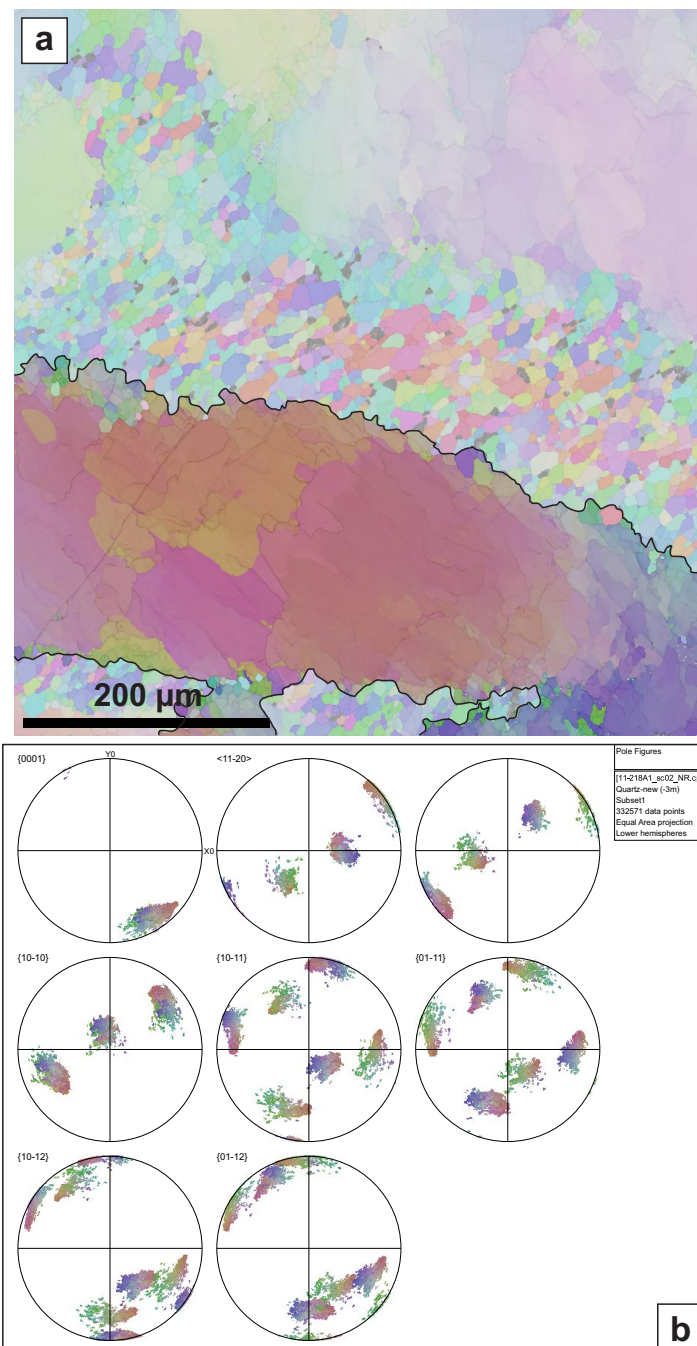


Figure SOM16

SEM-EBSD detector	FEG-SEM Zeiss 1540 EsB		JEOL 6610 LV SEM – Nordlys Nano		JEOL 7001 FE SEM Nordlys Max
Figure	Fig. 7	Fig. 8	Fig. 9	Fig. 6	Fig. 11
Subject	XZa-type μSZ		XZa-type μSZ		Ultramylonite
Magnification	130x	120x	120x	120x	90x
Step size (μm)	0.6	0.6	1.8	1.2	1.6
Size (μm)	560 x 590	520 x 600	1076 x 806	1076 x 484	1422 x 1195
Acquisition time (s/pxl)	0.074	0.074	0.178	0.040	0.34
Accelerating Voltage	20	20	20	20	20

Table SOM1

Fig. SOM1: Microstructure and CPO of protomylonitic quartz vein. (a) Optical microphotograph (crossed polars and inserted gypsum plate) of the 2nd thin section used with that shown in Fig. 2a for the analysis of the protomylonite. (b) Sketch drawn from (a) showing the different ribbons (in different colours) and incipient recrystallization aggregates (in black colour). The ribbons are colour-coded as a function of the mean c-axis orientation determined from CIP analysis, accordingly with the Look-Up Table (LUT) reported in (d); (c) Analysis of the orientations of fine-grained recrystallized aggregates (in black colour) in selected ribbon portions of the protomylonite shown in (a). The orientations of the μ SZ in the selected areas are shown in the rose diagrams. (d) CIP LUT showing (empty dots) the c-axis orientations of the ribbons. The dashed line represents the trace of the mylonitic foliation.

Fig. SOM2: Plot of the thickness versus displacement for μ SZ within ribbon grains.

Fig. SOM3: Microstructures of sheared quartz veins. (a) Thick (mature) μ SZ including small white mica flakes defining the internal oblique foliation. Note the extensive formation subgrains within the ribbon at the lower contact with the μ SZ. Crossed polars. (b) Same as in (a) with crossed polars and inserted gypsum plate. (c) Partially recrystallized ribbons in a mylonite. Note the incipient formation of a lozenge-shaped ribbon leftover derived from a XZ-type ribbon (central part of the microphotograph). (d) Ribbons dissected by pervasive C'-type μ SZs leading to formation quartz porphyroclasts in the ultramylonite. Crossed polars and inserted gypsum plate. (e) Ultramylonite showing extinction banding and including a ribbon leftover with an asymmetry unusual for a dextral sense of shear. Crossed polars. (f) Same as (f), but showing a more strongly asymmetric shape of the porphyroclast. (g) Secondary Electron (SE) SEM images of the grain surface of recrystallized grains along a μ SZ in mylonites showing pores with a crystallographically-controlled regular geometric shapes (etch pit type). (h) Same as (g). Sense of shear is dextral in all (a)-(f) microphotographs.

Fig. SOM4: optical micrographs (crossed polarizers) of ribbon areas (highlighted by the red rectangle) selected for the EBSD analyses. (a) Y-type ribbon of Fig. 6. (b) XZa-type ribbon of Fig. 7. (c) XZb-type ribbon of Fig. 8. (d) Ultramylonite (recrystallized matrix and porphyroclasts) of Fig. 10. (e) XZa-type ribbon with mature μ SZ of Fig. SOM5.

Fig. SOM5: EBSD orientation imaging and data for an XZa-type ribbon, and included mature μ SZ ω - ψ - ξ , in the protomylonite. (a) Orientation map colour-coded according to the inverse pole figure shown in the lower right corner. Boundaries are colour-coded as a function of misorientations according to the same legend in Fig. 6a. (b) Pole figures for the host ribbon showing the orientations of [c], <a> and {r} crystallographic directions. The trace of the μ SZ is shown as a red line. (c) Misorientation axis distributions for low (2-15°) and high (15-104°) misorientations in crystal and sample coordinates for the host ribbon. (d) Optical microphotographs (crossed polarizers) of the domain (included in the red box) shown in the EBSD map (a). (e) Pole figures ([c], <a> and {r} crystallographic directions) and misorientation axis distributions for low (2-15°), intermediate (15-45°) and high (45-104°) misorientations in IPF and sample coordinates for the μ SZ domain ω . (f) Idem as (e) for the μ SZ domain ξ . (g) Idem as (e) for the μ SZ domain ψ . (h) Idem as (e) for the bulk μ SZ (ω + ψ + ξ).

Fig. SOM6: Misorientation axis distributions for low (2-15°) and high (15-104°) misorientation in the host ribbons adjacent to incipient μ SZ α (a) and β (b) of Fig. 8. Both (a) and (b) include the misorientation axes distribution in crystal coordinate (first row) and in samples coordinates (second row) in both raw and contoured format.

Fig. SOM7: Area-weighted grain size distributions (Herweg and Berger, 2004) for the recrystallized aggregates within μ SZ zones: (a) incipient μ SZ α (Fig. 8a); (b) evolved μ SZ δ (Fig. 7a); (c-d) mature μ SZ ϵ (Fig. 7a) and of Fig. 9a.

Fig. SOM8: Area-weighted subgrain size distributions (Herweg and Berger, 2004) for the host ribbon close to incipient μ SZs α (a), β (b), and ϕ (c) of Fig. 8.

Fig. SOM9: Area-weighted grain size distributions (Herweg and Berger, 2004) for the recrystallized matrix aggregates of the ultramylonite of Fig. 11. (a) bulk ultramylonite (CPO in Fig. 11b); (b) recrystallized aggregate including the ribbon leftovers P (CPO in Fig. 10h); (c) layer I (CPO in Fig. 10c); (d) layer II (CPO in Fig. 10e); (e) layer IV (CPO in Fig. 10f).

Fig. SOM10: Misorientation angle distribution for recrystallized aggregates of the ultramylonite of Fig. 10a. (a) bulk ultramylonite (CPO in Fig. 10b); (b) layer I (CPO in Fig. 10c); (c) layer II (CPO in Fig. 10d); (d) layer III (CPO in Fig. 10e); (e) layer IV (CPO in Fig. 10f); (f) ribbon leftover P (CPO in Fig. 10g); (g) recrystallized aggregate around the ribbon leftovers P (CPO in Fig. 10h).

Fig. SOM11: Comparison between optical microstructure under crossed polarizers (right column) and SEM-CL images (left column). (a-b) Y-type ribbon. (c-d) Intersecting sets of recrystallized μ SZs within a XZa-type ribbon; (e-f) Detail of a dextral μ SZ within a XZa-type ribbon. (g-h) Ultramylonite showing a CPO banding and including a ribbon porphyroclast. Quartz luminescence is mainly related to the ~ 415 nm (blue) peak in panchromatic spectra that is strongly correlated with the trace concentration of Ti (Wark and Spear, 2005; Bestmann and Pennacchioni, 2015). Many studies have suggested that Ti resetting (and therefore resetting in CL patterns) in mylonitic rocks is enhanced by the occurrence of water-assisted deformation mechanisms and quartz precipitation (Grujic et al., 2011; Haertel et al., 2013; Bestmann and Pennacchioni, 2015). We performed a preliminary CL analysis of deformed Rieserferner quartz veins, with the purpose of detecting potential signatures for fluid-rock interaction during the different stages of shearing of the quartz veins.

We present CL images (Fig. SOM11) that provide evidence for the marked heterogeneity in the CL signal associated with the different microstructures. Protomylonites show complex and heterogeneous CL patterns (Fig. SOM11). The most strained parts of the XZ- and Z-type ribbons (that are less deformed than Y-type ribbons) have the lightest CL grey tones of the microstructure, which turn into dark tones in domains associated with crystal distortion, subgrain polygonization, incipient recrystallization and μ SZs. The domains of homogeneous deformation of Y-type ribbons (Figs. SOM11a-b) show a pervasive regular array of bright CL linear features organized in 2 intersecting sets, forming a lozenge shaped grid, overprinting a dark grey CL background. In zones of distortion of the Y-type ribbons this array is dissected irregularly across a network of darker CL zones coinciding with aggregates of subgrains and new grains or highly distorted zones.

The dark CL zones of incipient recrystallization have a granular appearance that is more clearly shown at the higher magnifications in CL images of the μ SZs across XZ-type grains (Figs. SOM11c-f). A direct comparison between the EBSD map of Fig. 7a and the corresponding CL image of Fig. SOM11f, clearly shows that the grains visible in the CL image perfectly match to subgrains and new grains along the μ SZ. These grains visible in CL show a light grey core and a dark rim, which results in the grainy appearance of the zone of polygonization and recrystallization described above. Adjacent to μ SZs there is commonly a very heterogeneous overprinting of the lighter CL tones of the less distorted portions of host ribbon by dark grey CL zones that are also associated with pervasive linear features subparallel to the main shortening direction. In general there is a coincidence between the CL darker tones with the most distorted parts of the ribbons. In ultramylonites, there is still heterogeneity in the CL patterns (Figs. SOM11g-h). The local ribbon leftovers have a lighter CL shade than the recrystallized matrix. This latter shows a CL banding, that partially matches the CPO banding, similar to that described by Bestmann and Pennacchioni (2015) for quartz in a mylonitic granodiorite.

Fig. SOM12: Boundary trace analysis (Prior et al., 2002; Piazzolo et al., 2008) of the Y-type ribbon of Fig. 6a. (a) EBSD color-coded map with location of the analysed subgrain boundaries 1 and 2. (b) Pole figures ($\langle c \rangle$, $\langle a \rangle$, $\{m\}$, $\{r\}$, $\{z\}$, $\{\pi\}$ and $\{\pi'\}$ crystallographic orientations) for EBSD data points around subgrain boundary 1; (c) Misorientation axis in sample and crystal coordinates across subgrain boundary 1; (d) Pole figures for EBSD data points around subgrain boundary 2; (e) Misorientation axis in sample and crystal coordinates across subgrain boundary 2. (f) Scheme of relationships between tilt boundaries and edge dislocations. In the pole figure sets (b, d), the possible geometrical elements are shown for a tilt boundary due to the activity of (c) $\langle a \rangle$ slip (subgrain boundary 1) and $\{m\}\langle a \rangle$ slip (subgrain boundary 2).

Fig. SOM13: Boundary trace analysis (Prior et al., 2002; Piazzolo et al., 2008) of the XZa-type ribbon of Fig. 7a. (a) EBSD color-coded map with location of the analysed subgrain boundaries 3-6. (b-e) Pole figures for subgrain boundary 3; (c) Misorientation axis in sample and crystal coordinates across subgrain boundary 3; (d) Pole figures for subgrain boundary 4; (e) Misorientation axis in sample and crystal coordinates across subgrain boundary 4. (f) Scheme of relationships between tilt boundaries and edge dislocations. In the pole figure sets (b, d), the possible geometrical elements are shown for a tilt boundary due to the activity of $\{r\}\langle a \rangle$ slip (subgrain boundary 3) and $\{\pi'\}\langle a \rangle$ slip (subgrain boundary 4).

Fig. SOM14: Boundary trace analysis (Prior et al., 2002; Piazzolo et al., 2008) of the XZa-type ribbon of Fig. 7a. (a) EBSD color-coded map with location of the analysed subgrain boundaries 3-6. (b-e) Pole figures for subgrain boundary 5; (c) Misorientation axis in sample and crystal coordinates across subgrain boundary 5; (d) Pole figures for subgrain boundary 6; (e) Misorientation axis in sample and crystal coordinates across subgrain boundary 6. (f) Scheme of relationships between tilt boundaries and edge dislocations. In the pole figure sets (b, d), the possible geometrical elements are shown for a tilt boundary due to the activity of $\{m\}\langle a \rangle$ slip for both subgrain boundaries 5 and 6.

Fig. SOM15: Misorientation axis distribution for host ribbon of Fig. 7a (domain in the upper right side of the μ SZ). (a) EBSD color-coded map (with semi-transparent colour for non-analysed areas). (b) Pole figures for $\langle c \rangle$, $\langle a \rangle$, $\{m\}$, $\{r\}$, $\{z\}$, $\{\pi\}$ and $\{\pi'\}$ crystallographic orientations. (c) Misorientation axis distribution diagrams (both inverse pole figures and in sample coordinates) for the misorientation ranges of 2-5°, 5-10°, 10-15° and 15-45°. See text for explanation.

Fig. SOM16: Misorientation axis distribution for host ribbon of Fig. 7a (domain in the lower left side of the μ SZ). (a) EBSD color-coded map (with semi-transparent colour for non-analysed areas). (b) Pole figures for $\langle c \rangle$, $\langle a \rangle$, $\{m\}$, $\{r\}$, $\{z\}$, $\{\pi\}$ and $\{\pi'\}$ crystallographic orientations. (c) Misorientation axis distribution diagrams (both inverse pole figures and in sample coordinates) for the misorientation angle ranges of 2-5°, 5-10°, 10-15° and 15-45°. See text for explanation.

Table SOM1: Scanning electron microscope typology and analytical conditions for EBSD maps reported in Figs. 6-7-8, Fig. 10 and Fig. SOM5.

We present CL images (Fig. SOM15) that provide evidence for the marked heterogeneity in the CL signal associated with the different microstructures. Protomylonites show complex and heterogeneous CL patterns (Fig. SOM15). The most strained parts of the XZ- and Z-type ribbons (that are less deformed than Y-type ribbons) have the lightest CL grey tones of the microstructure, which turn into dark tones in domains associated with crystal distortion, subgrain polygonization, incipient recrystallization and μ SZs. The domains of homogeneous deformation of Y-type ribbons (Figs. SOM15a-b) show a pervasive regular array of bright CL linear features organized in 2 intersecting sets, forming a lozenge shaped grid, overprinting a dark grey CL background. In zones of distortion of the Y-type ribbons this array is dissected irregularly across a network of darker CL zones coinciding with aggregates of subgrains and new grains or highly distorted zones. The dark CL zones of incipient recrystallization have a granular appearance that is more clearly shown at the higher magnifications in CL images of the μ SZs across XZ-type grains (Figs. SOM15c-f). A direct comparison between the EBSD map of Fig. 7a and the corresponding CL image of Fig. SOM15f, clearly shows that the grains visible in the CL image perfectly match to subgrains and new grains along the μ SZ. These grains visible in CL show a light grey core and a dark rim, which results in the grainy appearance of the zone of polygonization and recrystallization described above. Adjacent to μ SZs there is commonly a very heterogeneous overprinting of the lighter CL tones of the less distorted portions of host ribbon by dark grey CL zones that are also associated with pervasive linear features subparallel to the main shortening direction. In general there is a coincidence between the CL darker tones with the most distorted parts of the ribbons. In ultramylonites, there is still heterogeneity in the CL patterns (Figs. SOM15g-h). The local ribbon leftovers have a lighter CL shade than the recrystallized matrix. This latter shows a CL banding, that partially matches the CPO banding, similar to that described by Bestmann and Pennacchioni (2015) for quartz in a mylonitic granodiorite.

Table SOM1: Scanning electron microscope typology and analytical conditions for EBSD maps reported in Figs. 6-9 and Fig. 11.